

Thesis for the Degree of Doctor of Philosophy in Physics



Application of the 9.4T MRI system with a  
cryo-coil to study demyelination in the animal  
model of multiple sclerosis

Weronika Piędzia

The work was performed under supervision of dr hab. Władysław Węglarz  
at the Department of Magnetic Resonance Imaging  
Henryk Niewodniczański Institute of Nuclear Physics  
Polish Academy of Sciences  
Kraków, Poland  
2023

## ***Podziękowania:***

Składam serdeczne podziękowania dr. hab. Władysławowi Węglarzowi za pomoc i opiekę w realizacji projektu oraz wszystkie cenne wskazówki w czasie wykonywania eksperymentów i w trakcie pisania pracy doktorskiej. Jestem niezmiernie wdzięczna za okazane serce i niesamowitą życzliwość, która zawsze dodawała mi „ducha do walki”.

Dziękuję również dr. Krzysztofowi Jasińskiemu za pomoc w eksperymentach MRI a w szczególności za pomoc w wykonaniu map czasów relaksacji.

Dziękuję także dr Katarzynie Kalicie za pomoc przy zwierzętach, które przysłużyły się poniżej opisanym badaniom.

Dziękuję za wykonanie histopatologii przez zespół Prof. dr. hab. Krzysztofa Janeczko z Uniwersytetu Jagiellońskiego.

Dziękuję Prof. Tadeuszowi Lesiakowi za pomoc i wskazanie drogi podczas studiów doktoranckich oraz przywrócenie wiary w drugiego człowieka w chwilach zwątpienia.

Szczególne podziękowania kieruję w stronę Mojej Wspaniałej Mamy za bezinteresowną Miłość i tak ogromne wsparcie w trudnych chwilach oraz Mojej Ukochanej Babci za cierpliwość i wyrozumiałość oraz to, że była przy mnie każdego dnia.

Z całego Serca dziękuję mojemu Przyjacielowi Sławkowi Łozie za Jego niezłomną i niczym nie strudzoną wiarę we mnie, niezależnie od sytuacji i problemów, z którymi przyszło mi się zmierzyć.

Na koniec chcę podziękować Osobie, która przez wiele lat mojego dorosłego życia była dla mnie wsparciem i opoką, idąc ze mną krok w krok, nie raz przez zakamarki labiryntu trudów i zwątpienia, zawsze wyciągając pomocną dłoń, kiedy droga wydawała się niemożliwa do pokonania.

Dziękuję Ci Tomusiu ... Spoczywaj w Pokoju.

## Streszczenie

Praca doktorska opisuje zastosowanie różnorodnych technik badawczych na systemie do obrazowania magnetyczno-rezonansowego (MR) w polu 9,4T w celu badań procesów demielinizacji w modelu mysim stwardnienia rozsianego (łac. sclerosis multiplex, SM).

Wiele istniejących chorób neurologicznych jest obecnie diagnozowanych w późnych stadiach rozwoju. Spowodowane jest to brakiem metod umożliwiających diagnozę na wczesnym, pre-symptomatycznym etapie co pozwoliłoby na efektywne leczenie. Obrazowanie magnetyczno-rezonansowe (ang. MRI) dostarcza wysokiej jakości obrazów z bardzo dobrym kontrastem tkanek miękkich dzięki różnicy w czasach relaksacji pomiędzy tkankami co związane jest z ich różnym składem chemicznym. Ponieważ SM powoduje zmiany w ilości i strukturze mieliny (główny składnik istoty białej), obrazowanie magnetyczno-rezonansowe potencjalnie mogłoby wykryć te zmiany bazując na pomiarach zmian czasów relaksacji a w konsekwencji umożliwić wczesną diagnozę tej groźnej i do tej pory nieuleczalnej choroby.

Do skutecznego obrazowania mieliny, a stąd diagnozy SM, potrzebny jest jednak odpowiedni kontrast pomiędzy białą a szarą istotą. Niestety czasy relaksacji istoty białej i szarej, w szczególności czas  $T_2$ , są bardzo krótkie i porównywalne ze sobą co powoduje trudności natury technicznej w ich obrazowaniu i zróżnicowaniu na uzyskanych obrazach MR. Dlatego, aby otrzymać najwyższy możliwy kontrast, wymagany jest bardzo dobry stosunek sygnału do szumu (ang. SNR) oraz właściwa i zoptymalizowana sekwencja impulsowa. W pracy zastosowany został system do obrazowania oparty o magnes nadprzewodzący o natężeniu pola magnetycznego 9,4T wyposażony w cewkę kriogeniczną. Tak wysokie pole oraz chłodzona cewka pozwoliły na otrzymanie maksymalnego sygnału i stąd maksymalnej rozdzielczości obrazu. W celu pomiarów krótkich czasów relaksacji  $T_2$  mieliny badane były sekwencje obrazujące oparte o echo spinowe (SE) oraz dwu- i trójwymiarowe sekwencje tzw. ultra short echo time (UTE). W dalszej kolejności zastosowana została sekwencja inversion recovery ultra short echo time (IR-UTE), która dodatkowo wprowadziła ważenie czasem  $T_1$ .

Wyniki badań pokazały, że technika obrazowania IR-UTE pozwala na pomiary czasów relaksacji  $T_1$  i  $T_2$  mieliny w modelu zwierzęcym ale nie umożliwia obrazowania wielowarstwowego in vivo ze względu na długi czas pomiaru. Dlatego została także przetestowana sekwencja o nazwie "segmented magnetization prepared rapid gradient echo

(MP-RAGE)”, która pozwoliła na otrzymanie wysokiej jakości obrazów 3D istoty szarej i białej w akceptowalnym dla badań czasie akwizycji. Co więcej, testowane były różnego typu impulsy selektywne radiowej częstotliwości (rf), np. Version S, Mao oraz Levitt-Freeman, które pozwalają na odpowiednie ogniskowanie magnetyzacji w niejednorodnym polu  $B_0$  generowanym przez magnes i podatność magnetyczną próbki oraz w niejednorodnym polu  $B_1$  produkowanym przez cewkę powierzchniową użytą w badaniach. Impulsy te pozwalają na zmniejszenie artefaktów związanych z echemi stymulowanymi.

Badania *in vivo* poprzedzone były badaniami fantomów w celu znalezienia optymalnych parametrów sekwencji, kształtu impulsu rf oraz odpowiedniego ułożenia cewki powierzchniowej. Wyniki badań *in vivo* zostały potwierdzone badaniami *ex vivo* MRI o wysokiej zdolności rozdzielczej oraz badaniami histopatologicznymi.

Do badań zmian zawartości mieliny zastosowany został kupryzonowy model MS, w którym zmiany w istocie białej odzwierciedlają zmiany występujące u człowieka. W wyniku prac otrzymane zostały trójwymiarowe obrazy mózgu przy użyciu zoptymalizowanych sekwencji IR-UTE oraz MP-RAGE, które umożliwiły detekcję mieliny i jej zaniku. Następnie zostały obliczone średnie wartości sygnału w wybranych obszarach mózgu reprezentujących szarą i białą materię oraz płyn mózgowo-rdzeniowy. W celu kwantyfikacji wyników wykonano histogramy różnych warstw mózgu u myszy zdrowych i poddanych diecie kupryzonowej. Histogramy pokazały, że zawartość mieliny w ciele modelowatym i korze mózgowej jest statystycznie różna u zwierząt chorych w porównaniu z grupą kontrolną. Wyniki badań pokazały, że zastosowane metody obrazowania (IR-UTE oraz MP-RAGE) z użyciem krio-cewki w polu 9,4T uwidaczniają kontrast pomiędzy białą i szarą materią, przewyższając obecne metody oceny demielinizacji w mózgu mysim *in vivo*.

Cele pracy były następujące: 1) ocena wartości badawczej obrazowania magnetyczno-rezonansowego w wysokim polu magnetycznym mikrostruktur mózgu zawierających różne ilości mieliny w modelu mysim MS; 2) zbadanie czy obrazowanie rezonansowe w wysokim polu magnetycznym przy użyciu krio-cewki oraz odpowiednich sekwencji impulsowych może pokazać uszkodzenia mieliny występujące w kupryzonowym modelu zwierzęcym MS. Cele te zostały osiągnięte i wyniki pokazały, że zoptymalizowany system pracujący w polu 9.4T, może istotnie być użyty do oceny ubytków w zawartości mieliny w mózgu myszy w modelu zwierzęcym MS. Wyniki pokazują potencjał zastosowania zaproponowanych metod obrazowania MR w przyszłych badaniach klinicznych stwardnienia rozsianego. Wszystkie badania na zwierzętach zostały przeprowadzone za zgodą Komisji Etyki.

## Summary

The thesis contains description of the application of the 9.4T MRI system using various pulse sequences and a radiofrequency (rf) cryo-coil to study demyelination in the animal model of multiple sclerosis (MS).

Many neurodegenerative diseases, among them MS, are currently diagnosed in late stage due to the lack of proper technique that could enable pre-symptomatic diagnosis, hence efficient treatment. MRI provides superior contrast that depends not only on tissue density and water content but on tissue relaxation times, hence their chemical composition. Because MS is associated with changes in myelin (the major part of white matter) structure and its content, MRI could potentially detect these alterations based on relaxation measurements providing early MS diagnosis. However, for efficient imaging of myelin, and thus potential detection of MS, high contrast between white matter (WM) and gray matter (GM) is needed. Unfortunately, their relaxation times (in particular  $T_2$ ) are short and comparable to each other, causing difficulties in their differentiation. Furthermore, very short  $T_2$  of myelin makes its direct visualisation difficult. Therefore, to obtain maximum contrast, high signal-to-noise ratio (SNR), a proper and optimal pulse sequence must be selected. We applied the 9.4T MRI system equipped with a cryo-coil for maximum sensitivity hence image resolution. To detect short  $T_2$  values of myelin we investigated application of spin echo (SE) based and ultra short echo time (UTE) pulse sequences. To further enhance capability of the method to detect myelin we applied the inversion recovery UTE (IR-UTE) pulse sequence with non-selective inversion rf pulse to provide additional  $T_1$  weighting.

The studies showed, the IR-UTE pulse sequence is indeed suitable for  $T_1$  and  $T_2$  myelin measurements in the animal model, but it requires long acquisition time for multi-slice MRI. Therefore, we applied the segmented magnetization prepared rapid gradient echo (MP-RAGE) pulse sequence that provided high quality 3D images of white and gray matter. Furthermore, we also investigated refocusing efficacy of various types of selective rf pulses, such as Version S, Mao and Levitt-Freeman. These pulses allow improved spin refocusing in inhomogeneous  $B_1$  produced by the surface RF coil and inhomogeneous  $B_0$  generated by the magnet and susceptibility of samples, hence avoiding artifacts caused by stimulated echoes.

*In vivo* experiments were preceded with phantom studies to find the optimal parameters of the pulse sequences, shape of the rf pulse and rf coil configuration. The *in vivo* results were confirmed with high resolution *ex vivo* MRI and with histopathology.

A cuprizone mouse model of MS was used to mimic myelin lesions (demyelination) occurring in MS patients. The 3D MR images of the brain were obtained using the IR-UTE and MP-RAGE pulse sequences with optimized parameters for myelin detection and changes of its content. The average signal intensities of different brain regions representing white matter (WM), gray matter (GM) and cerebro-spinal fluid (CSF) were calculated. To quantify the results, histograms of different slices in control and cuprizone treated animals were calculated. The histograms showed differences in the control and cuprizone treated animals, in particular, they showed that loss of myelin in the corpus callosum (cc) and cerebral cortex was statistically significant between healthy and cuprizone-treated animals. We concluded that the application of the IR-UTE and MP-RAGE methods provided excellent WM/GM contrast improving the current assessment of demyelination in a mouse brain *in vivo*.

The aim of the thesis was to: 1) assess the capability of high field MRI to image brain microstructures containing various amount of myelin in the mouse brain; 2) investigate if high field MRI can be optimized to assess myelin lesions occurring in the cuprizone mouse model of MS. These aims were accomplished and the thesis results show that the 9.4T MRI system, when the cryo-coil is used and the pulse sequences are optimized, can be indeed used to assess myelin losses in the animal model of MS, showing potential for future clinical applications of the proposed method for MS diagnosis.

All animal experiments were approved by the local Ethical Committee.

## Publications and peer-reviewed conference materials used in the thesis:

- W. Piędzia, K. Jasiński, K. Kalita, B. Tomanek, W.P. Węglarz. White and gray matter contrast enhancement in MR images of the mouse brain in vivo using IR UTE with a cryo-coil at 9.4 T; *Journal of Neuroscience Methods*; 232:30–35, 2014.
- W. Piędzia, K. Jasiński, K. Kalita, B. Tomanek, W.P. Węglarz. MRI of myelin as a potential tool for early diagnosis of multiple sclerosis; Proc. 6<sup>th</sup> Congress of the Pan-Asian-Committee-for-Research-and-Treatment-of-Multiple-Sclerosis (PACTRIM), Kyoto, Japan, Nov 6-8, 2013, *Multiple Sclerosis Journal*, 20(7):920, 2014.
- W. Piędzia, K. Jasiński, K. Kalita, B. Tomanek, W.P. Węglarz. Detection of myelin changes in vivo using high field MRI; Proc. 8<sup>th</sup> Congress of the Pan-Asian-Committee-for-Research-and-Treatment-of-Multiple-Sclerosis (PACTRIMS), Seoul, South Korea, Nov 19-21, 2015; *Multiple Sclerosis Journal*, 22(3):413, 2016.
- W. Piędzia, K. Jasiński, K. Kalita, B. Tomanek, W.P. Węglarz. T<sub>1</sub> relaxation measurements in the mouse brain in vivo using Variable Flip Angle - UTE with a cryo-coil at 9.4 T; 23<sup>rd</sup> *Joint Annual Scientific Meeting Intl. Soc. Mag. Reson. Med. – European Int Soc Mag Res Med Biol* (3238), Milan, Italy, May 10-16, 2014.
- W. Piędzia, K. Jasiński, K. Kalita, B. Tomanek, W.P. Węglarz. Enhancement of the myelin rich regions in MR images in the mouse brain in vivo using IR-UTE with a cryo-coil at 9.4 T; 21<sup>st</sup> *Annual Scientific Meeting Int. Soc. Mag. Reson. Med.* (2392), Salt Lake City, UT, USA, April 20-26, 2013.
- W. Piędzia, K. Jasiński, K. Kalita, B. Tomanek, W.P. Węglarz. Application of a cryo-coil and modified pulse sequences for relaxation study of the mouse brain in vivo at 9.4T; 30<sup>th</sup> *Annual Scientific Meeting ESMRMB* (527), Toulouse, France, Oct 3-5, 2013. *MAGMA*; 26(Suppl 1), 2013.
- W. Piędzia, K. Jasiński K, W. Węglarz. Comparison of different MRI pulse sequences for quantitative T<sub>2</sub> measurements in preclinical studies; 29<sup>th</sup> *Annual Scientific Meeting ESMRMB* (708), Lisbon, Portugal, Oct 4-6, 2012.
- Piędzia W, Bock N, Jasiński K, Kalita K, Stanisiz G, Węglarz WP, MR imaging of the mouse brain using cryo-coil at 9.4T - histology in vivo? Abstr. of the *XLV Polish Seminar on Nuclear Magnetic Resonance and Its Applications*, 1-2 December 2014, Krakow, in IFJ Report, 2077/AP 2014, p. 37 (not peer-reviewed)

## Content:

Abbreviations.....	10
1. Introduction	
1.1 Detection of the MR signal.....	11
1.2 Relaxation times.....	15
1.3 Principles of MR Imaging.....	18
1.4 Selective and non-selective rf pulses.....	20
1.5 MR Imaging techniques for detection of multiple sclerosis.....	21
1.6 <i>In vivo</i> measurements of short T <sub>2</sub> relaxation times.....	28
1.7 Identification of small brain structures in MRI.....	33
2. Multiple sclerosis (MS)	
2.1 Etiology and diagnostic methods of MS.....	39
2.2 Immunology and pathophysiology of MS.....	41
2.3 Treatment of MS and myelin detection methods.....	43
2.4 Application of MRI to diagnosis of MS.....	44
3. Experimental Section	
3.1 Animal model of MS.....	49
3.2 Selection of the MRI techniques for the study of demyelination in the animal model of MS.....	51
3.2.1 Application of modified spin-echo pulse sequences for quantitative T <sub>2</sub> imaging.....	52
3.2.2 Application of the IR-UTE pulse sequence.....	55
3.2.3 The Method of classification of the brain structures.....	57

3.2.4 Identification and quantification of the brain structures in the mouse brain <i>in vivo</i> using the IR-UTE pulse sequence.....	59
3.2.5 Application of the MP-RAGE pulse sequence for <i>in vivo</i> imaging of demyelination in the mouse model of MS.....	65
3.2.6 Quantitative evaluation of demyelination volume in <i>ex vivo</i> MP-RAGE images of the mouse brain.....	72
3.3 Histological assessment of demyelination in the brain of the MS mouse model.....	75
4. Discussion and Conclusions.....	77
5. References.....	80

## List of used abbreviations

AC – cerebral aqueduct  
APC – Antigen Presenting Cell  
BBB – blood brain barrier  
CA – cornu ammonis  
CC – corpus collosum  
cc – corpus callosum  
CNR – contrast to noise ratio  
CNS – Central Nervous System  
CSF – cerebrospinal fluid  
CX – cerebral cortex  
DG – dentate gyrus  
FH – fimbria hippocampi  
GE – gradient echo  
GM – gray matter  
ic – internal capsule  
EC/IC - extra and intracellular water)  
IR – inversion recovery  
LV/RV – left/right ventricles  
MRI – magnetic resonance imaging  
MS – multiple sclerosis  
OP – optic nerve layer of the superior colliculus  
PAG - -peri-aqueductal gray matter  
PD – Parkinson’s Disease  
SE – spin echo  
SNR – signal to noise ratio  
TE – echo time  
Th – thalamus  
TI – inversion time  
TR – repetition time  
UTE – ultra short echo  
V3 – third ventricle  
WM – white matter

# 1. Introduction

Multiple sclerosis (MS) is a neurodegenerative disease of the central nervous system (CNS) leading to disorder of higher brain functions such as memory, speech or abstractive thinking. MS is associated with changes in myelin structure and composition within the CNS (Weinshenker, 1996). The disease is diagnosed mostly based on symptoms or examination of the cerebrospinal fluid (CSF). MS cause is unknown and typically presents in adults 20 to 45 years of age (Cree, 2007). It is the most common cause of disability among young adults (Ebers, 1993; Kobelt, 2017). About two third of MS patients are women. Unfortunately, there is no efficient cure for MS, treatment is symptomatic and aimed at maintaining quality of life (Brunton, 2005).

There was 2.8 mln people affected by MS in 2020 worldwide (Walton, 2020) and over 46 000 in Poland alone (NFZ, 2021). The incidence of MS in both developed and developing countries is rising (Browne, 2014). Considering huge impact of MS on our society and lack of early and suitable diagnostic techniques, research (such as the one presented in the thesis) focusing on new methods of early and non-invasive detection of demyelination is justified. Should such method exist, MS could be possibly treated at early stages providing opportunities for efficient therapy. Therefore, the overall aim of the thesis was to develop and propose a method based on MRI enabling early detection of demyelination in the brain hence early MS diagnosis.

## 1.1. Detection of the MR signal

Magnetic Resonance Imaging (MRI) has been developed in 1970-ties and soon after found clinical applications. It is based on the nuclear magnetic resonance (NMR) phenomena, discovered by Isidor Rabi in 1938 (Rabi, 1938), who was awarded the Nobel Prize in Physics. In 1941, Yevgeny Zavoisky also observed the phenomena of nuclear magnetic resonance. Felix Bloch and Edward Mills Purcell expanded the Rabi's approach developed in atoms in vacuum and applied it to liquids and solids showing application of electromagnetic fields to chemical analysis (Purcell 1946; Bloch, 1946). They shared the Nobel Prize in Physics in 1952 "for their development of new methods for nuclear magnetic precision measurements and discoveries in connection therewith". Further work by Erwin Hahn who discovered spin echo (Hahn, 1950) provided basis for progress in NMR (Abragam, 1961; Andrew, 1955,

Torrey, 1956, 1960). This work was continued by Carr and Purcell who applied a series of 180° refocusing pulses (Carr, 1954) and showed their applications for diffusion measurements. Further works in the area was conducted by Richard Ernst, who introduced the Fourier Transform to NMR (Ernst, 1965) and was awarded the Nobel Prize in Chemistry in 1991 “for his contributions to the development of the methodology of high resolution nuclear magnetic resonance (NMR) spectroscopy”. Finally, Paul Lauterbur and Peter Mansfield introduced modulation of the external magnetic field by applying time dependent gradients of the main magnetic field that enabled MR Imaging. This discovery was awarded with the Nobel Prize in Medicine to both Lauterbur and Mansfield in 2004 (Lauterbur, 1973; Mansfield, 1973).

The principles of MRI arise from the interaction of a proton spin with an external magnetic field ( $\vec{B}_0$ ). Proton spins with a magnetic moment ( $\vec{\mu}$ ), when placed in the external magnetic field ( $\vec{B}_0$ ) precess along the direction of  $\vec{B}_0$  with the angular frequency  $\vec{\omega}$  according to the formula:

$$\vec{\omega} = -\gamma\vec{B}_0 \quad [\text{Eq 1}]$$

where  $\gamma$  is called the gyromagnetic ratio, and the frequency  $\omega$  is called the Larmour frequency.

When placed in the magnetic field small fraction of spins aligns parallel to the field. The sum of these spins creates a net magnetisation  $M_0$  (Abragam, 1961):

$$M_0 = \frac{\rho_0 \gamma^2 \hbar^2}{4kT} B_0 \quad [\text{Eq 2}]$$

where  $\rho_0$  is the spin density (number of protons per unit volume),  $\hbar = h/2\pi$ , where  $h$  is the Planck’s constant,  $k$  is the Boltzmann’s constant,  $T$  is the absolute temperature.

To observe the NMR signal, the magnetisation is moved out of equilibrium by the application of an external pulse with the frequency corresponding to the Larmour frequency. As this frequency is in the order of 100 MHz it is called a radiofrequency (rf) pulse. The rf

pulse that tips the magnetisation by  $90^\circ$  is called  $90^\circ$  or  $\pi/2$  pulse. This rotating magnetisation is detected by rf coils as the voltage induced by the electromotive force (*emf*) (Hoult, 2011):

$$emf = -\oint \frac{d}{dt} (\vec{M} \vec{B}_{rf}) dV \quad [\text{Eq 3}]$$

where  $\vec{B}_{rf}$  is the field produced by the rf coil with a unit current.

Combining [Eq 2] and [Eq 3] we get formula for the NMR signal *S*:

$$S \sim \frac{B_0^2 \rho_0}{T} \quad [\text{Eq 4}]$$

As noise in an NMR experiment is proportional to the frequency (hence  $B_0$ ) the signal to noise (SNR) is proportional to  $B_0$ :

$$SNR \sim B_0 \quad [\text{Eq 5}]$$

The above equation explains the tendency of applying stronger magnetic fields to increase NMR sensitivity hence image resolution

Beside electronic noise the major noise contribution comes from the rf coil due to its resistance. Neglecting radiation losses, the noise picked up by the receiver (*N*) is proportional to the sum of the effective resistance of the sample ( $R_s$ ) and the resistance of the coil itself ( $R_c$ ):

$$N \sim \sqrt{R_s + R_c} \quad [\text{Eq 6}]$$

The resistance of the sample comes from two sources: dielectric losses (that can be minimized using distributed capacitance and proper capacitor shielding) and inevitable inductive losses associated with rf induced eddy currents within the sample.

The noise originating from the rf coil depends on temperature and is expressed by the Johnson-Nyquist equation (Pierce, 1956):

$$N \sim \sqrt{4kTR(T_c)\Delta f} \quad [\text{Eq 7}]$$

where  $k$  is Boltzmann constant,  $\Delta f$  is the receive bandwidth and  $R(T_c)$  is the resistance of the material which the coil is made of. This relationship allows to increase SNR by decreasing temperature of the rf coil as its resistance is proportional to temperature:

$$R = R_0(1 + \alpha\Delta T) \quad [\text{Eq 8}]$$

where  $\alpha$  is temperature coefficient of resistance (copper  $\alpha = 3.9 \times 10^{-3}/^\circ\text{C}$ ).

This phenomenon was used by Bruker, producer of preclinical MRI systems, to make so called cryo-probe (Fig 1.1) that is kept in gaseous helium at temperature  $-253^\circ\text{C}$  (20K). As electronic noise also decreases with temperature, preamplifier is also kept at low temperature of 77K. Furthermore, the quadrature configuration of the coil allows additional gain in SNR by  $\sqrt{2}$  (Hoult, 1984). This design allowed 3- to 12-fold (depending on the slice position) SNR increase in mouse brain imaging when compared to a volume rf coil (Piędzia, 2014). This increase corresponds to 9 to 144 times reduction of the acquisition time with the same SNR when using a room temperature coil.



**Fig. 1.1** Bruker cryo-coil (cryoprobe) used in the thesis: radius 11mm, temp. 20K, preamplifier cooled to 77K. (<https://www.bruker.com/en/products-and-solutions/preclinical-imaging/mri/MRI-CryoProbes/rat-array-mri-cryoprobe.html>)

## 1.2 Relaxation times

For the consideration of relaxation times let's assume the external  $B_0$  field is applied along  $\vec{z}$  direction, such as:

$$\vec{B}_{ext} = B_0 \hat{z} \quad [\text{Eq. 9}]$$

Then behaviour of the magnetisation can be described by the Bloch equation:

$$\frac{d\vec{M}}{dt} = \gamma \vec{M} \times \vec{B}_{ext} + \frac{1}{T_1} (M_0 - M_z) \hat{z} - \frac{1}{T_2} \vec{M}_\perp \quad [\text{Eq 10}]$$

where  $\vec{M}_\perp = M_x \hat{x} + M_y \hat{y}$ ,  $T_1$  is the spin-lattice relaxation time,  $T_2$  is the spin-spin relaxation time.

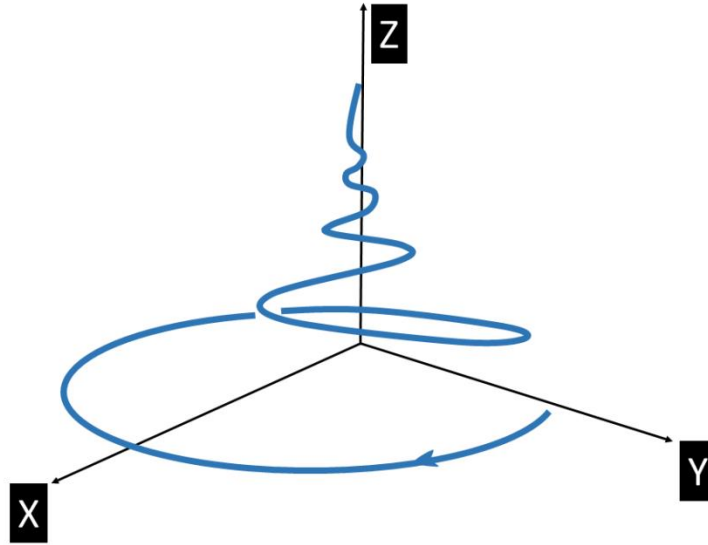


**Fig. 1.2** Trajectory of the tip of the magnetisation vector after applying  $90^\circ$  pulse along  $y$  axis showing return of the magnetisation to equilibrium. Decay of the transverse magnetisation is visible (Haacke, 1999 with permission)

The solutions of the [Eq 10] are:

$$\begin{aligned}
 M_x(t) &= e^{-t/T_2} (M_x(0) \cos \omega_0 t + M_y(0) \sin \omega_0 t) \\
 M_y(t) &= e^{-t/T_2} (M_y(0) \cos \omega_0 t - M_x(0) \sin \omega_0 t) \\
 M_z(t) &= M_z(0) e^{-t/T_1} + M_0 (1 - e^{-t/T_1})
 \end{aligned}
 \tag{Eq. 11}$$

The regrowth of the magnetisation  $M_z$  with the time  $T_1$  (Fig 1.2 and Fig 1.3a) is caused by the interaction of the spins with their atomic surroundings, namely the lattice, hence the name spin-lattice relaxation time. For example, following  $90^\circ$  pulse the  $M_z$  regrowth is given by:

$$M_z(t) = M_0 (1 - e^{-t/T_1})
 \tag{Eq 12}$$

and for the transverse magnetisation:

$$\vec{M}_{\perp}(t) = \vec{M}_{\perp}(0)e^{-t/T_2} \quad [\text{Eq 13}]$$

The transverse relaxation ( $T_2$ ) is caused by spin-spin interactions causing dephasing of spins due to variations of the local magnetic field.

The above equation [Eq. 13] is true for a perfectly homogeneous magnetic field  $\vec{B}_0$ . In a more realistic case of inhomogeneous magnetic field [Eq 13] must be rewritten to:

$$\vec{M}_{\perp}(t) = \vec{M}_{\perp}(0)e^{-t/T_2^*} \quad [\text{Eq 14}]$$

where:

$$\frac{1}{T_2^*} = \frac{1}{T_2} + \frac{1}{\gamma\Delta B} \quad [\text{Eq 15}]$$

$\Delta B$  expresses inhomogeneity of the main field associated with imperfections of the magnet design and with the sample. The inhomogeneity increases relaxation.

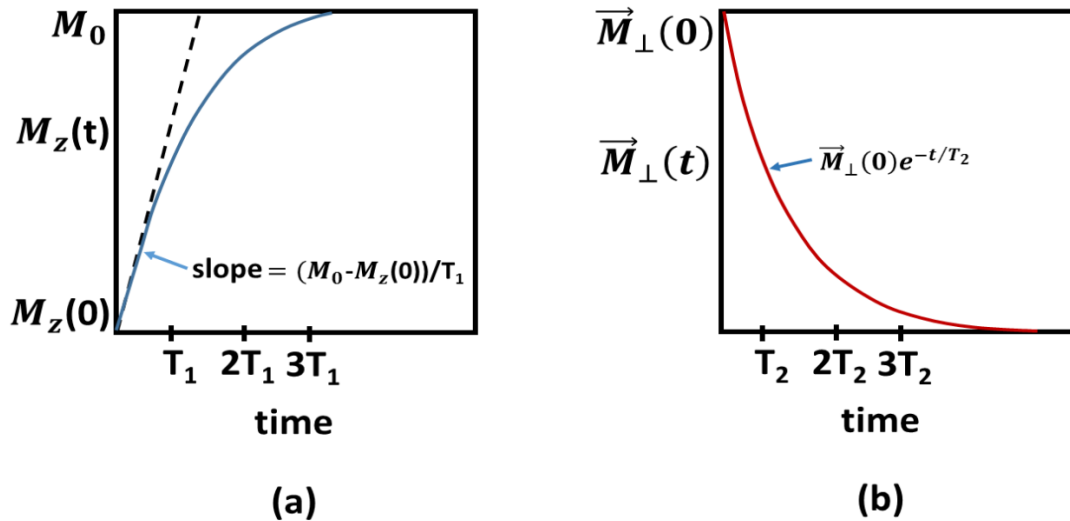


**Fig. 1.3** (a) The return of the longitudinal magnetisation from the initial value  $M_z(0)$  to the equilibrium  $M_0$ . (b) The decay of the transverse magnetisation from the initial value (Haacke, 1999 with permission).

### 1.3 Principles of MR Imaging

To obtain an MR image the NMR signal in time domain must be converted to provide information about spatial spin density  $\rho(\vec{r})$ . To achieve this, three orthogonal linear external time-variable gradients of the magnetic field along with rf field are applied:

$$\vec{B}(\vec{r}, t) = \vec{B}_0 + \vec{r}G(t) \quad [\text{Eq 16}]$$

where

$$G = \frac{\partial B_z}{\partial r} \quad [\text{Eq 17}]$$

For spins placed along  $z$  direction their frequency depends on their position as follows:

$$\omega_G(z, t) = \omega_0 + \gamma z G(t) \quad [\text{Eq. 18}]$$

If the gradient is applied only after the rf pulse for the time  $t$  the spins will accumulate the phase:

$$\Phi_z(z, t) = - \int_0^t \omega_G(z, t') dt' = -\gamma z \int_0^t G(t') dt' \quad [\text{Eq 19}]$$

Then the NMR signal is given by:

$$S(t) = \int \rho(z) e^{-i\Phi_g(z,t)} dz \quad [\text{Eq 20}]$$

The above equation can be rewritten as:

$$S(k) = \int \rho(z) e^{-i2\pi k z} dz \quad [\text{Eq 21}]$$

where:

$$k = \frac{\gamma}{2\pi} \int_0^t G(t') dt' \quad [\text{Eq 22}]$$

If the gradient  $G$  is constant over the entire time  $t$ , the [Eq 22] can be written as:

$$k = \frac{\gamma}{2\pi} Gt \quad [\text{Eq 23}]$$

As seen signal  $S(k)$  is the Fourier transform (FT) of the spin density of the sample. Therefore, the spin density can be found using the inverse FT of the signal:

$$\rho(z) = \int S(k) e^{i2\pi kz} dk \quad [\text{Eq 24}]$$

While the above equations describe 1D case, they can be expanded into 3D imaging by applying 3 gradients of the magnetic field:

$$S(k_x, k_y, k_z) = \iiint \rho(x, y, z) e^{-i2\pi(k_x x + k_y y + k_z z)} = FT[\rho(x, y, z)] \quad [\text{Eq 25}]$$

Collecting the signal  $S$  when the gradients are applied allows the entire 3D  $k$ -space to be filled up and the spatial distribution of spin density  $\hat{\rho}(\vec{r})$  (an image) can then be obtained by the inverse FT of the collected data:

$$\hat{\rho}(\vec{r}) = FT^{-1}[S(\vec{k})] = \int S(\vec{k}) e^{i2\pi \vec{k} \vec{r}} d^3k \quad [\text{Eq 26}]$$

The above equation enabled application of various pulse sequences comprising single and multiple spin excitations and various configurations of gradients, such as spin echo (SE), gradient echo (GE), fast spin echo (FSE), ultra-short echo time (UTE) etc.

## 1.4 Selective and non-selective rf pulses

There are two major types of rf pulses used in MRI: slice selective (known as “soft”) and non-selective (known as “hard”) pulses. The frequency spectrum of a hard pulse is very broad (Fig 1.4a) not allowing selection of a specific slice or volume. The spectrum of an ideal soft pulse is rectangular and allows slice selection when applied simultaneously with a gradient of the magnetic field. An example of a soft pulse (sinc) is shown in Fig 1.4b.

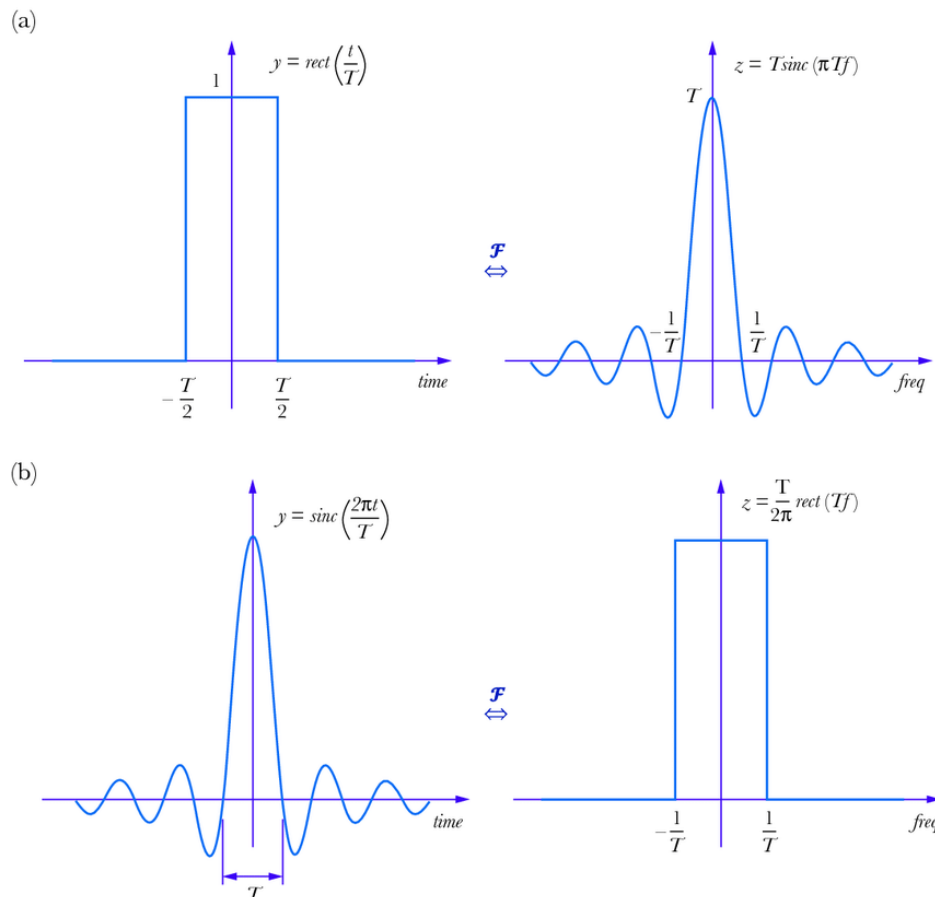


**Fig. 1.4** Visualisation of rf pulses and their Fourier Transforms (FT): (a) rectangular (non-selective) pulse, (b) selective (sinc) pulse (FT applied to the sinc pulse assumed to be infinite) (free non-commercial licence from Research Gate).

A perfectly rectangular spectrum is produced only by an infinite soft pulse (note: Fig 1.4b shows limited pulse length). In practice this is impossible because the acquisition of an MR image must be as fast as possible therefore the pulses must be as short as possible. The frequency spectra of such non-infinite pulses are not perfectly rectangular and produce frequency modulations at the edges of their spectrum (Fig 1.5). Application of these selective

rf pulses causes image artifacts and errors in MR data quantification, such as  $T_2$  measurements. While there are methods (e.g. Bottomley 1984; Henning, 1988) minimizing these effects, they remain obstructive in imaging of samples with very short  $T_2$  such as myelin as discussed in the following sections.

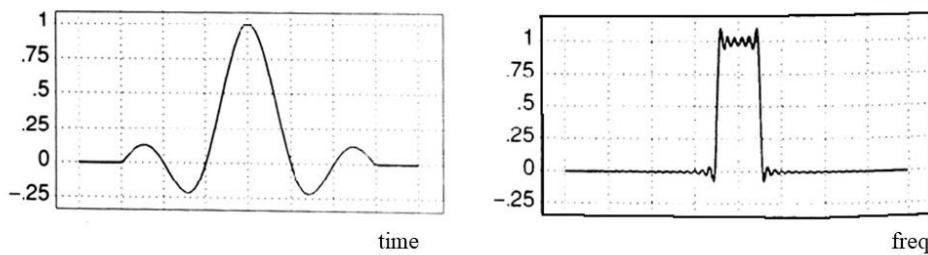


**Fig. 1.5** The finite selective (“soft”) sinc rf pulse (left) and its Fourier Transform (right). The imperfections of the rectangular spectrum are visible due frequency modulations. (Seppo Äyräväinen Hut, free licence)

## 1.5 MR Imaging techniques for detection of multiple sclerosis

It was shown that MRI can be used for detection of MS in different stages corresponding to different degrees of demyelination (Piędzia, 2013). MRI techniques enabling imaging of the myelin-deficient brain areas hence MS, are mainly based on  $T_2$ -weighting (Larson, 2006; Piędzia, 2014). The pulse sequences used for this type of measurements include: spin echo (SE) and gradient echo (GE) with short and ultra-short echo time (Wilhelm, 2012). The  $T_1$  and  $T_2$  contrast in these sequences can be further utilized and enhanced by the application of the magnetisation prepared rapid acquisition gradient echo (MP-RAGE) (Fellner, 1996) and using inversion recovery ultra-short echo time (IR-UTE) sequences (Tyler, 2007). These techniques allowed contrasting different brain structures associated with WM and GM in animals and in humans (MacKay, 1994; Chavez, 2012; Piędzia, 2014, Pirreda 2020; Filippi, 2021; Piredda, 2021).

The most common pulse sequence used in standard MRI is based on the spin echo (SE). It consists of the slice selective  $90^\circ$  rf excitation pulse applied simultaneously with the “slice” gradient, allowing spin excitation only within the selected slice, followed by the  $180^\circ$  selective pulse (Fig 1.6). These pulses create an MR signal, called “spin echo”. The echo

occurs at the exactly the same time after the  $180^\circ$  pulse as is the time interval between  $90^\circ$  and  $180^\circ$  pulses (Hahn, 1950). Application of the phase encoding gradient and read gradient allows spatial distribution of the spins to be calculated using the Inverse Fourier Transform (Eq 26; Hutchison, 1978). The major advantage of the SE pulse sequence is the ability to obtain any contrast weighting:  $T_1$ -,  $T_2$ - or proton density by manipulating echo time (TE) and repetition time (TR) values. This capability allowed high contrast MR images of soft tissue to be obtained in early 80-ties (Hendrick, 1984; Perman, 1984). The SE pulse sequence is less sensitive to inhomogeneities of the magnetic field caused by imperfections of magnet shimming or susceptibility effects than other pulse sequences, such as gradient echo (GE). This is caused by the application of the  $180^\circ$  pulse that refocuses off-resonance effects, reducing possible image artifacts caused by magnetic field inhomogeneities. Other consequence is the possibility of using long TE allowing strong  $T_2$ -weighting, despite short  $T_2^*$ , that is not possible in the gradient echo pulse sequence.

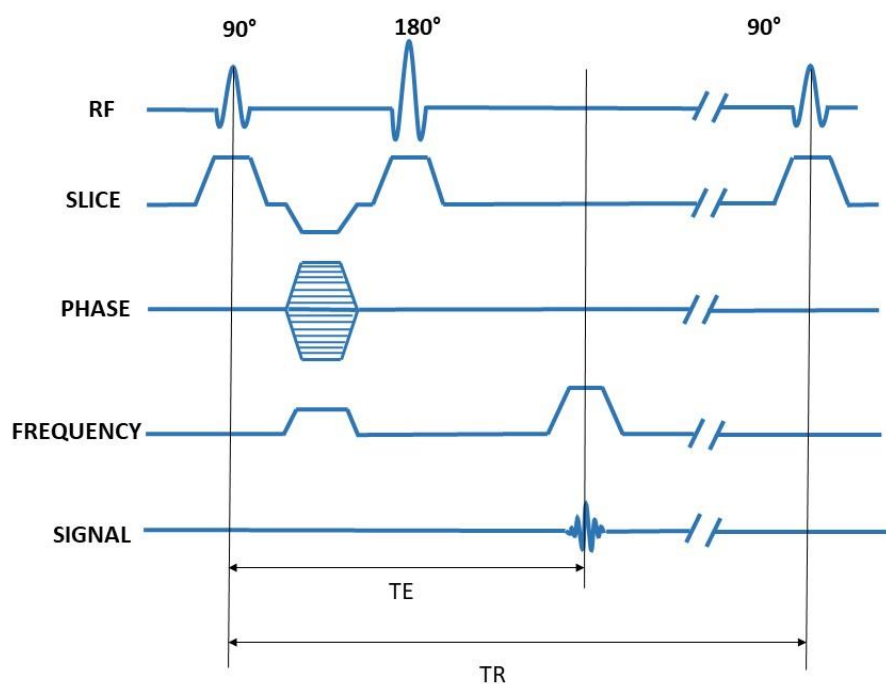


**Fig. 1.6** The spin echo (SE) pulse sequence with selective  $90^\circ$  and  $180^\circ$  rf pulses: TR – repetition time, TE – echo time. The sequence is repeated for each phase encoding step with TR time. (Author’s drawing based on open access <https://www.intechopen.com/>)

SE based MR imaging can be obtained with a single echo or multiple echoes using one or multiple  $180^\circ$  rf pulses respectively. Each echo can be used to create an MR image with different TE hence different  $T_2$ -weighting. To obtain  $T_2$ -weighted image both TR and TE must be long, that causes long imaging scanning. For example, to collect an MR image with resolution  $256 \times 256$ , typical TR is 5000 ms, TE = 50 ms, that leads to the total acquisition time of over 21 min ( $256 \times 5$  sec). While SE imaging allows multiple images to be obtained within TR, the major disadvantage of the sequence remains long total acquisition time. Moreover, in practice, to obtain high enough SNR, signal averaging is needed further increasing total scan time.

To deal with long SE scan time a pulse sequence based on gradient echo (GE) was introduced (Frahm, 1986). The gradient echo pulse sequence uses gradient reversal along frequency encoding direction instead of a refocusing pulse to produce a gradient echo. The echo creating gradient first dephases the spins and then rephases them when applied in opposite direction. This pulse sequence may be used with rf selective pulses as well as in a 3D version using hard pulses (Fig. 1.7). The GE pulse sequence is much faster than SE because lower than  $90^\circ$  excitation pulses may be used and refocusing pulse is not required. This allows application of short repetition times as magnetisation recovery is much faster than after  $90^\circ$  and  $180^\circ$  pulses. Typical GE pulse sequences use  $5^\circ$ - $30^\circ$  flip angle and TR of 3-50 ms, that gives total acquisition time for  $256 \times 256$  images of  $\sim 0.8$  -  $\sim 13$  sec. However, as no refocusing pulse is used, GE provides  $T_2^*$  weighting (unlike SE that provides  $T_2$ -weighting) and as such depends on inhomogeneities of the magnetic field. Due to low flip angle it also provides lower SNR than SE. However, it can be utilized to obtain susceptibility weighted imaging (SWI) (Haacke 2004) and can be used in functional MRI (fMRI) (Logothetis, 2008)

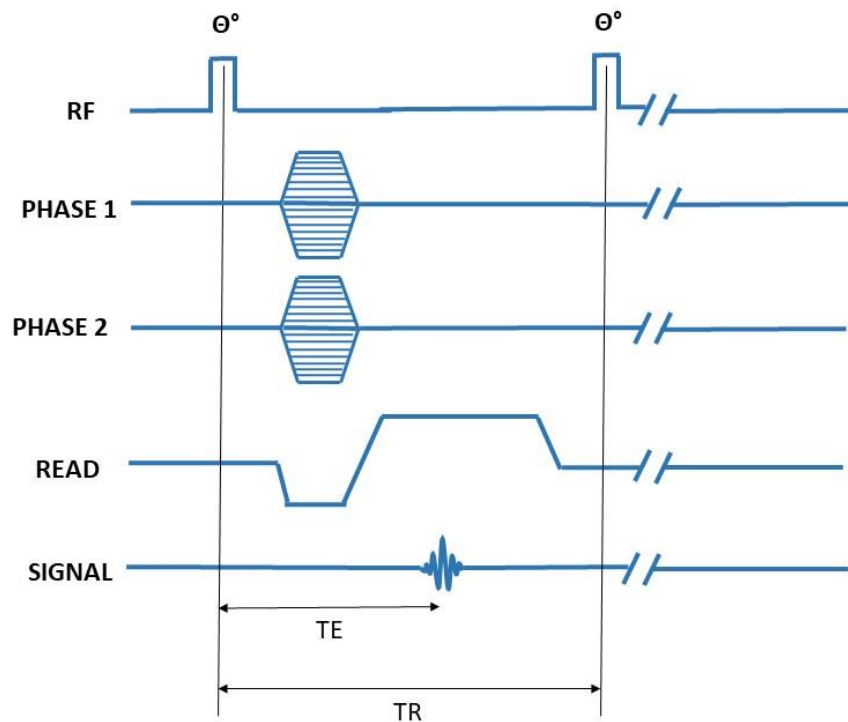


**Fig. 1.7** The 3D FLASH pulse sequence: TR – repetition time, TE – echo time. The read gradient is used to create a gradient echo and for frequency encoding. (Based on Frahm 1986, with permission)

Imperfections of  $180^\circ$  refocusing pulses (for example due to their non-infinite length) used in the SE pulse sequence cause stimulated echoes (Hahn, 1950) creating image artifacts. To minimize these unwanted spurious echoes application of a spoiler gradient and non-selective refocusing pulses was proposed (Fig 1.8). A spoiler gradient consists of two lobes with the same direction applied before and after the rf refocusing pulse. The amplitudes of the gradients and their polarities may differ for multiple rf refocusing pulses to effectively reduce unwanted signals by manipulating the phase coherence of transverse magnetisation (Poon, 1992). The other option is to use phase-cycling by applying rf pulses with different phases causing dephasing of unwanted signals (Bain, 1984).

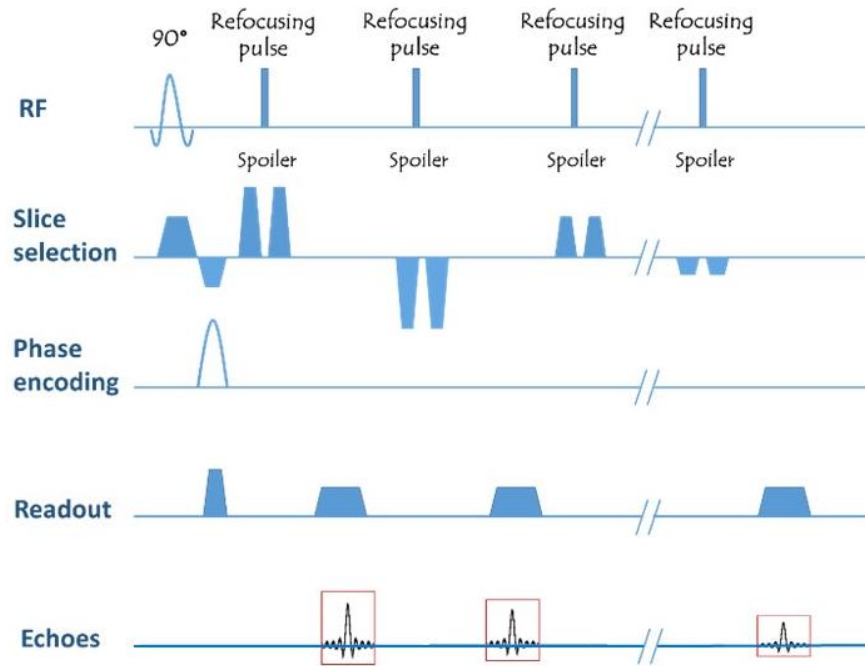


**Fig. 1.8** Spin echo (SE) based pulse sequences reducing artifacts using spoiling gradients and a selective rf  $90^\circ$  pulse, for example the “Version S” (base on Poon, 1992, with permission).

While the above listed pulse sequences are suitable for soft tissue imaging they cannot be used for tissues with very short  $T_2$  ( $< \sim 1\text{ms}$ ) such as bones or some structures in the brain (e.g. myelin). To address this need, pulse sequences with small flip angle, so called ultra-short echo time (UTE) were developed (Tyler, 2007; Robson, 2003). The UTE pulse sequences use half excitation pulse and radial data acquisition (Robson, 2003) (Fig. 1.9). The application of the half pulse allows signal detection even from tissues with very short  $T_2$  while radial k-space sampling maximizes available SNR. The rf pulse is truncated, applied with the negative slice selection gradient in the first half and positive in the second half of the pulse sequence, and it is followed by the rapid acquisition and simultaneously applied phase and read encoding gradients for radial acquisition (Tyler, 2007; Robson, 2003).

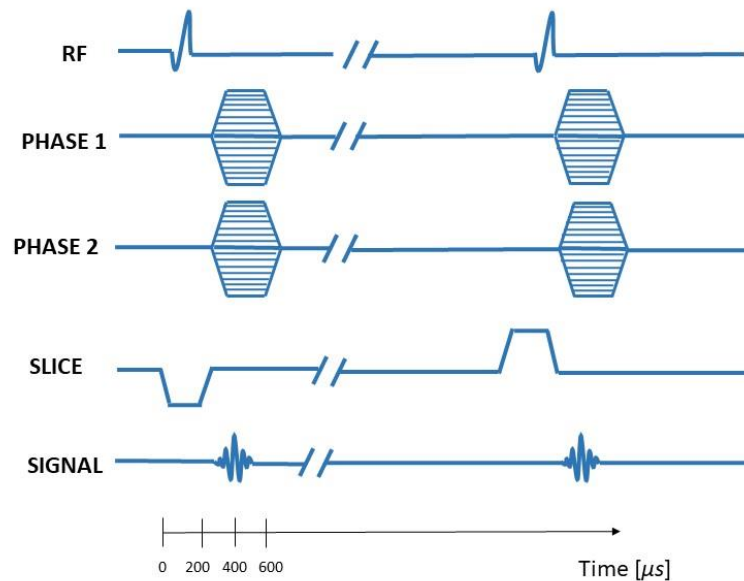


**Fig. 1.9** The ultra-short echo time (UTE) pulse sequence diagram (based on Tyler, 2007, with permission)

The UTE pulse sequence may be preceded by other rf pulses, such as variable-rate selective excitation (VERSE), inversion recovery pulse (IR-UTE) eliminating signal from tissues with long  $T_1$  or suppression recovery (SR-UTE) eliminating long  $T_2$  components.

To combine  $T_1$ -weighted fast imaging with short TE allowing short  $T_2$  tissue detection the three-dimensional, magnetization prepared rapid gradient echo (MP RAGE) pulse sequence (Fig 1. 10) was introduced (Brant-Zawadzki, 1992; Fellner, 1996). The MP-RAGE pulse sequence comprises a  $180^\circ$  inversion pulse, to obtain  $T_1$  contrast, followed by a 3D FLASH sequence with very short TR and TE, and very low flip angle. Following the inversion pulse all 3D phase encoding steps are performed by changing the slice-selection gradient ( $G_s$ ) step by step, keeping the 2D phase encoding gradient ( $G_p$ ) constant. After the recovery period the whole procedure is repeated changing  $G_p$  for the next 2D phase encoding step.

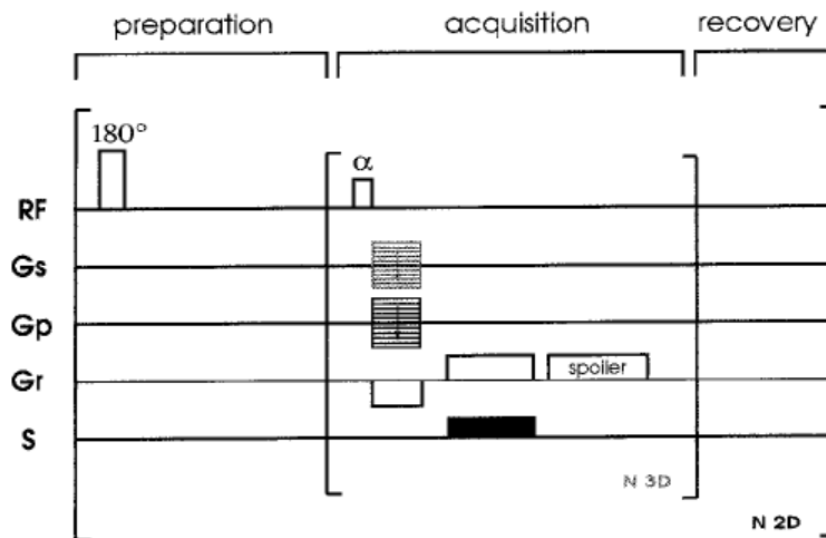


**Fig. 1.10** The MP-RAGE pulse sequence diagram (Fellner, 1996 with permission). The gradient echo imaging is preceded by a magnetisation preparation ( $180^\circ$  pulse).

## 1.6 *In vivo* measurements of short $T_2$ relaxation times

The method of measurement of the  $T_2$  relaxation time is well-known particularly in NMR spectroscopy. It is relatively straightforward using the CPMG pulse sequence ( $90^\circ$ - $180^\circ$ - $180^\circ$ - $180^\circ$ -...) with non-selective (“hard”) pulses for a sample with a single  $T_2$  component (Fig 1.11).

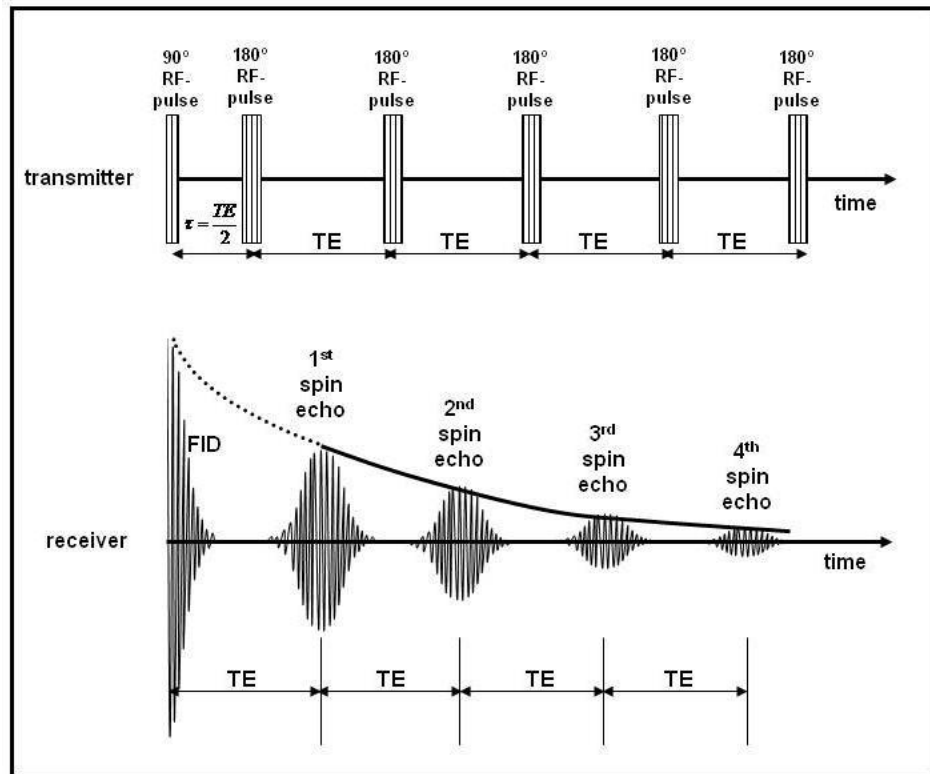


**Fig. 1.11** CPMG pulse sequence diagram used for  $T_2$  measurements. The figure shows non-selective pulses, but both selective or non-selective ( $90^\circ$  and  $180^\circ$ ) can be used for imaging. (Appel, 2011, with permission).

The CPMG pulse sequence is usually (particularly in NMR experiments) used to calculate  $T_2$  of various solid samples based on hundreds of echoes requiring long acquisition time, while *in vivo* MRI imposes limitation on total acquisition time. In addition, slice selection must be used disabling application of rectangular (“hard”) pulses (compare Fig 1.5). Application of selective pulses causes many artifacts associated with phase modulation of  $k$ -space data caused by various reasons, such as stimulated echoes, eddy currents, field inhomogeneities or improper refocusing of magnetisation due to imperfections of soft  $180^\circ$

pulses (Reeder, 1997). Furthermore, low SNR and limited acquisition time, hence limited number of echoes, introduce errors in fitting procedures of the echoes. Finally, signal from living organs is lower than from phantoms and comprises tissues of various  $T_2$  relaxation times bringing additional complications to data acquisition and its analysis. In particular, multi-exponential fitting must be used, that is sensitive to SNR, number of collected data points and their acquisition rate.

Other errors in  $T_2$  measurement are caused by inhomogeneities of the main field  $B_0$  and variations of the amplitude and phase of the rf field ( $B_1$ ) produced by rf coils (Fig. 1.12).

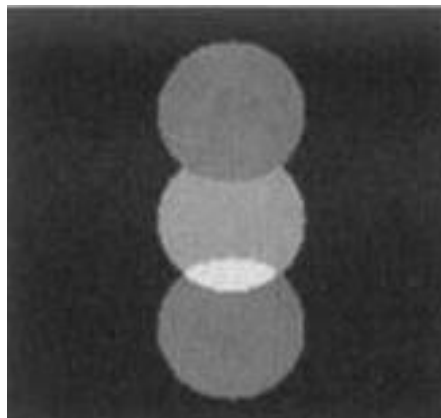


**Fig. 1.12** An example of an artifact caused by the phase modulation of k-space data that may occur in a multi-echo pulse sequence (Reeder, 1997, with permission).

Considering the above points, the criteria to ensure proper  $T_2$  measurements *in vivo* are: 1)  $180^\circ$  pulses should refocus the entire magnetization within the selected slice; 2) there should be no  $T_1$  weighting in the collected data ( $TR > 5T_1$ ); 3) there should be as many as possible echoes collected for proper fitting, particularly for multi-exponential fitting; 4) rf pulses should be insensitive to  $B_0$  and  $B_1$  inhomogeneities. To address these requirements, composite rf pulses are usually applied for quantitative  $T_2$  measurements, albeit with the price of longer TE.

Although  $B_0$  inhomogeneities are eliminated by the application of spin echo, this is only the case if selective pulses are perfectly  $90^\circ$  and  $180^\circ$ , which in practice is never accomplished mostly due to hardware imperfections (e.g. rf coils producing inhomogeneous  $B_1$  field, such as a surface coil) and time constraints (e.g. short time of echo train). These are

the sources of additional dephasing of echoes hence the measured  $T_2$  is shorter than the true one.

To ensure the proper echoes formation the profiles of the refocusing pulses must be as close to rectangular as possible. While standard sinc pulses could be used, they do not have perfectly rectangular spectra due to their limited time length (Fig 1.5). To generate ideal frequency-selective rf pulses, with perfectly rectangular spectra, composite rf pulses were proposed.

Composite pulses are composed of closely spaced rf pulses and have an equivalent effect on magnetisation as conventional single pulses but are less sensitive to the above mentioned imperfections (Levitt, 1979, 1982, 1983, 1985; Freeman 1980). In the 1980-ties the composite pulses were used mostly in high-resolution NMR (Levitt, 1979; Freeman, 1980). Most composite pulses was developed based on computer simulations of spins behaviour in the presence of the rf pulses (e.g. Levitt, 1982).

So far, no perfect selective rf pulse suitable for multi-echo spin-echo pulse sequence has been designed, however there were many attempts to reduce spurious signals due to rf pulses and field imperfections. For example, Levitt and Ernst (Levitt, 1981, 1983) proposed to replace the refocusing  $180^\circ$  pulse in a Carr-Purcell spin-echo experiment with a composite of three pulses:  $90_x-180_y-90_x$ , where x,y denote the phase of the rf pulses. The authors showed, using an analysis of rotation operators, that this pulse compensates the effects of pulse length errors caused by inhomogeneity of the rf field and it corresponds to a “perfect”  $180^\circ$  pulse. The most commonly used variation of this pulse, known as the Levitt-Freeman pulse, is the pulse  $90_0-180_{90}-90_0$ .

Further improvement in this type of the composite pulses was proposed 10 years later by Poon et al (Poon, 1992). The authors proposed a new  $180^\circ$  refocusing pulses comprising the following pulses:  $55_{230}49_{285}93_{334}96_{114}138_{103}237_{352}133_{213}32_{187}122_{162}46_{198}122_{233}24_{88}66_{49}66_{23}57_{269}42_{22}$  that were referred as the *Version S pulse* (Poon, 1992). The report analysed in details impact of spoiling gradients,  $B_1$  and  $B_0$  inhomogeneities on the measurement of the  $T_2$  relaxation times for the Version S pulse. Fig 1.13 shows the results of  $T_2$  measurements using the Version S,  $90_0180_{90}90_0$ , sine-modulated slice selective, and standard rectangular pulses in the presence of rf and  $B_0$  variations. As seen, the Version S is the least sensitive to the  $B_1$  fields variations hence the most suitable for  $T_2$  measurements with a surface rf coil.

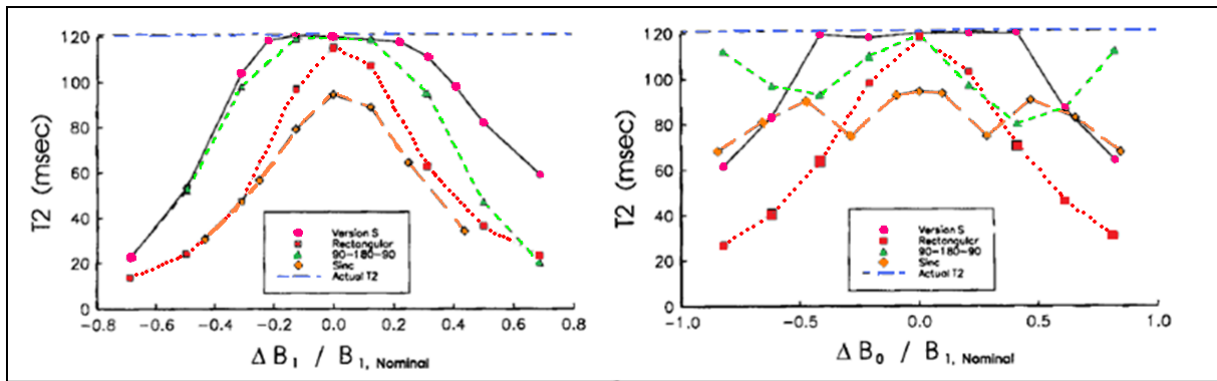


**Fig. 1.13** Experimental comparison of the Version S,  $90_0180_9090_0$ , sine-modulated slice selective, and standard rectangular pulses for  $T_2$  measurement in  $B_1$  and  $B_0$  field inhomogeneities (left and right respectively) (Poon 1992, with permission).

While the shape and the composition of the rf pulses are important factors in proper quantification measurements, slice selection is also an important factor in quantification MR imaging experiments. Mao et al. (Mao, 1988) analyzed the relationship between slice edge and slice thickness. They showed that there is a minimum ratio of the width of a slice edge to the thickness of the selected slice at a certain slice thickness. Therefore, both the desired slice profile and the corresponding rf pulse must be optimized. The authors showed, that to obtain a slice with a sharper edge at a certain pulse length, an optimal selective pulse with a higher peak amplitude is required (Fig 1.14).

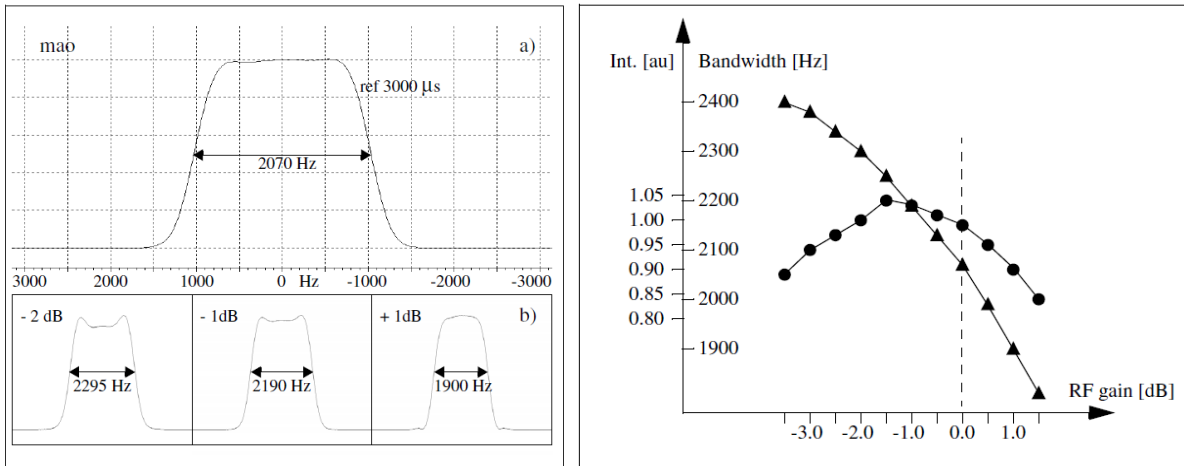


**Fig. 1.14** The spectra of the Mao pulse (left). Dependence of the pulse bandwidth (BW) on its amplitude is shown (right). Triangles – BW, circles – profiles (Bruker Manual, Paravision ver 5.1)

Finally, when the optimal parameters of the pulse sequence are selected, such as the “Version S” rf pulse and spin echo based pulse sequence (Fig.1.8), major structures of the human body can be associated with  $T_2$  relaxation times as shown in Fig 1.15.

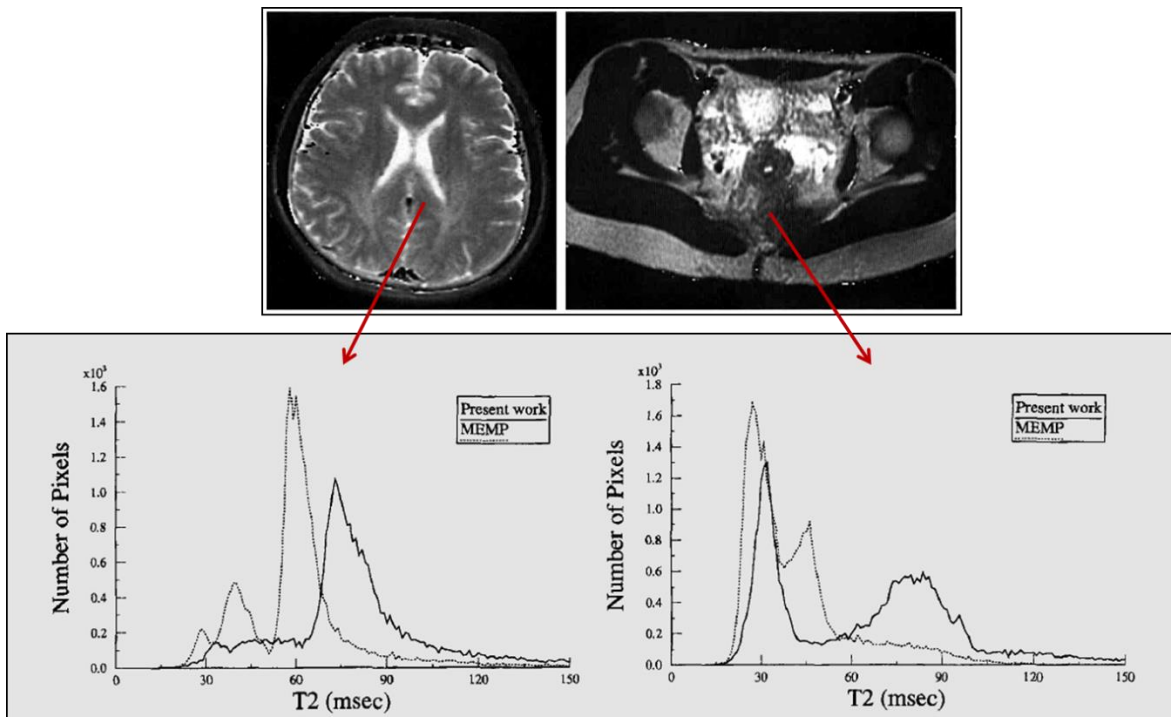


**Fig. 1.15** Comparison of  $T_2$  histograms for the brain and the pelvis region MRI using the Version S composite rf pulses (marked as “present work”) and the pulse sequence shown in Fig 1.8 (Poon 1992, with permission).

## 1.7 Identification of small brain structures in MRI

There are three major water compartments in the brain that can be relatively easily identified in MRI due to different  $T_2$  relaxation times: white matter (WM), gray matter (GM) (extra and intracellular water (IC/EC)) and cerebrospinal fluid (CSF) (Figs 1.16 – 1.17).

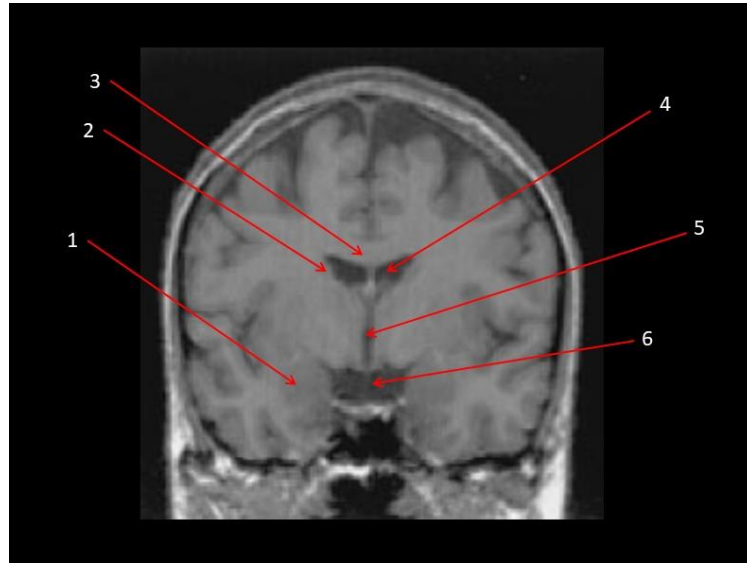


**Fig. 1.16** The three major water compartments in the brain: WM, GM, CSF. 1. Hippocampus (GM); 2. Caudate nucleus (GM); 3. Corpus callosum (WM); 4. Lateral ventricle (CSF); 5. Third ventricle (CSF); 6. Interpeduncular cistern (CSF). (modified based on Schnack, 2001; with permission)

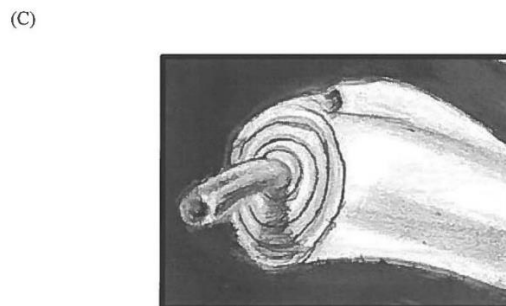
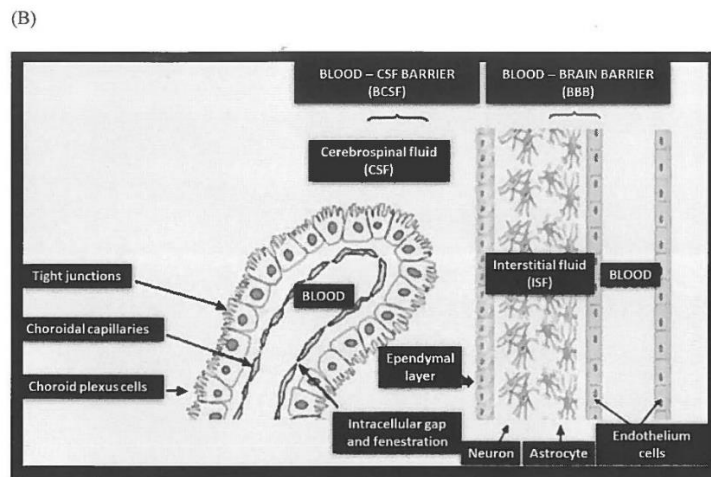
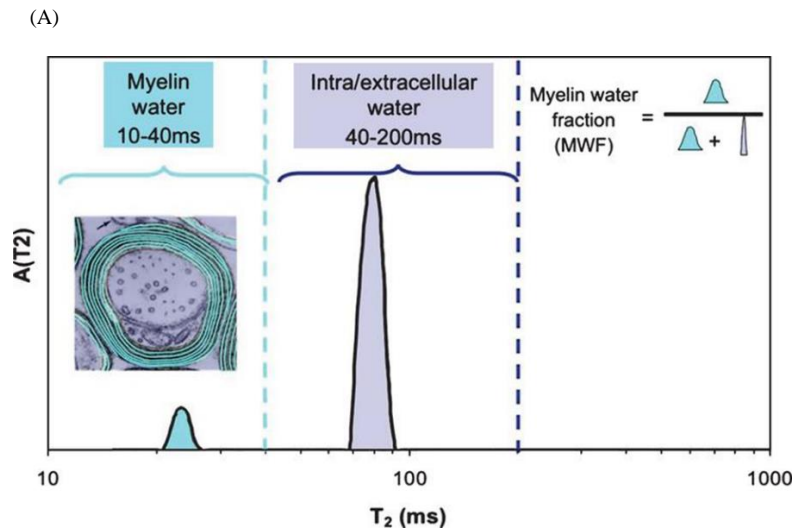


**Fig. 1.17** (A) Two different  $T_2$  values corresponding to two water compartments: myelin water and GM (extra and intracellular water (IC/EC)) obtained from the brain at 9.4T. Their calculated  $T_2$  values were  $\sim 20$ ms and 70-90 ms respectively. Location of myelin water and intra/extracellular water *in vivo* shown in (B). (C) shows anatomy of myelin. (A - MacKay, 2016, open access; B, C – drawings by the author based on free access [https://www.researchgate.net/figure/Overview-of-the-blood-brain-barrier-and-blood-cerebrospinal-fluid-barrier\\_fig1\\_262693056](https://www.researchgate.net/figure/Overview-of-the-blood-brain-barrier-and-blood-cerebrospinal-fluid-barrier_fig1_262693056))

Many neurodegenerative diseases are associated with changes only in tissues with short  $T_2$  and  $T_1$  relaxation times such as myelin (Wilhelm, 2012). In contrary to relatively simple measurements of WM, GM and CSF, high resolution and fast MRI of tissues with short  $T_1$  and  $T_2$  is challenging, particularly using conventional MRI techniques (Larson, 2006). Degeneration of myelin is associated with various neurological disorders, including multiple sclerosis (MS). WM is composed of millions of axons covered by myelin sheath. The name “white” matter comes from the white color of myelin (electrical insulation) that coats axons (see more in chapter 2). As  $T_2$  and  $T_1$  relaxation times depend on myelin content, MRI could be potentially used for detection of myelin degeneration due to MS or other neurological disease (Wilhelm, 2012; Piredda, 2020; Larson, 2006, Piędzia, 2014).

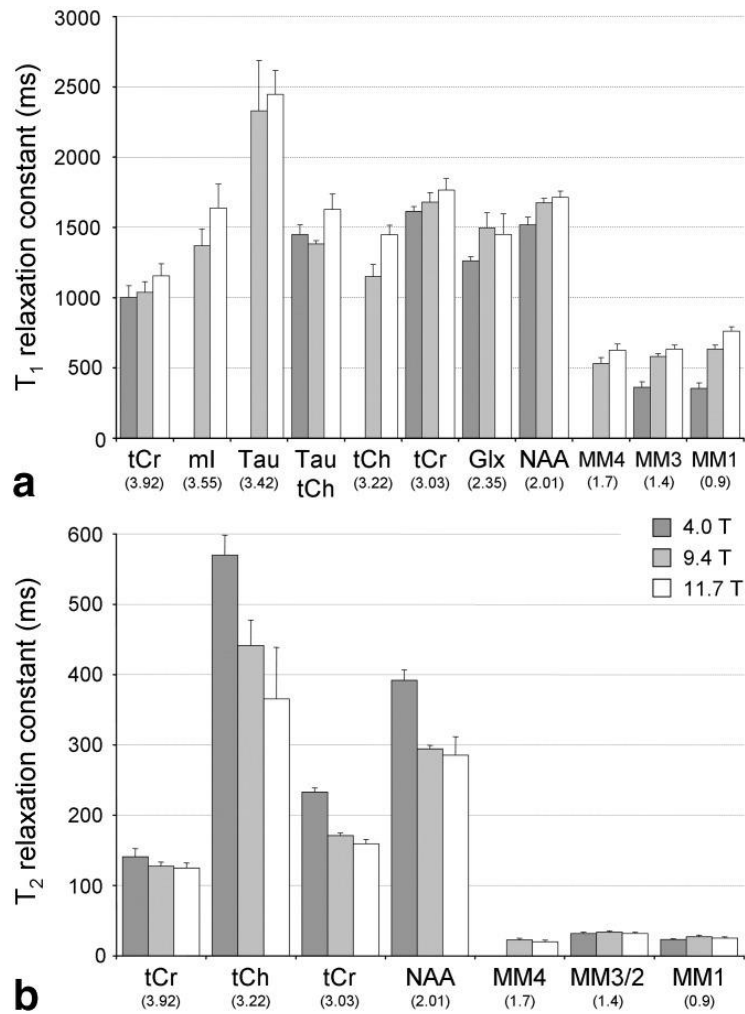
Previous MRI studies (de Graaf, 2006) allowed identification of various brain structures based on  $T_2$  relaxation times (Figs 1.17, 1.18), despite very short  $T_2$  and low water content (Fig. 1.19) implying very low signal and fast signal decay. As seen in Fig 1.17 - 1.19 the following structures can be identified based on differences in  $T_2$  relaxation times: corpus callosum, cerebral cortex, olfactory bulb, hippocampus, cerebellar white matter, cerebellar gray matter, stratum, thalamus and mid-brain.

Table 1  
Water  $T_1$  and  $T_2$  Relaxation Time Constants for Rat Brain at 4.0, 9.4, and 11.7 T

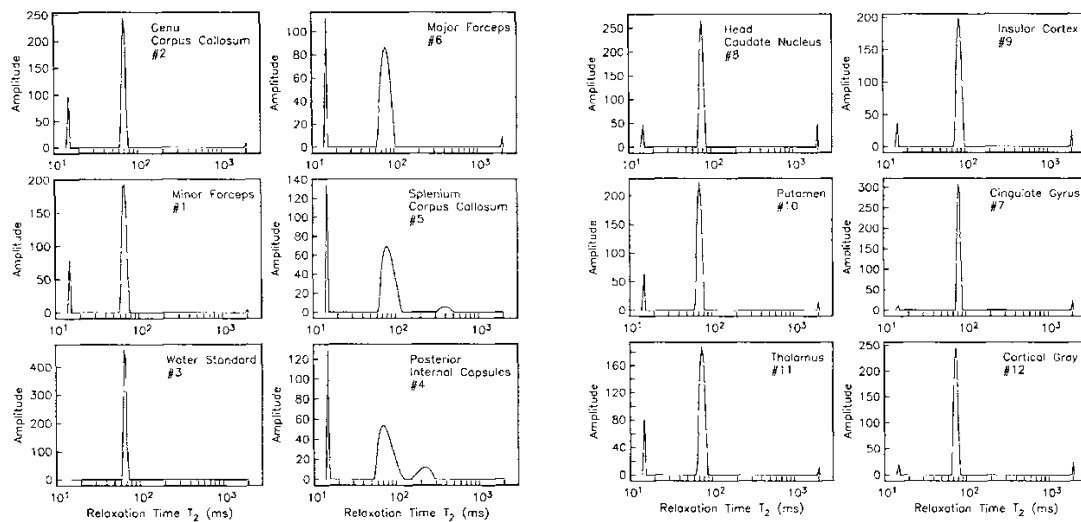
	Structure								
	cc	cx	ob	hc	cw	cg	st	th	mb
4.0 T									
$T_1$ (ms)	1096.8	1285.8	1640.6	1334.1	1046.9	1352.6	1288.2	1169.4	1064.4
SD (ms)	49.3	77.0	20.8	97.4	53.3	82.6	87.3	69.5	17.3
9.4 T									
$T_1$ (ms)	1752.1	1948.4	2129.1	2059.7	1660.3	2097.2	1927.0	1793.1	1786.5
SD (ms)	52.1	51.9	63.7	66.1	79.3	68.2	54.7	64.3	81.9
11.7 T									
$T_1$ (ms)	1861.3	2073.4	2304.3	2222.8	1745.1	2109.4	2046.5	1903.2	1893.2
SD (ms)	73.5	100.7	63.4	63.2	36.0	95.0	55.3	61.2	44.3
4.0 T									
$T_2$ (ms)	57.9	65.2	80.2	72.0	58.8	65.3	69.7	61.7	60.6
SD (ms)	1.6	2.4	2.0	1.3	1.5	2.0	2.0	2.1	1.9
9.4 T									
$T_2$ (ms)	35.8	42.1	48.1	45.4	37.2	41.7	43.5	40.6	40.3
SD (ms)	1.2	1.2	1.9	1.8	2.0	1.6	2.4	1.2	1.4
11.7 T									
$T_2$ (ms)	30.7	36.2	38.9	38.9	27.1	37.3	36.4	33.8	33.8
SD (ms)	1.0	1.0	1.1	1.3	1.3	2.3	2.2	1.6	1.9

cc = corpus callosum, cx = cerebral cortex, ob = olfactory bulb, hc = hippocampus, cw = cerebellar white matter, cg = cerebellar gray matter, st = striatum, th = thalamus, mb = mid-brain.

**Fig. 1.18**  $T_1$  and  $T_2$  relaxation times of different brain structures in the rat at various magnetic fields (de Graaf, 2006 with permission).

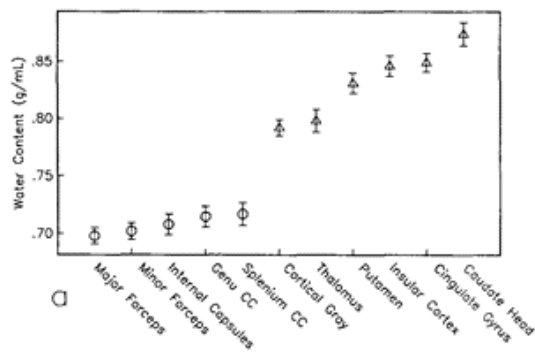


**Fig 1.19** Metabolite and macromolecule longitudinal  $T_1$  relaxation and (b) transverse  $T_2$  relaxation in rat brain in vivo at 4.0T, 9.4T, and 11.7T. Metabolite  $T_1$  and  $T_2$  relaxation times were obtained at  $TE \geq 100$  ms to avoid contamination from macromolecular resonances. Myo-inositol, taurine, and MM4 could not be reliably determined at 4.0T with simple integration. Error bars represent the SD over five animals (de Graaf, 2006 with permission)

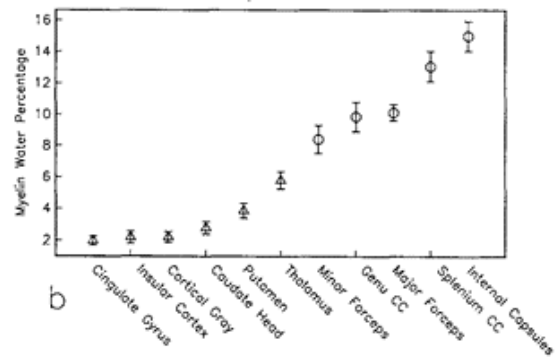


(A)

(B)



(C)



(D)

**Fig. 1.20** (A)  $T_2$  distributions for the water standard and the five white matter locations in the brain of one volunteer at 1.5 T. (B)  $T_2$  distributions for the six gray-matter locations in the brain of one volunteer. (C) Mean water content in g/ml for the 11 structures examined. Circles and triangles correspond to white and gray matter, respectively. (D) Mean myelin water percentage for the 11 structures. Circles and triangles correspond to white and gray matter, respectively. (Whittall, 1997 with permission).

In addition, the dependence of relaxation times of the brain structures on the magnetic field strength makes animal experiments at 9.4T even more demanding when compared to the lower fields (Fig 1.19). The differences are smaller at 9.4T than at the lower field causing further decrease of the CNR between brain structures. Due to various brain components with

very short  $T_2$ , the precise  $T_2$  measurements are crucial for detection of myelin in the brain. Despite these challenges, some authors (e.g. Wilhelm 2005, Filipii, 2021) state that MRI of myelin has the potential to characterize its loss and reveal axonal integrity and function, hence provide information on early neurodegenerative development.

## 2. Multiple sclerosis (MS)

### 2.1. Etiology and diagnostic methods of MS

Multiple sclerosis (MS) is associated with demyelination in the brain and spinal cord (McGinley, 2021). Myelin is an insulating structure surrounding axons fibers. It increases electrical conduction velocity along the nerve cells. Damaged myelin causes interruptions of electrical communication between cells that impact higher brain functions causing neurological symptoms. Myelin is a lipid–protein bilayer that extends from the outer membrane of glial cells (i.e., oligodendrocytes in the CNS) and winds around individual axonal fibers. These deficiencies in oligodendrocyte function may lead to axonal degeneration causing in turn neurodegenerative disorders, such as multiple sclerosis or schizophrenia (van der Knaap, 2005; McGinley, 2021). Therefore, assessment of myelin may reveal abnormalities of the CNS (Wilhelm, 2012).

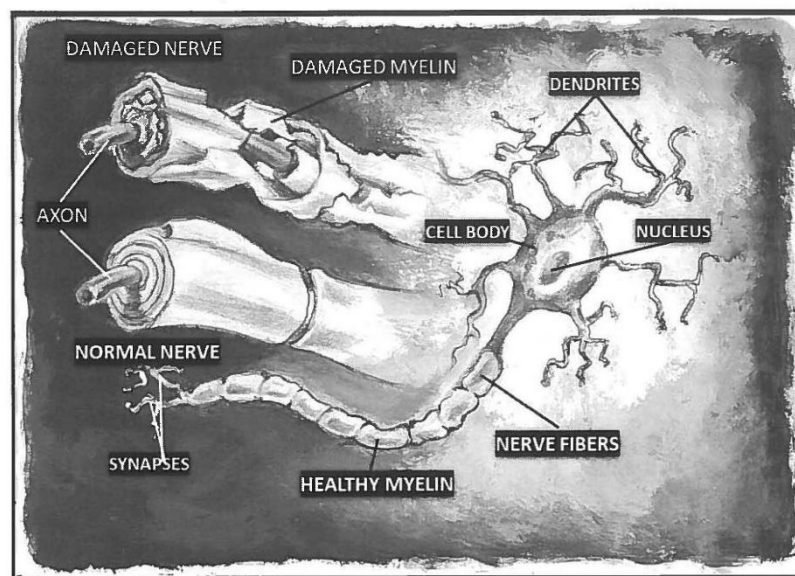


**Fig. 2.1** Morphology of a normal and damaged axon: myelinating Schwann cells support neurons, that wrap around axons to form the myelin sheath, a lipoprotein layer surrounding the axon. (Author’s drawing based on [https://www.medicinenet.com/image-collection/nerve\\_fibers\\_and\\_myelin\\_attack\\_in\\_ms\\_picture/picture.htm](https://www.medicinenet.com/image-collection/nerve_fibers_and_myelin_attack_in_ms_picture/picture.htm))

As shown in Fig. 2.1 myelin is a lipoprotein layer surrounding an axon and is important in transferring reflexes. Therefore, its loss or alteration is associated with neurodegenerative diseases such as MS, that is associated with chronic inflammation of CNS.

The processes associated with MS include lymphocyte and macrophages infiltration, and local demyelination (Fig. 2.2).

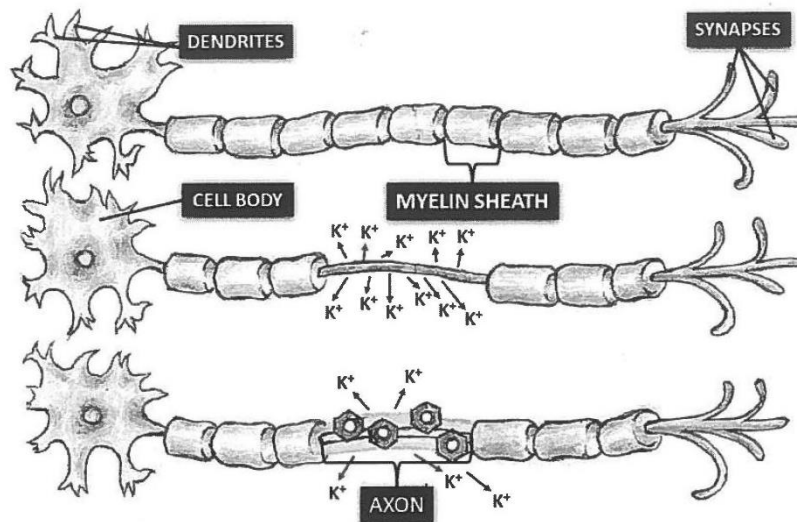


**Fig. 2.2** The processes involved in the demyelination due to MS include partial injury, damaged or total removal of myelin. (Author’s drawing based on <https://pl.pinterest.com/pin/362328732501544415/>)

There are 2 major types of MS. About 85-90 % of MS cases are relapsing-remitting (RRMS) while 10-15% are primary progressive MS (PPMS) (Lublin, 1996; McGinley, 2021). Relapsing-remitting MS is a type of MS when relapses (symptoms getting worse) are followed by recovery (“remitting”). In other words, symptoms do not get worse between relapses but after each relapse they can be worse than before. Frequently, after 10-15 years, RRMS develops into a secondary progressive form of MS (SPMS), characterised by progressive loss of neurological functions, that resembles PPMS (Confavreux, 2005). RRMS is characterised by periods of acute relapses of focal inflammation in the brain or spinal cord WM with neuronal demyelination and axonal loss. Neuronal lesions can provide no symptoms hence their clinical detection may be problematic. They are various symptoms of MS including limb paresis, impaired or double vision, vertigo (causing loss of balance and difficulties of performing daily tasks), bladder symptoms, cognitive impairment or fatigue. The acute MS attack generally diminishes within a few weeks or months, but it leaves various residual symptoms. The average relapse-rate in untreated RRMS patients is approximately 0.5

per year (Confravreux, 2005) while recovery time varies. In the early stages of MS, recovery is rather significant, most likely due to the plasticity of the brain. In the later stages of MS, recovery is often incomplete due to the progressive myelin loss (Chard, 2021; Cooke, 2006).

## **2.2 Immunology and pathophysiology of MS**

The cause of MS is unknown. However epidemiological and genetic studies showed both environmental factors and genetic predispositions may trigger inflammation leading to MS. For example, MS development was associated with Epstein–Barr virus, sunshine (UV), smoking, obesity and vitamin D (Ascherio, 2013; Vandeborgh, 2021). Interestingly, migration is a secondary factor to an environmental exposure (Kurtzke, 2013).

The histopathology of MS shows CNS inflammation, mostly located in white matter around a central blood vessel. Macrophages and T-lymphocytes (T cells) are the major component of the inflammatory cells, although B-lymphocytes and plasma cells are also present (Kutzelnigg, 2005; Lucchinetti, 2000). Animal models of MS indicate, that inflammation is an autoimmune reaction directed against CNS antigens, mostly myelin components (McGinley, 2021; Modin, 2004; Oksenberg, 2004). Circulating myelin-reactive T cells are common in healthy individuals and MS patients, but are more active in the cells of MS patients (Zhang, 1994; Lovett-Racke, 1998; Bielekova, 2004). There are few models that attempt to explain how the myelin-reactive T cells become activated in MS patients (He, 2002; Banerjee, 2005; Fujinami, 2006). For example, the molecular mimicry model associates activation of T-cells with viral infection (Wucherpfennig, 2001). The super-antigens model postulates, that some viral or bacterial antigens are capable of cross-linking the major histocompatibility complex (MHC) class II molecule on the Antigen Presenting Cells (APCs) with the T cell receptor complex, resulting in polyclonal T cell activation (Wucherpfennig, 2001). However, none of these models has been proven responsible for the pathogenesis of MS.

The most common model of MS (Fig 2.3) assumes that the inflammation is preceded by systemic activation of myelin-reactive T helper (Th), that involves APC (antigen presenting cells) that recognize T lymphocytes. These cells migrate into the CNS, that is an area unreachable to immune cells. In the CNS the Th cells are reactivated by their antigen produced in perivascular cells. This secondary activation causes the release of proinflammatory cytokines, chemokines, and other mediators, that in turn attract and activate

other immune effector cells (CD8+ T cells, B cells, and microglia/macrophages). Finally, these cells initiate the inflammatory lesion and cause demyelination and hence axonal damage mostly through cytotoxicity (Hemmer, 2002; Holmes 2005).

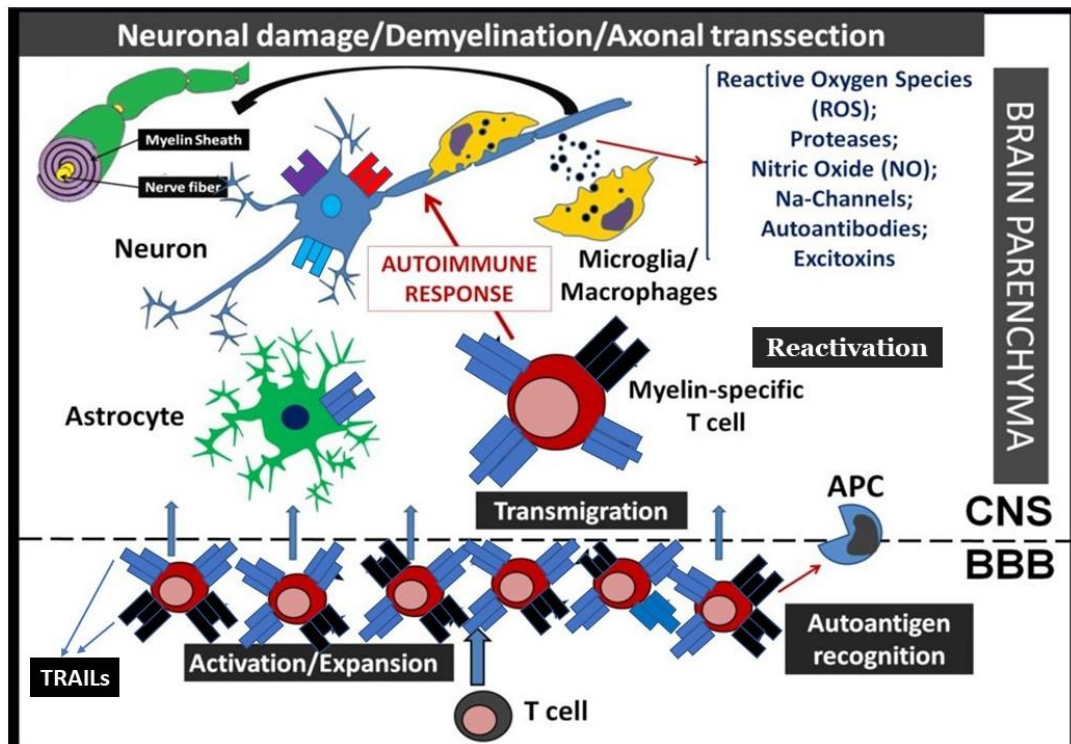


**Fig. 2.3** Simplified biomolecular model of MS. Immunological processes causing inflammation target myelin sheath, initiating demyelination. This eventually leads to axonal loss, dysregulation of ion channels and in consequence resulting in death of oligodendrocytes and neurons. The TRAIL ligand (tumor necrosis factor (TNF)-related apoptosis-inducing ligand) appears to be responsible for apoptosis of cells not related to tumor development, e.g. CNS cells. The first step in the MS related inflammatory plaque formation is the activation of T cells, which no longer undergo normal immunoregulatory mechanisms. The following steps include expansion of T cells and their transmigration through Blood Brain Barrier (BBB). Once T cells autoantigens are recognized, they are reactivated inside the CNS. Myelin sheath lesions and neuronal death may then occur due to TRAIL receptors presented by cells targeted to undergo apoptosis, which is an antigen-independent process that appears through TRAIL system. It has been shown that astrocytes remain ‘immune’ to the TRAIL apoptosis mechanism, in contrary to other cells that are part of the inflammatory autoimmune response. (Author’s drawing based on Aktas, 2007, open access).

## 2.3 Treatment of MS and myelin detection methods

Although some treatment for MS exist, currently there is no effective cure for this neurodegenerative disease. Among various drugs, a corticosteroid, methylprednisolone and interferon have been used for treatment of MS. In particular, methylprednisolone was used for treatment of acute relapses in MS. Interferon (IFN)- $\beta$  targeting the immune system, became the first disease-modifying treatment for MS, reducing the overall relapse-rate by approximately one-third (Jackobs, 1996). Although the exact mechanism of action of IFN- $\beta$  is not known (Zhang, 2002, 1994; Hartung, 2004), MRI studies using contrast-enhancing lesions of the central nervous system (CNS) showed that IFN- $\beta$  treatment also reduces disease activity. Following this research, other drugs have been introduced, such as glatiramer acetate, intravenous immunoglobulins, and mitoxantrone (Hartung, 2004)

Currently the most common method of studying myelin is histological staining (Laule, 2006). Myelin structure has been also investigated with X-ray diffraction (Avila, 2006) and Raman optical techniques (Wang, 2005; Fu, 2008). These techniques are however destructive thus limited to animal studies. Recently, myelin-specific contrast agents for MRI and positron-emission tomography (PET) that selectively bind to myelin have been developed (Frullano, 2011; Wei, 2020), but their toxicity may prevent clinical applications.

So far, MRI is the only technique allowing non-destructive and non-toxic myelin assessment capabilities in both animals and humans based on endogenous protons and hence not requiring any agent injections. The most common MR techniques applicable to studies *in vivo* that have demonstrated histologically correlated sensitivity to myelin are magnetization transfer (MT) and  $T_1$  and  $T_2$  relaxometry (Dousset, 1992; MacKay, 1994). The  $T_2$  values ranging from 10 to 50 ms have been assigned to restricted myelin water (MacKay, 1994) and showed correlation with myelin-specific histological staining (Laule, 2008).

## 2.4 Application of MRI to diagnosis of MS

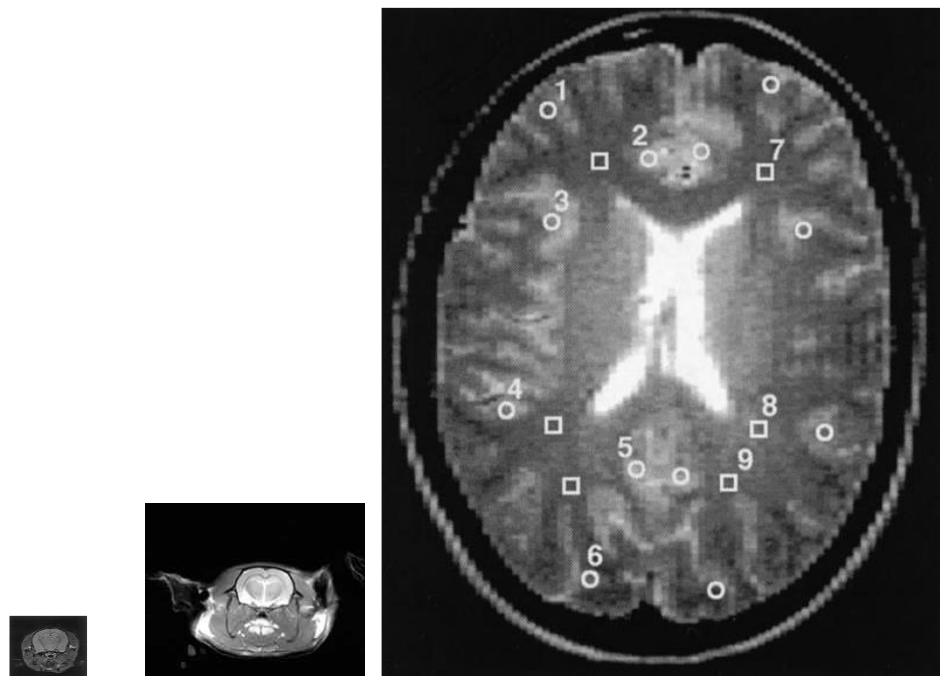
Many neurodegenerative diseases including multiple sclerosis (MS), Alzheimer's disease (AD) and Parkinson's disease (PD) are associated with changes in the relaxation times of diseased tissues. Specifically, MS has been associated with small changes of  $T_2$  relaxation time within water fractions related to myelin in animal models and humans (Fu, 1998; Laule, 2004, 2006; Gareau, 2002; Bartzokis, 2003, 2004; MacKay, 1994; Whittall, 1997; Lancaster, 2003; Grenier, 2002; Neema, 2007).

However, when designing studies of MS, substantial differences between animal models and humans must be considered, including weight, size, respiration rate and heart beat rate (Fig. 2.4). The most important variations in MRI research are large differences in relaxation times of brain tissues within species as well as differences due to the magnetic field. While human MRI is usually performed at 3T, animal studies are carried out at 7T or higher fields to increase resolution hence to improve visualisation of small structures. For example, as seen from Fig 2.4C  $T_1$  and  $T_2$  of gray matter (GM) and white matter (WM) change almost two-fold between 4.0T and 11.7T in a rat brain. Furthermore, the differences in  $T_1$  and  $T_2$  for both WM and GM become smaller with the increasing magnetic field. To make research even more complex the reported  $T_1$  and  $T_2$  values vary significantly (10 to 50%) as stated by Weijden (2021) depending on the imaging method, selection of the region of interest and data analysis. Therefore, quantification of the data and translation between different fields is even more complex.

A) Characteristic parameters of a mouse, rat and human

	Average weight [kg]	Ave brain weight [g]	Heart rate [1/min]	Resp [1/min]	Temp [°C]
Man	62	1300	70	17	36.6
Rat	0.4	2	330-480	85	35.9-37.5
Mouse	0.025-0.035	0.4	310-840	80-220	36.5-38.0

B) MRI images of the brain of a mouse, rat and human (image size selected for comparison purposes)



Brain MRI: mouse (7T)    rat (9.4T)                      human (3T)

C) Relaxation times at selected fields for mouse, rat and human brain.

Rat (based on Fig.1.18):

Field [T]	T1 [ms]		T2 [ms]	
	WM (cc)	GM (th)	WM (cc)	GM (th)
4.0	1097	1169	58	62
9.4	1752	1793	36	41
11.7	1861	1903	31	34

Human (Wansapura, 1999):

Field [T]	T1 [ms]		T2 [ms]	
	WM (cc)	GM (th)	WM (cc)	GM (th)
3.0	832	1331	79.6	110

Mouse (Guilfoyle, 2003):

Field [T]	T1 [ms]		T2 [ms]	
	WM (cc)	GM (cortex)	WM (cc)	GM (cortex)
7.0	146	1588	35	38

**Fig. 2.4.** Comparison of the mouse, rat and human brain anatomy and MR parameters:

(A) Characteristic of the species (<https://web.jhu.edu/animalcare/procedures/>).

(B) Examples of MRI images of the mouse, rat and human brain.

Mouse (Guilfoyle, 2003): Spin-echo, TE=15ms, in-plane resolution 200  $\mu\text{m}$  x 200  $\mu\text{m}$  and slice 0.2 mm, field 7.0T;

Rat (Kirsch, 2010): Spin-echo, TR/TE= 2000/13, FOV 64  $\times$  64 mm, matrix 256  $\times$  256, slice 3 mm;

Human (3T) (Wansapura, 1999): T<sub>2</sub>-weighted MRI, 3mm transverse slice through the level of the basal ganglia in a healthy volunteer. ROIs are indicated by the squares (WM) and circles (GM). Numbers correspond to: 1 - frontal gray matter; 2 - parasagittal frontal gray matter; 3 - insular gray matter; 4 - parietal gray matter; 5 - parasagittal occipital gray matter; 6 - gray matter; 7 - frontal white matter; 8 - parietal white matter; 9 - occipital white matter.

(C) T<sub>1</sub> and T<sub>2</sub> relaxation times of selected WM and GM brain structures at different fields for mouse, rat and human.

Note: 1) strong dependence of T<sub>1</sub> and T<sub>2</sub> of WM and GM on the magnetic field, 2) the small differences in T<sub>1</sub> and T<sub>2</sub> at 9.4T; 3) major differences in size, weight and heart beat rate among species. (Standard deviations were omitted for clarity.)

(Published with permission from: Wansapura, 1999; Guilfoyle, 2003 Kirsch. 2010.)

As myelin water  $T_2$  is very short (order of 10 ms at 9.4T) (McCreary, 2009) the detection of changes due to disease is challenging and requires application and optimization of both pulse sequence and rf coil design to obtain maximum SNR, enabling detection of miniscule changes in  $T_2$  (Kozlowski, 2008). The pathological processes associated with MS, Alzheimer's or Parkinson's Diseases have been attributed to the distribution of iron and myelin in brain white matter (Bagnato, 2011; Dobson, 2019; Frisoni, 2010; Watanabe, 2012; Baudrexel, 2010; Du, 2011). Changes in the content of water bound to the myelin lipoprotein bilayers, due to the appearing myelin sheath plaques as well as increase of the iron content cause decrease in the  $T_1$  and  $T_2$  relaxation times were also reported (Rahmanzadeh, 2021; Neema, 2007). Therefore, it was postulated that measurements of relaxation time changes in the brain may allow *in vivo* diagnosis of various neurological diseases (Wilhelm, 2012).

White matter is formed predominantly by axons surrounded by the myelin sheaths, which dramatically shortens the relaxation time of adjacent water. Gray matter has usually significantly smaller amount of myelin as it consists of neuronal cells, neuropil (dendrites and unmyelinated axons), glial cells and capillaries, thus has longer  $T_2$  (Barkovich, 2000; Mottershead, 2003; Koenig, 1990; Does, 2002). Myelin which has very short  $T_2$ , although potentially important as a marker for pathologies, is normally invisible in conventional MRI due to relatively long echo time (TE) when compared to  $T_2$  used in clinical imaging. To deal with this shortfall Poon et al. attempted to collect data with short TE and selective rf pulses using the multi-echo pulse sequence (Poon, 1992) aiming to obtain information on distribution and changes of short  $T_2$  water components within the brain. The effectiveness of this approach has been limited, mostly due to long selective pulses required for slice selection, disabling short enough TE, causing imperfections in the slice selection, and generating unwanted stimulated echoes and in consequence further MR images degradation (MacKay, 1994; Whittall, 1997). As  $T_2$  decreases with the raising magnetic field strength, measurements of the signal from myelin water components are even more demanding at the high fields that are typically used in preclinical studies (de Graaf, 2003; van de Ven, 2007; Kara, 2012). This issue is especially important in mouse MRI studies, where the small size of the brain requires high resolution imaging, hence very strong magnetic fields (usually 9.4T or higher). An alternative for the assessment of very short  $T_2$  components is to use a 2D ultra-short echo time (2D UTE) pulse sequence (Du, 2001, 2012; Gatehouse, 2004). However, in this case very short echo time leads to proton density rather than  $T_2$  weighted MRI.

Although the majority of water within the brain has a  $T_1$  of the order of 1–2 s, depending on its location and field strength (Guilfoyle, 2003; Bjarnason, 2005; van de Ven, 2007; Deoni, 2008; Kara, 2012), several authors have indicated the presence of a shorter  $T_1$  component in myelinated regions of the brain (Lancaster, 2003; Herndon, 1996; Labadie, 2014) and spinal cord (Wilhelm, 2012). This revelation brings opportunity to utilize  $T_1$  contrast or combine both  $T_1$  and  $T_2$  contrasts in the areas of very short  $T_2$ . Therefore, to achieve maximum myelin contrast in our study we applied a non-selective inversion recovery (IR) pulse before UTE (IR-UTE) (Du, 2012; Larson, 2007) allowing further enhancement of the contrast in the brain regions with short  $T_2$  and  $T_1$ . Considering the small amount of tissue with short  $T_2$ , a strong MR signal is essential to provide sufficient SNR for quantification measurements. To fulfill this requirement, we compared several radio-frequency (rf) coil configurations. While volume coils provide good rf field homogeneity, surface coils deliver higher SNR, but only close the body surface as their rf field drops significantly with the distance from the coil. As SNR can be increased by the application of rf coils with low resistivity, because reduced resistance of the coil reduces electronic noise (Ratering, 2008; Baltes, 2009), to further increase SNR, the cryo-probe was used in the presented research.

## 3. Experimental Section

The application of animal models that simulate as close as possible human disease in the terms of physiology and response to therapy is a necessity for bench-to-bedside translation of research. Much of the research in human diseases relies on animal models and various animal models are well known and are frequently used. Due to low costs, size and handling the most often used are mouse models. These models allow to study *in vivo* brain function and animal behaviour to better understand molecular interactions, pathways and functional mechanisms. Furthermore, the small size of a mouse allows the MRI study in magnets generating very strong magnetic field within small magnet bore size (~20cm), such as the available at IFJ/PAN 9.4T system.

### 3.1 Animal model of MS

There are various animal models of MS, such as experimental autoimmune encephalomyelitis (EAE), that can be induced by the active sensitization to CNS tissue, myelin or different protein antigens of the CNS or by the passive transfer of auto reactive T-cells (Madsen, 1999). Chronic virus-induced inflammation and demyelination in the CNS is an alternative model of MS (Bieber, 2004) but the Theiler's virus encephalomyelitis appears to be the most reliable and most frequently used virus-induced MS model (Kim, 2021). Despite differences in the animal models of MS, similar patterns of demyelination and remyelination suggest common basic mechanisms of tissue injury and repair (Bieber, 2004).

In our studies cuprizone was used to induce MS-like symptoms in a mouse. Cuprizone (bis-cyclohexanone oxaldihydrazone) induces reproducible demyelination mostly in mouse brain white matter structures (also in gray matter). This experimental approach has been extensively used as a rodent model of MS and to study demyelination and remyelination processes in the central nervous system (CNS) (Blakemore, 1973; Ludwin, 1978; Hiremath, 1998; Stidworthy, 2003; Komoly, 2005). In this model, the orally administered copper chelator cuprizone (bis(cyclo-hexanone)oxaldihydrazone) causes a highly reproducible demyelination of certain brain regions, including the corpus callosum (CC). The CC represents the most frequently investigated white matter tract in this model. The extent of demyelination depends on mouse strain, cuprizone dosage and animal age and is characterized by: 1) the loss of the myelin-forming cells oligodendrocytes (OLG); 2) myelin sheath

degeneration (from the third week of intoxication); and 3) recruitment of microglia and astrocytes to the lesioned area. Acute demyelination is followed by spontaneous remyelination during subsequent weeks when mice are fed normal chow. In contrast, remyelination is highly restricted after chronic demyelination. Demyelination has been evaluated based on myelin structure, biochemical parameters, myelin staining techniques and Lin- markers analysis (Teunissen, 2005). As cuprizone susceptibility depends on strain, age and weight of the animals (Irvine, 2008; Herder, 2011), different drug concentrations have been used to induce disease, although the most common is 0.2% weight mixed into a standard powdered rodent chow (Stidworthy, 2003; Kumar, 2003; Mason, 2004).

Similarities between MS lesions in people and cuprizone-induced demyelination in animals were observed with some differences, such as inflamed blood vessels and the presence of CD3 T cells (Herder, 2011). As demyelination caused by cuprizone includes processes such as spontaneous remyelination during acute demyelination, the model may distinguish acute and chronic demyelination. The model may also distinguish gender differences because animal model shows the contribution of some growth factors and cytokines during and after cuprizone intoxication (Teunissen, 2005).

As shown by Torkildsen (2008) the MR images of the cuprizone model of MS correlate well with histopathological data. The authors also showed that this model allows studies of de- and remyelination using MRI. They indicate the use of the C57BL/6 strain offers the potential for future studies on transgene and knockout mice. They also showed that MRI of the cuprizone model offers capability of MRI to follow the disease progression and monitor treatment. Wu et al demonstrated that MRI can be used as a reliable marker of the extent of pathology in this model (Wu, 2008). Torkildsen (2009) and Veto (2007) showed reduced brain lesions in T<sub>2</sub>-weighted MR images of a cuprizone model in week 5, that correlated with increased water content in brain parenchyma and less severe demyelination of CC at week 6 and 1 week after recovery.

More advanced MRI techniques, such as Magnetization Transfer MRI (MT-MRI) and Diffusion Tensor MRI (DT-MRI) have also been applied to the study of MS. MT-MRI was used for evaluation of de- and remyelination (Chen, 2007) in MS. DT-MRI was applied to assess pathology and recovery in the cuprizone model (Harsan, 2008). The losses in the myelin content in the animal model were detected using combination of *in vivo* DT-MRI and histology allowing an assessment of demyelination (Harsan, 2008). Injection of triiodothyronine (T<sub>3</sub>) hormone after 3 weeks of cuprizone withdrawal progressively restored

the normal DT-MRI corresponding to remyelination. Furthermore, DT-MRI allowed assessment of the T3 hormon as an inducer of oligodendrocyte progenitor cells in the mouse brain following demyelination.

Interestingly, MRI was also used to study spinal cord lesions as they correlate with disability in MS patients (Rovaris, 2001; Agosta, 2005; Tench, 2005). Beside differences in the development of gray and white matter lesions in MS, *in vivo* MRI studies demonstrated also that spinal cord lesions arise probably independently from brain lesions. However, underlying mechanisms resulting in region-specific disease manifestations remain undetermined (Agosta, 2007; DeLuca, 2006).

### **3.2 Selection of the MRI techniques for the study of demyelination in the animal model of MS**

Pulse sequences used for imaging of the myelin-deficient brain areas include T<sub>2</sub>-weighted MRI, such as SE and GE with short TE and ultra-short echo time (UTE) (Wilhelm, 2012; Larson 2006; Piędzia 2013; Piędzia 2014). The T<sub>1</sub> and T<sub>2</sub> contrast in these sequences can be further enhanced by the application of the magnetization inversion using the IR-UTE pulse sequence (Piędzia, 2014). These techniques allowed contrasting different brain structures associated with WM and GM in animals and in humans (Chavez, 2012; Piędzia, 2014). However, the most suitable pulse sequence for MS detection remains unknown. Therefore, we investigated feasibility of using various pulse sequences for myelin detection. The studied pulse sequences included: SE, GE, CPMG, IR-UTE and segmented magnetization prepared rapid gradient echo (MP-RAGE) (Brandt-Zawadzki, 1996; Fellner, 1996; Marques, 2010; Bock, 2013). These techniques were tested considering minimum echo time, total acquisition time, available rf coils, SNR, B<sub>1</sub> field homogeneity, spatial resolution of imaging of the mouse brain, especially imaging of cortical WM and GM with high contrast. Various rf pulses, such as standard selective and composite rf pulses, were also investigated in each pulse sequence.

In our studies, to obtain maximal SNR, we used a cryo-coil along with the selected pulse sequences. This configuration allowed optimal WM/GM contrast and capability of T<sub>1</sub> and T<sub>2</sub> quantification of the structures in the mouse brain *in vivo*, in healthy mice as well as in cuprizone mouse model of demyelination. In order to select the most reliable and robust MRI pulse sequence considering time efficacy, high resolution 3D imaging of demyelination

processes, the three imaging techniques were tested in phantoms, *ex vivo* and *in vivo* mouse brains: modified CPMG, ultra-short echo time (UTE) and MP-RAGE. As shown below in details, the MP-RAGE technique and the rf cryo-coil were selected for further studies of the cuprizone induced demyelination in the mouse model of MS, as it met most of the above listed requirements.

### **3.2.1. Application of the modified spin-echo pulse sequences for quantitative $T_2$ imaging (Piędzia, 2014).**

As the first approach to myelin imaging at 9.4T we applied two  $T_2$ -weighted imaging methods: 1) custom implemented Spin-Echo Multi-Echo (SEME) pulse sequence composed of the Carr-Purcell-Meiboom-Gill (CPMG) sequence with Levitt-Freeman rf pulse and decaying crusher gradients pattern (Poon, 1992, see chapter 1.4); 2) standard Multi-Slice Multi-Echo sequence using Mao selective refocusing pulse (Fig. 1.14). As a reference the well-established non-selective CPMG MR spectroscopic sequence composed of non-selective  $90^\circ$  and  $180^\circ$  pulses was used in order to evaluate performance of the pulse sequences and to compare  $T_2$  values of the samples with the gold standard, namely CPMG with non-selective pulses.

Phantoms with two different concentrations of  $\text{CuSO}_4$  were used to compare the measurements using the three mentioned pulse sequences. The concentrations were chosen to obtain the  $T_2$  values close to the expected values in brain tissue. To ensure relevant comparison, the same repetition time and echo time ( $TR = 10$  s,  $TE = 10$  ms) were used for each pulse sequence. The number of echoes was 64 for the imaging methods with selective pulses and 512 for the non-selective CPMG spectroscopic method. The mono-exponential fitting was used for  $T_2$  calculations in phantoms as only one component was expected while bi-exponential fitting was applied to *in vivo* data due to presence of various brain structures. The Levenberg-Marquardt algorithm implemented in Matlab was used for the data fitting.

	Mao	Levitt-Freeman	CPMG
High conc. CuSO <sub>4</sub> – short T <sub>2</sub>	17.6 ± 0.9	17.3 ± 1.0	17.8 ± 0.5
Low conc. CuSO <sub>4</sub> – long T <sub>2</sub>	76.7 ± 1.4	72.4 ± 2.0	75.8 ± 0.9
Distilled water	583 ± 2	824 ± 10	2300 ± 50

**Table 3.1.** The T<sub>2</sub> relaxation times (in ms) obtained from phantoms with two different concentrations of CuSO<sub>4</sub> using three different rf pulses: Mao, Levitt-Freeman and hard pulse with standard CPMG. The T<sub>2</sub> value of distilled water is shown for comparison.

The results (Table 3.1) showed that for both, short as well as long T<sub>2</sub> relaxation time components in CuSO<sub>4</sub> solution phantoms, simulating brain tissue, different imaging pulse sequences performed similarly providing relatively small deviation from the reference (e.g. spectroscopic CPMG). The differences in T<sub>2</sub> values were smaller than 2% for short and smaller than 5% for long components. However, the water T<sub>2</sub> was substantially shorter for both pulse sequences comparing to the reference value of 2300 ms, although pulse sequence with the Levitt-Freeman rf pulse provided closer to CPMG results. The results illustrate difficulties in proper quantification of long T<sub>2</sub> values, when using various spin echo-based imaging pulse sequences. The major reason of this discrepancy is the non-ideal profile of the rf pulses applied simultaneously with the slice gradient. Furthermore, the presence of strong pulsing gradients, required for selective rf pulses, causes additional dephasing of magnetisation and therefore faster echo train decay than in purely spectroscopic pulse sequence without presence of the magnetic field gradients and soft pulses (Hurlimann, 2000).

In addition to experiments with phantoms, *ex vivo* MRI experiments were performed using fixed mouse brains. The brains were imaged with the standard multi-slice multi-echo (MSME) pulses sequence using sinc selective rf pulses and the composite refocusing pulse (Levitt-Freeman). A volume rf coil (birdcage coil, 3.5cm diameter, 4 cm long) was used in all studies. As brain contains various structures, bi-exponential T<sub>2</sub> fitting was used. The volume rf coil was used to ensure homogeneous rf (B<sub>1</sub>) excitation, that is of particular importance when selective pulses are used as the refocusing is consistent throughout the sample providing

spatially independent relaxation values. The volume rf coil also allowed homogeneous excitation of the entire sample providing uniform imaging of the entire brain.

The results of imaging and analysis using bi-exponential fitting showed that the sequence with the composite rf refocusing pulse performs better at first few echoes than standard MSME allowing more reliable assessment of the short  $T_2$  component (Fig 3.1). However, the obtained contrast between WM (high myelin content) and GM (low myelin content) was relatively small. In addition, the application of the pulse sequence with the composite rf pulse is limited to single slice acquisition, which significantly increases the total time of experiment in case of 3-D imaging. We thus concluded these pulse sequences are not suitable for reliable myelin studies *in vivo* in practical experimental conditions.

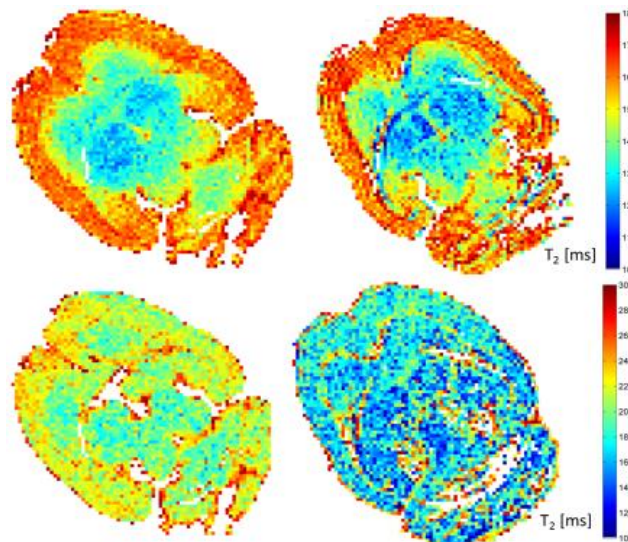


**Fig. 3.1** Maps of short (top row) and long (middle row)  $T_2$  components in the *ex vivo* mouse brain obtained using a standard multi-echo spin-echo (left column) pulse sequence and spin-echo imaging using the composite refocusing pulse (Levitt-Freeman) (right column). Color scale corresponds to  $T_2$  values in ms. Slightly better contrast for the short component is visible in the image obtained with the pulse sequence utilizing the composite Levitt-Freeman refocusing rf pulse.

### 3.2.2 Application of the Inversion Recovery UTE (IR-UTE) pulse sequence (Piędzia, 2014)

As shown above, pulse sequences based on short echo time (e.g. Ultra-short Echo Time (UTE)) allow high quality imaging of the tissues with short  $T_2$  times and  $T_2$  quantification. Unfortunately, the MR signal from these tissues is obscured by a large signal from tissues with longer  $T_2$  and  $T_1$  times originating mostly from CSF or non-myelinated gray matter compartments (Wilhelm, 2012; Larson, 2006). Therefore, we considered application of the UTE pulse sequence with an inversion pulse, called IR-prepared UTE (IR-UTE) allowing to null the long  $T_1$  component (Du, 2010) (Fig. 3.2).

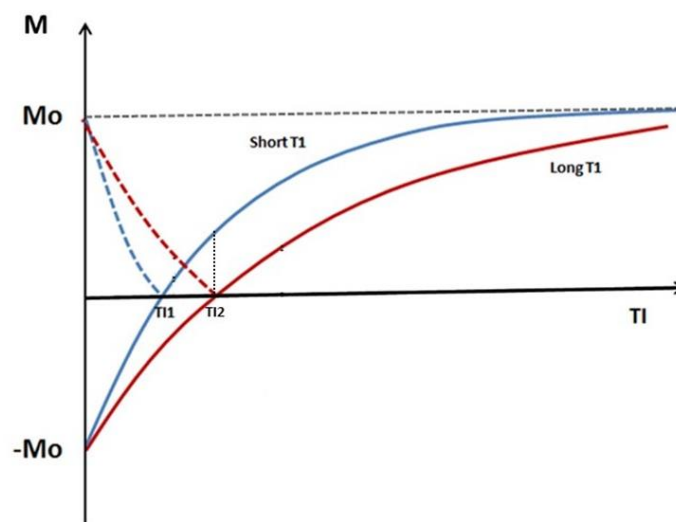


**Fig. 3.2** Application of the inversion recovery (IR) pulse to remove unwanted signal from long  $T_1$  component (non-myelin, eg CSF or non-myelinated gray matter). Magnetisation along  $z$  direction ( $M$ ) from the tissues with short  $T_1$  (blue line) and long  $T_1$  (red line) relaxation returns to equilibrium after application of the IR  $180^\circ$  pulse at time  $T1$ . The optimal time for removing signal from long  $T_1$  tissue is marked at  $T2$  when there is no signal from long  $T_1$  component while there is a signal from “blue” tissue (marked with the dotted line). The imaging pulse sequence (e.g. SE) starts at this point. Dashed line represents actual signal decay detected by the rf coil (Author’s drawings based on Haacke, 1999).

As shown in Fig. 3.2 signal from a tissue with long  $T_1$  can be nulled when proper TI is used. At this point an imaging sequence may start, for example with a  $90^\circ$  or shorter pulse depending on the technique. However, IR pulse sequence reduces SNR, as only part of the magnetization is used for imaging, therefore to obtain high resolution images, which is crucial for myelin imaging, we used the cryo-coil. This coil takes advantage of both lower resistivity at lower temperature and high sensitivity of the quadrature surface coil (Baltes, 2009). Beside increase of SNR, the quadrature reception of the coil partly compensates inhomogeneities in MR images and improves performance of selective rf pulses caused by inhomogeneous  $B_1$  field produced by a standard surface coil. The combination of optimal IR-UTE and the cryo-coil allowed to obtain sufficient image contrast of the mouse brain structures with short  $T_2$ .

Although benefits from using the cryo-coil and the inversion pulses before UTE-based sequences are already known (Baltes, 2009; Du, 2011; Guilfoyle, 2003), the combination and preclinically relevant optimization of these components *in vivo*, aiming at imaging of tissues with intrinsically short  $T_2$  is still a topic of active research. Therefore, the aim of this work was to show that the optimized pulse sequence, based on IR-UTE pulse sequence, when combined with the cryo-coil and the proper inversion pulse and time selection allows improved discrimination of short  $T_2$  regions in the mouse brain within a total experiment time suitable for *in vivo* experiments. A standard birdcage coil was used for SNR comparison (room temperature, 35 mm diameter, 40 mm length).

For the comparison of SNR for both coils the following IR UTE parameters were used for the study: repetition time (TR)/echo time (TE) = 2500/0.350 ms; field of view(FOV) = 1.5 cm  $\times$  1.5 cm; 128  $\times$  128 matrix; slice thickness of 1 mm, number of averages (NA) 1 and coronal orientation. In addition, SNR for both coils was assessed based on the manufacturer (Bruker, Germany) recommended quality assurance (QA) procedure (multi-slice, spin echo, TR/TE = 500/15 ms), with a cylindrical phantom (2 cm diameter  $\times$  2 cm length). Water in the phantom was doped with 1 g/l of  $\text{Cu}_2\text{SO}_4$  and 4.31 g/l of NaCl simulating a typical load of the mouse brain in the rf coil. The results based on QA tests showed that the maximum SNR was 11.6-fold larger for the cryo-coil.

Fig 3.3 shows a comparison of the coronal MR images of the mouse brain *in vivo* obtained using the 2D UTE pulse sequence with the quadrature birdcage coil (Fig 3.3A) and the Bruker cryo-coil (Fig 3.3B). The marked regions indicate areas of the image used for the SNR assessment. For the birdcage coil, the measured averaged brain SNR was 4700/mm<sup>3</sup>, while for the cryo-coil, the signal distribution from the brain is very inhomogeneous

(Fig. 3.3B) due to signal excitation and detection by the surface coil. Based on the signal values from the two brain regions marked in Fig 3.3 (blue circles), SNR was calculated to be within the range of 14300/mm<sup>3</sup> at the position ~7 mm from the surface of the coil (bottom of the brain) up to 55300/mm<sup>3</sup> close to the coil surface (top of the brain – within 1 mm). This corresponds to substantial, ~3- to ~12-fold, increase in SNR for the cryo-probe as compared to the birdcage coil. These results were comparable to the values obtained using the QA procedure.

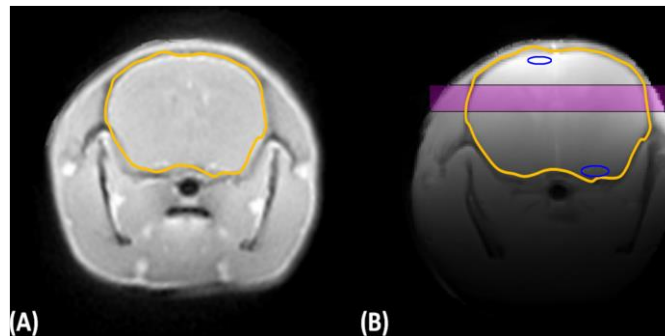


**Fig. 3.3** Coronal MR images of the mouse brain *in vivo* using the 2D UTE pulse sequence (TR respiratory triggered with a minimum of 2500 ms ; TE 0.35ms, NA – 1, in-plane resolution was 117  $\mu\text{m} \times 117 \mu\text{m}$ , 1 mm slice, FOV = 1.5  $\times$  1.5 cm) obtained with the birdcage coil (A) and the cryo-coil (B). The areas within the brain (blue solid line) were used for the assessment of SNR. The position of the horizontal violet slice was used for imaging shown in Fig. 3.5. (Permission not required for the author of the paper in Elsevier)

### 3.2.3 The method of classification of the brain structures.

An important part of the work required identification of the mouse brain structures in MR images. Classification of the brain structures was performed based on the mouse brain atlas (Anon, 1998). As a reference, schematics of the main brain structures is provided in Figure 3.4. To identify specific anatomical brain structures in MR images, SNR and CNR between different brain structures were calculated according to the formulas:

$$SNR = \frac{S_i}{Noise} \quad [Eq 27]$$

$$CNR = \frac{S_i - S_j}{Noise} \quad [Eq\ 28]$$

where  $S_i$  and  $S_j$  are signals from a region-of-interest (ROI) within the tissue  $i$  and  $j$  respectively. Noise for each coil was calculated from the images obtained without transmitting rf power (i.e. with 150 dB pulse power attenuation), while keeping other parameters the same as in the original brain image. This approach allows to avoid potential influence of signal outside of the animal that may occur due to imperfections in phase or read encoding directions. Noise was calculated as a standard deviation of Rician distribution (Gudbjartsson, 1995). SNR values were expressed per unit volume (i.e. intensity per  $1\text{ mm}^3$ ) to allow a direct comparison between images with different spatial resolutions.

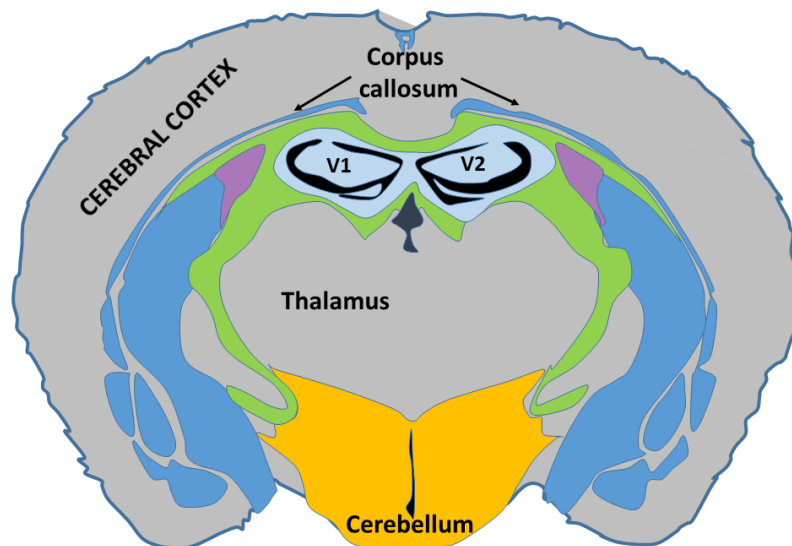


**Fig. 3.4** Schematic axial cross section of a mouse brain with labeled selected structures. V1, V2 are ventricles. (Author's drawing based on Badea, 2007)

To quantify the results, we used histograms that associate number of voxels with their intensity and hence a particular brain structure. The histograms of the horizontal images obtained for different TIs were restricted to the brain area to show overall distribution of signal intensities within the brain, while avoiding signal from other anatomical structures. This method has been frequently used for various disease diagnosis (e.g. Fujima, 2019). Histograms obtained from the brain images shown in Fig. 3.5 corresponding to different TI values are presented in Fig 3.6. They show voxel counts corresponding to the different brain

structures of WM and GM based on their signal intensity. A differentiation of WM and GM, as well as CSF and blood vessels (VS) in the brain was possible due to their different signal intensities, as shown in the histograms of the brain areas associated with different  $T_1$  and  $T_2$  values (see Fig 3.5). The procedure of assignment of the signal levels in histograms to different classes, for each TI value was as follow:

- select ROI for each structure,
- calculate signal within specified ROIs,
- compare signal from each brain structure (i.e. vessels, GM, WM, CSF) with the signal intensities in the histograms.

### **3.2.4 Identification and quantification of the brain structures in the mouse brain *in vivo* using the IR-UTE pulse sequence**

For *in vivo* studies, the IR-UTE pulse sequence with a non-selective  $180^\circ$  inversion pulse was used. To find out the maximum SNR and the optimum CNR (defined as  $(S1-S2)/\text{noise}$ , where  $S1$ ,  $S2$  are signals from tissue 1 and 2 respectively) for white and gray matter (WM/GM), a healthy C57BL/6J mouse was used. The IR-UTE pulse sequence, with a 0.5 ms long, non-selective inversion pulse was used to obtain MR images of the mouse brain at various inversion recovery times (TI), ranging from 100 to 1500 ms. For imaging, the following pulse sequence parameters were used: flip angle (FA) =  $90^\circ$ , TE = 0.350 ms, TR respiratory triggered with a minimum of 2500 ms, FOV = 1.5 cm  $\times$  1.5 cm, NA = 1 and a single slice thickness of 1 mm. The resulting in-plane resolution was 117  $\mu\text{m}$   $\times$  117  $\mu\text{m}$ . A horizontal slice (parallel to the surface coil) was collected to obtain homogeneous excitation and detection profiles with the cryo-coil. In order to ensure the proper flip angle, a reference pulse gain adjustment was performed prior to the measurements for the selected coronal slice. Total acquisition time was  $\sim$ 20 min for one slice. In addition, as a reference, a standard 2D UTE image was also collected.

SNR and CNR were calculated for various brain structures: corpus callosum (cc), fimbria hippocampi (FH), internal capsule (ic) and optic nerve layer of the superior colliculus (OP) comprising WM as well as cerebral cortex (CX), cornu ammonis (CA), dentate gyrus (DG), thalamus (Th) and peri-aqueductal gray matter (PAG) comprising GM. In addition,

signal from cerebro-spinal fluid (CSF) in left (LV) and right (RV) ventricles, the third ventricle (V3) and cerebral aqueduct (AC) was also assessed. Classification of the brain structures was performed based on mouse brain atlases (Anon, 1998; Badea, 2007).

The CNR between selected brain structures for different TI was calculated using ImageJ 1.46r (NIH, USA). The average signal intensities were evaluated for structurally different brain regions and pixel by pixel  $T_1$  relaxation times were evaluated for each brain structure using a custom written Matlab based script.

Fig. 3.5 shows an example of horizontal brain images obtained with the cryo-probe using IR-UTE pulse sequence with three different TI values: 500, 750, 1000 and no IR pulse. CNR changes are visible for different inversion times, when compared to UTE with no IR pulse ( $TI = 0$  ms), providing better contrast between the brain structures.

The  $T_1$ -map (Fig 3.7) of the horizontal slice shown in Fig. 3.5 was also calculated from the set of images obtained with various TIs using a home developed Matlab script utilizing the Marquardt's fitting routine. The map allows distinguish areas of WM and GM based on their different  $T_1$  relaxation times.

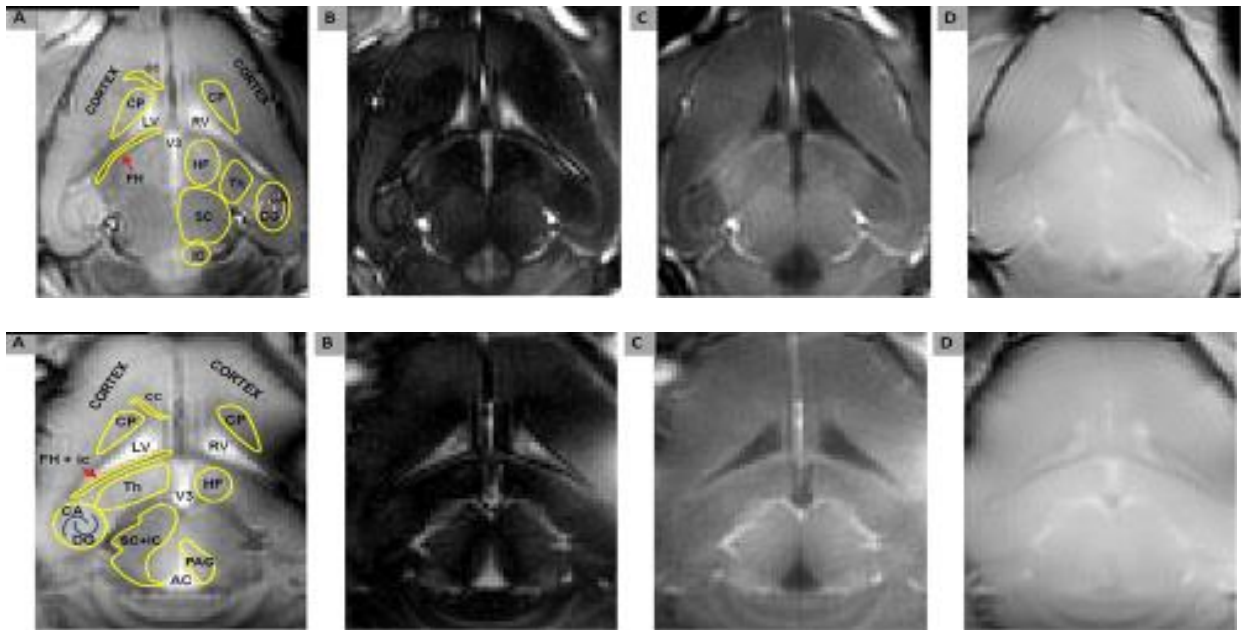


**Fig. 3.5** Horizontal IR-UTE MR images of the mouse brain *in vivo* in 2 slices (upper and lower row): (A) TI = 500 ms; (B) TI = 750 ms; (C) TI = 1000 ms; (D) TI = 0 ms (no inversion pulse). LV - left ventricle; RV - right ventricle; V3 - dorsal third ventricle; cc - corpus callosum; FH - fimbria hippocampi; ic - internal capsule; OP - optic nerve layer of the superior colliculus; CA - cornu ammonis; DG – dentate gyrus; PAG - periaqueductal gray matter; Th - thalamus; LV + RV + V3 = CSF (Piędzia, 2013; Piędzia 2014) (Permission not required for the author of the paper in Elsevier)

In the IR-UTE image obtained with TI = 750 ms, significant attenuation of the signal from most of the brain tissue (especially GM) is observed as compared to CSF, while CSF signal is diminished for TI = 1000 ms. For TI = 750 and 1000 ms, a reversal of CNR between gray and white matter is observed.

White matter comprising corpus callosum (cc) and fimbria hippocampi (FH) (including internal capsule – ic and stria terminalis – st) is clearly visible. Both structures, cc and FH, are prominent bands of WM fibers. Hippocampal formation (HF) consisting of cornu ammonis (CA) and dentate gyrus (DG), thalamus (Th) located below FH, caudo putamen (CP), located above the left and right ventricle, periaqueductal gray matter (PAG) around the cerebral aqueduct as well as the most abundant cerebral cortex (CX) were identified in MR images as GM with low myelin content. The layers of superior colliculus (SC) are also visible in the images below the hippocampal area.

The CNRs calculated for (WM/GM) and (WM/CSF) based on the images obtained with the cryo-coil using standard UTE as well as IR-UTE with inversion times 500, 750 and 1000 ms are presented in Table 3.2. The TIs were selected to optimize enhancement of CNR as compared to standard no-inversion UTE images. Signal from WM, rich in myelin, is significantly enhanced over the CSF and GM for TI = 1000 ms, with the highest positive CNR of ~20- and ~60-fold larger respectively, compared to no-inversion UTE. The largest negative WM/GM and WM/CSF contrast was observed for TI = 500 ms (~20- and ~30-fold enhancement comparing to no-inversion UTE). Contrast sign change for WM/GM contrast was observed for TI between 500 and 750 ms, while WM/CSF contrast reverses for TI between 750 and 1000 ms (Table 3.2).

TI [ms]	CNR (WM/GM)	CNR (WM/CSF)
No inversion	$-1.9 \pm 11$	$-11 \pm 8$
500	$-61 \pm 32$	$-220 \pm 38$
750	$63 \pm 17$	$-97 \pm 34$
1000	$110 \pm 38$	$230 \pm 38$

**Table. 3.2** Comparison of CNR values for WM, GM and CSF brain regions using different TI delays (Piędzia, ISMRM 2013; Piędzia, 2014) (Permission not required for the author of the paper in Elsevier)

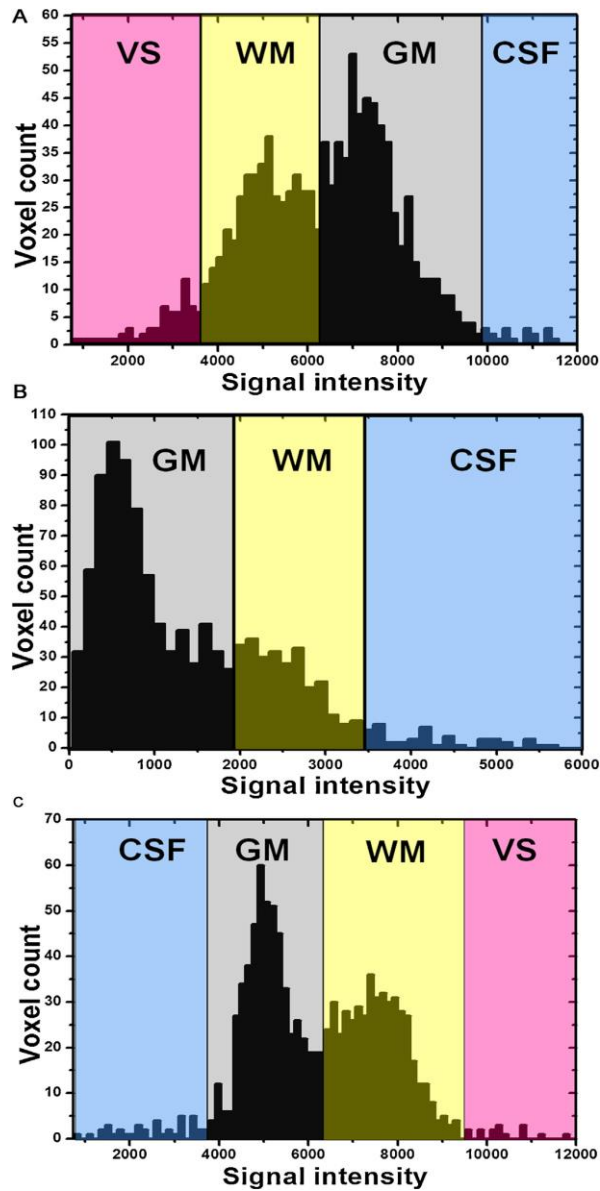


**Fig. 3.6** Histograms for different TIs, obtained from MR images in fig 3.5, showing differences between gray matter, white matter, CSF and vessels in the mouse brain: TI = 500 ms (A), TI = 750 ms (B), TI = 1000 ms (C); specific WM and GM structures are described in the text.

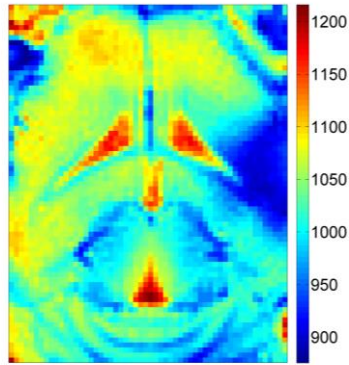


**Fig. 3.7** T<sub>1</sub>-map of the horizontal slice calculated based on the images shown in Fig. 3.5. The brain areas of WM (short T<sub>1</sub>) and GM (long T<sub>1</sub>) are clearly visible.

Brain region	T <sub>1</sub> [ms]
WM (FH)	1690 +/- 115
GM (CX)	1870 +/- 80
CSF	2220 +/- 95

**Table 3.3** T<sub>1</sub> values of different brain regions comprising white (WM) and gray matter (GM) obtained from Fig. 3.5. FH – fimbria hippocampi (including internal capsule and stria terminalis); CX – cerebral cortex; CSF – cerebrospinal fluid.

The study demonstrated benefits of using the cryo-coil when compared to other coils available in the lab (birdcage, standard room temperature surface coils) which makes it a preferable coil for contrasting different structures inside the brain of a mouse *in vivo*. Combining the IR-prepared UTE sequence with the properly selected TI time and the cryo-coil enables significant positive enhancement of the CNR from myelin rich WM regions of the mouse brain *in vivo*. The main disadvantage of the IR-UTE pulse sequence is relatively long acquisition time when high resolution 3D imaging is necessary.

Although a thinner than 1 mm slice is possible with most 9.4T systems, we found that a 1 mm slice provides sufficient SNR within our experimental time (i.e. ~20 min). The study of dependence of CNR on TI demonstrated the possibility of obtaining satisfactory contrast

between different anatomical structures of the brain. Specifically, the values of TI providing optimum CNR for different brain structures *in vivo* at 9.4T were between 500 and 1000 ms. For TI = 500 ms, signal from GM is higher than from WM, while starting from TI = 1000 ms the relative contrast is reversed, enhancing WM/GM contrast, with the best results achieved for TI = 1000 ms. Literature studies in human and rodents brains have shown that increasing magnetic field causes decreasing difference in  $T_1$  values between myelin-rich (i.e. WM) and non-myelinated (i.e. GM) regions making it difficult to distinguish between these regions at a magnetic field above about 7T, at which the  $T_1$  ratio for WM/GM has been reported to be close to 0.9 (Guilfoyle, 2003; de Graaf, 2003; van de Ven, 2007; Kara, 2012). Our results show that using the cryo-coil and an appropriately selected inversion time, it is possible to obtain MR images with high WM/GM contrast within the experimental time (~20 min), that is reasonable for *in vivo* imaging. Moreover, it is possible to reverse WM/GM contrast by altering inversion time between 500 and 1000 ms. We have showed that by combining a IR-prepared UTE sequence with a properly selected TI and the application of the cryo-coil enables significant enhancement of the CNR from regions with short  $T_2$ , such as myelin-rich WM regions, of the mouse brain *in vivo* when compared to a standard volume coil. The results indicate feasibility of the application of the IR-UTE pulse sequence, with echo time shorter than 1 ms enabling assessment of regions with short  $T_2$ , such as myelin that may be related to different brain pathologies.

### **3.2.5 Application of the MP-RAGE pulse sequence for *in vivo* imaging of demyelination in the mouse model of MS**

While the results showed that IR-UTE is suitable for imaging of the animal model of MS, it does not allow multi-slice imaging within experimentally acceptable time due to application of non-selective IR pulses. To rectify this drawback, we also applied the magnetization prepared rapid acquisition gradient echo (MP-RAGE) pulse sequence allowing 3D images (Fig 1.10). To obtain the optimum contrast WM/GM in the mouse brain we investigated various MRI configurations of the MP-RAGE pulse sequence and the cryo-coil in the cuprizone mouse model of multiple sclerosis at 9.4T. Changes in MR images of the brains were confirmed with immunohistochemistry.

For *in vivo* MR imaging 4-month old C57BL/6J mice were used. The animals were anaesthetized with a mixture of isoflurane and oxygen:  $O_2:air = 0.75\%:0.25\%$ ; adjusted for

respiration frequency. The animals were placed in an imaging cradle and positioned within the magnet bore. An animal prepared for MRI is shown in Fig. 3.8.

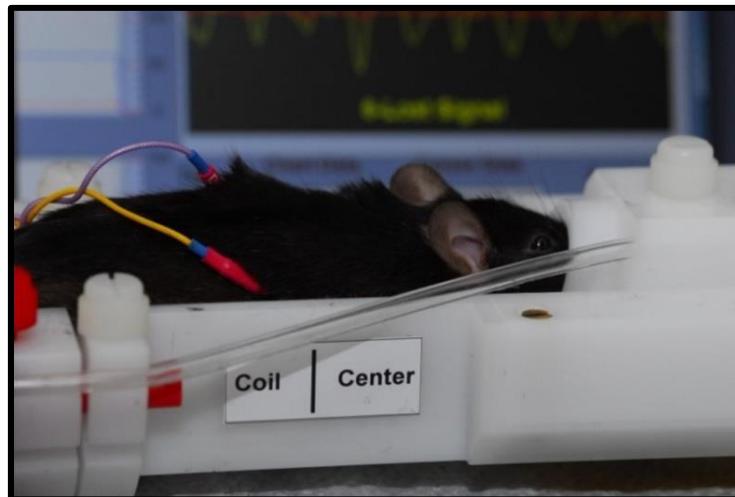


**Fig. 3.8** An animal prepared for an MRI session (IFJ/PAN 9.4T Lab).

For *in vivo* MRI experiments, sixteen mice were imaged: eight controlled and eight fed with cuprizone. As stated before, cuprizone was used to induce MS-like symptoms as orally administered copper chelator cuprizone (bis(cyclo-hexanone)oxaldihydrazone) produces reproducible demyelination in the mouse brain white matter (WM), particularly in the corpus callosum (cc) and, in some extend, in gray matter (GM).

A 9.4T/21cm horizontal bore Bruker Biospec MRI scanner (Paravision 5.0) equipped with a Bruker cryo-coil was used. The 3D MP-RAGE (Fig. 1.10) pulse sequence was used with following sequence parameters: TR/TE = 15/4.5 ms, Segment Repetition Time (SRT) = 6000 ms, FA = 12°, 26 horizontal 0.1 mm thick slices covering most of the brain, FOV = 1.80 x 1.50 x 0.26 cm, matrix = 256 x 256, in-plane resolution of 70 x 59  $\mu\text{m}$ . To find out the optimal IR time images with the following TIs were collected: 600, 800, 1000, 1100, 1200, 1400, 1600 and 2200 ms. Based on a pixel-by-pixel fitting of the mono-exponential inversion recovery curve, the  $T_1$ -map of the mouse brain was calculated, showing clear differences between highly myelinated white matter, gray matter and CSF (Fig. 3.9)

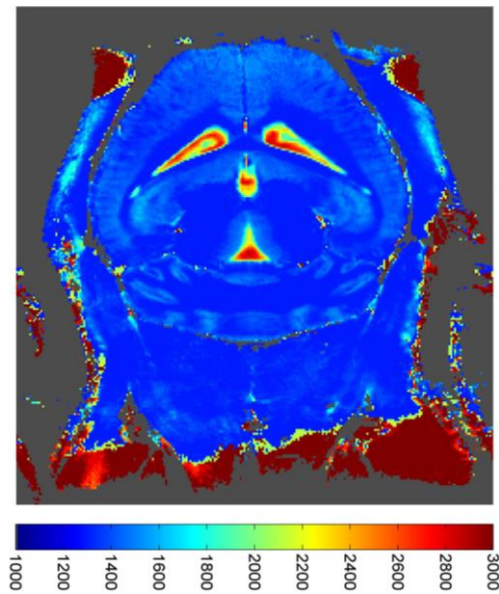


**Fig. 3.9**  $T_1$ -map of the horizontal slice obtained from the healthy mouse brain (color scale corresponds to  $T_1$  values in ms) collected using the MP-RAGE pulse sequence.

The highest WM/GM CNR was obtained at IR = 1000 ms and 1200 ms, corresponding to nulling of the WM and GM signal, respectively, hence only these images were used for further analysis and studies of the MS model (Fig. 3.10). Due to high SNR provided by the cryo-coil, the fine details are visible throughout the high resolution images. Histograms were calculated for different slices for each mouse to ensure coverage of the entire corpus callosum.

The average signal intensities of different brain regions for healthy and cuprizone mice representing white matter (WM), gray matter (GM) and cerebrospinal fluid (CSF) were calculated using ImageJ1.46r software (NIH, USA). Slices were selected at different distances from the cryo-coil surface. Histograms were made for slices in control and cuprizone treated animals.

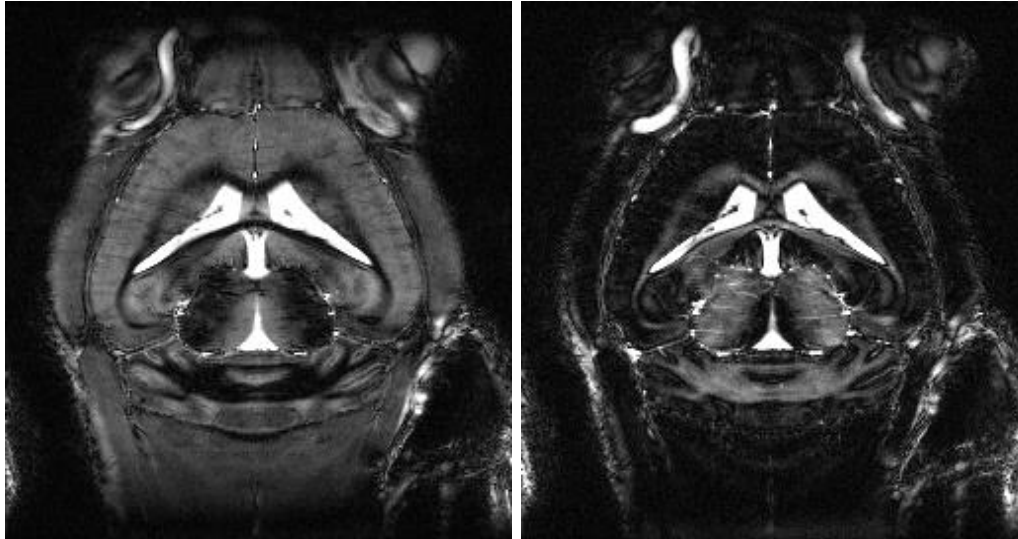


**Fig. 3.10** Example of a single slice horizontal image acquired using the MP-RAGE multislice pulse sequence of the healthy mouse brain *in-vivo*, obtained with inversion time (TI) equal to 1000 ms (left) and 1200 ms (right). The reversed contrast is visible, with signal from highly myelinated white matter nulled in the left image, while signal from the gray matter is nulled in the right image, clearly showing myelinated tissue with enhanced brightness.

The sagittal and horizontal MR images of the mouse brains of healthy and cuprizone treated animals using MP-RAGE with TI = 1200 ms are shown in Fig. 3.11. Fig. 3.12 shows calculated histograms of cerebellum obtained from these MR images. Figures 3.13, 3.14 and 3.15 show the results obtained at TI = 1000 ms. These selected parameters (TI = 1000 and 1200 ms) of the MP-RAGE pulse sequence are based on the maximum WM/GM CNR obtained with a healthy mouse and were used for the studies of demyelination in the cuprizone model of MS.

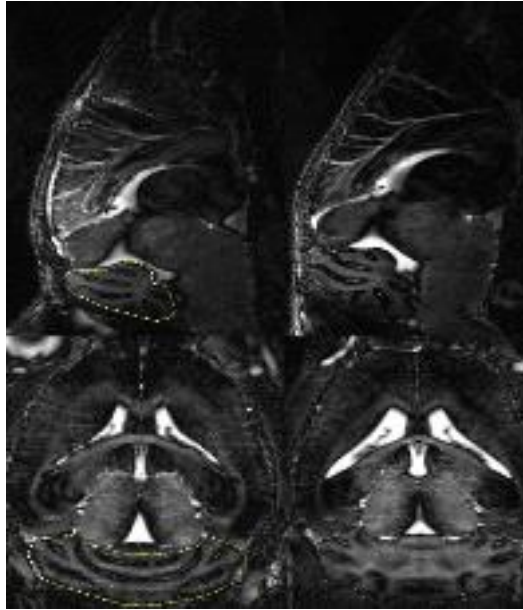


**Fig. 3.11** Sagittal (top) and horizontal (bottom) MP-RAGE images of the mouse brain (TI = 1200 ms) of healthy (left) and cuprizone (right) treated animals. Cerebellum comprising both WM and GM is marked with the yellow dotted line.

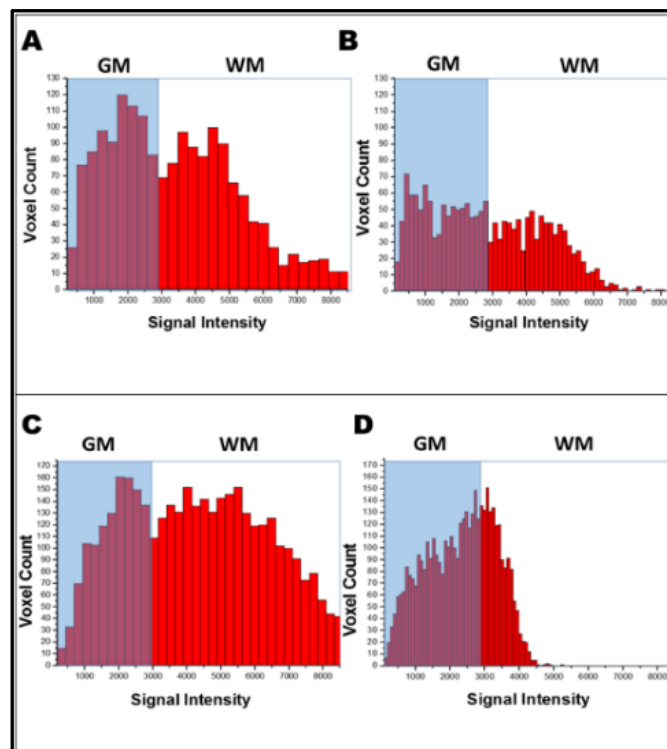


**Fig. 3.12** Histograms of cerebellum of healthy (A, C) and cuprizone treated animals (B, D) obtained with the MP-RAGE pulse sequence with IR = 1200 ms.

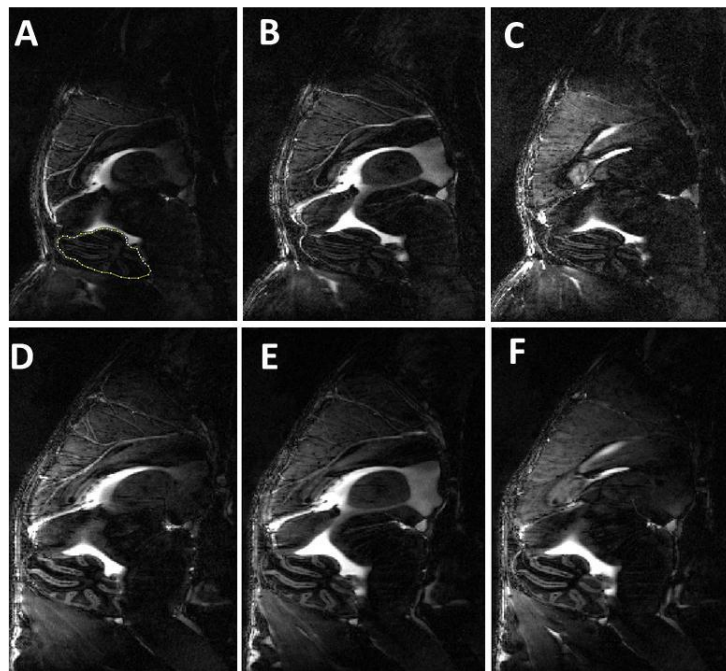


**Fig. 3.13** MP-RAGE sagittal images of a mouse brain (TI = 1000 ms) for healthy (A, B, C) and cuprizone treated animals (D, E, F). Three different slices of saggital cross-sections are presented for each mouse.

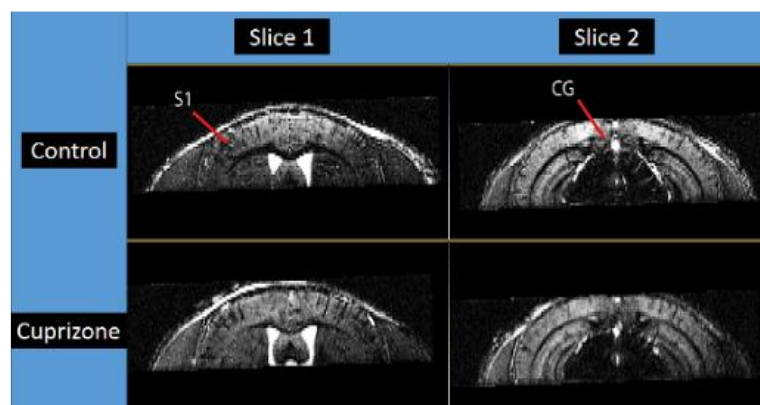


**Fig. 3.14** Comparison of axial cross-sections through MR images of the control and cuprizone treated animals obtained with the MP-RAGE pulse sequence (TI = 1000 ms). S1 - primary somatosensory cortex and CG - cingulate gyrus. Demyelination in corpus callosum is visible in the cuprizone treated animal.

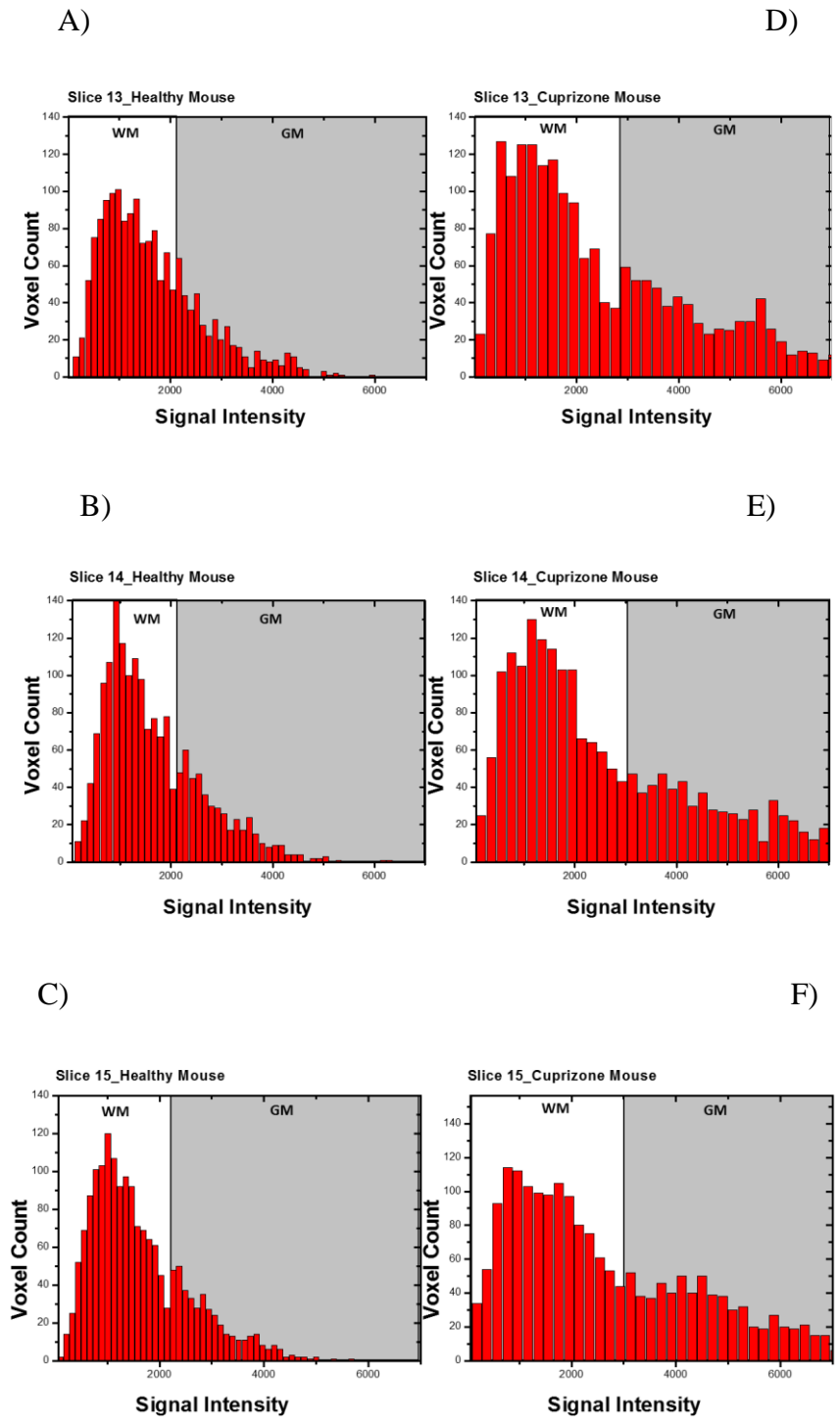


**Fig. 3.15** Histograms of cerebellum for healthy (A, B, C) and cuprizone treated animals (D, E, F). Three different slices have been presented for each mouse (TI = 1000 ms).

The images in Fig. 3.11 - 3.12 and 3.13 – 3.14. with TI = 1000 ms and TI = 1200 ms showed the highest differences in the control and cuprizone treated animals when compared to other TI times. The loss of myelin in the corpus callosum and cerebellum is clearly visible in the histograms.

We concluded that application of the MP-RAGE method with optimum parameters provided excellent WM/GM contrast improving assessment of demyelination in a mouse brain *in vivo*.

The images showed differences in the control and cuprizone treated animals. Using these optimized settings, we showed that patterns of myelination can be visualized in individual subjects. Application of the MP-RAGE pulse sequence at 9.4T with optimized parameters provided excellent WM/GM contrast in the corpus callosum as well as in the cerebellum region. The histograms show that the loss of myelin in the corpus callosum and cerebellum was significant. However, the exact determination of the areas of the brain undergoing demyelination was hindered due to presence of fine anatomic details related to e.g. blood circulatory system, which influence local signal intensity and its interpretation in terms of demyelination.

### **3.2.6 Quantitative evaluation of demyelination volume in *ex vivo* MP-RAGE images of the mouse brain.**

Following *in vivo* imaging, the animals were intracardiac perfused with formalin under anaesthesia, sacrificed, and their brains were extracted for further high resolution MR imaging *ex-vivo* and histopathological examinations. Extracted brains were stored in formaline solution, in the sample tubes appropriate for MRI measurements. The MP-RAGE experimental parameters defining image geometry were kept the same as in *in vivo* experiments, in order to obtain images with the same spatial resolution. However, due to the fact that T<sub>1</sub> values in formalin fixed tissue, measured at room temperature, were significantly lower than compared to *in vivo* measurements at physiological temperature, the TI values optimal for nulling signal from WM and GM tissue were also decreased to 500 ms and 650 ms respectively.

Examples of the obtained images are shown in Fig. 3.16. Good contrast between high and low-myelin areas of the brain is seen as it is not disturbed by the blood flow through the vessels and capillaries. The images show the areas most affected by cuprizone diet, i.e. corpus callosum and cerebellum.

In order to quantitatively assess the change of the myelinated volume in corpus callosum was manually delineated in all slices of the brain image for both the healthy and the cuprizone brain. The calculations of the entire delineated volume showed that the average myelinated corpus callosum volume decreased by  $(35 \pm 3)\%$ .

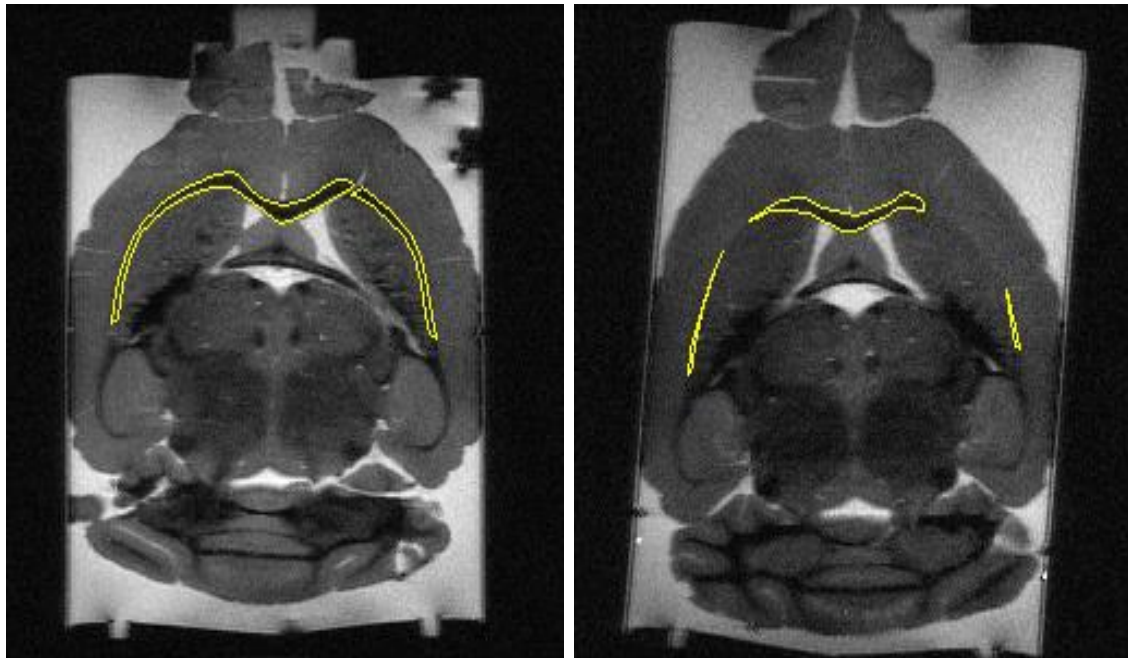


**Fig. 3.16** *Ex vivo* images of the brains from healthy (left) and cuprizone-fed (right) mice. The area of highly myelinated cc is significantly decreased in the cuprizone treated mouse.

Another easily recognised area affected by the cuprizone diet was cerebellum. Its volume was also assessed using histograms of the image intensities from the entire cerebellum volume for each slice. Examples of such histograms from the four adjacent slices through central cerebellum (most affected by the changes) are presented in Fig. 3.17 for the healthy and cuprizone-fed mice. Two-modal distribution of image intensities, corresponding to highly myelinated WM (left mode) and GM (right mode) can be easily distinguished for healthy animal, while significant decrease of the left mode, corresponding to myelinated tissue is

present in the cuprizone affected brain. Bi-modal Gaussian distribution was fitted to the data, in order to obtain the number of voxels corresponding to these two modes. The comparison between healthy and cuprizone affected cerebellum showed  $(10 \pm 2) \%$  decrease in the volume of the myelinated tissue.

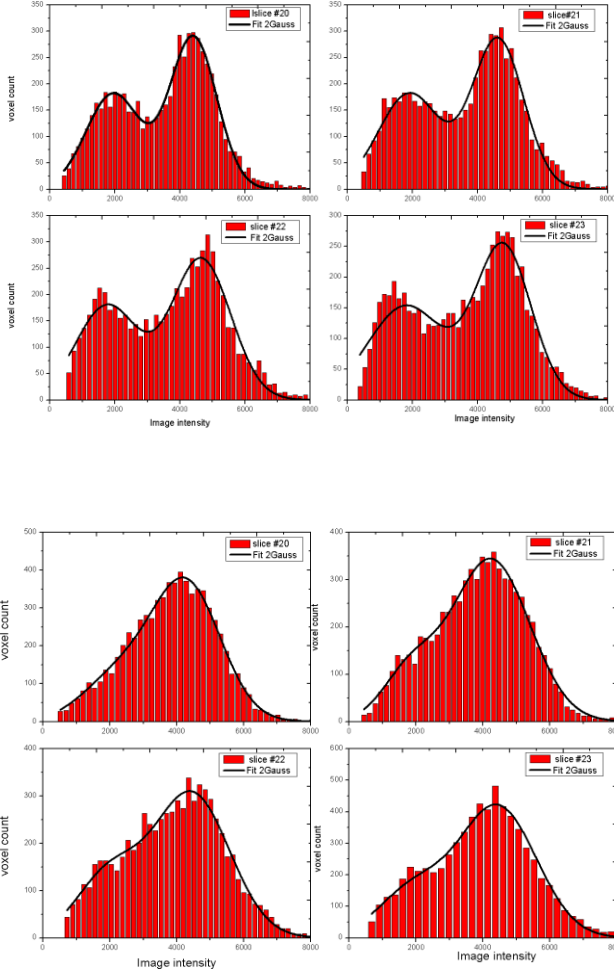


**Fig. 3.17** Histograms from four adjacent slices covering the central part of cerebellum for healthy (top) and cuprizone-fed (bottom) mice *ex vivo* obtained with the MP-RAGE pulse sequence with TI = 500 ms.

### **3.3 Histological assessment of demyelination in the brain of the mouse MS model.**

To correlate and confirm MRI results, histopathology studies were performed at the Department of Neuroanatomy, Jagiellonian University, using extracted brains of the same animals. In particular, the following structures within WM were investigated: WM in corpus callosum, cerebellar cortex, cerebral cortex, hippocampus, basal part of the forebrain and anterior commissure. The degree of myelination was established using Luxol Fast Blue dye due to the presence of lipoproteins and acid-alkaline reaction producing salt. Because this method has limited sensitivity and it does not detect subtle pathological changes in GM, immunohistochemistry of myelin was performed. This method allowed detection and visualisation of myelin basic protein (MBP), mitogen-activated protein (MAP) and myelin proteolipid protein (PLP), which are the major myelin components. Following this study original antibodies against these peptides were selected providing optimal quality of dying.

Significant decrease of myelin density was detected in corpus callosum in the cuprizone diet mouse. Interestingly, no evident changes were detected in other highly myelinated axon bundle connecting two brain hemispheres, i.e. anterior commissure (Figs. 3.18-19). This observation corresponds to the MRI results.

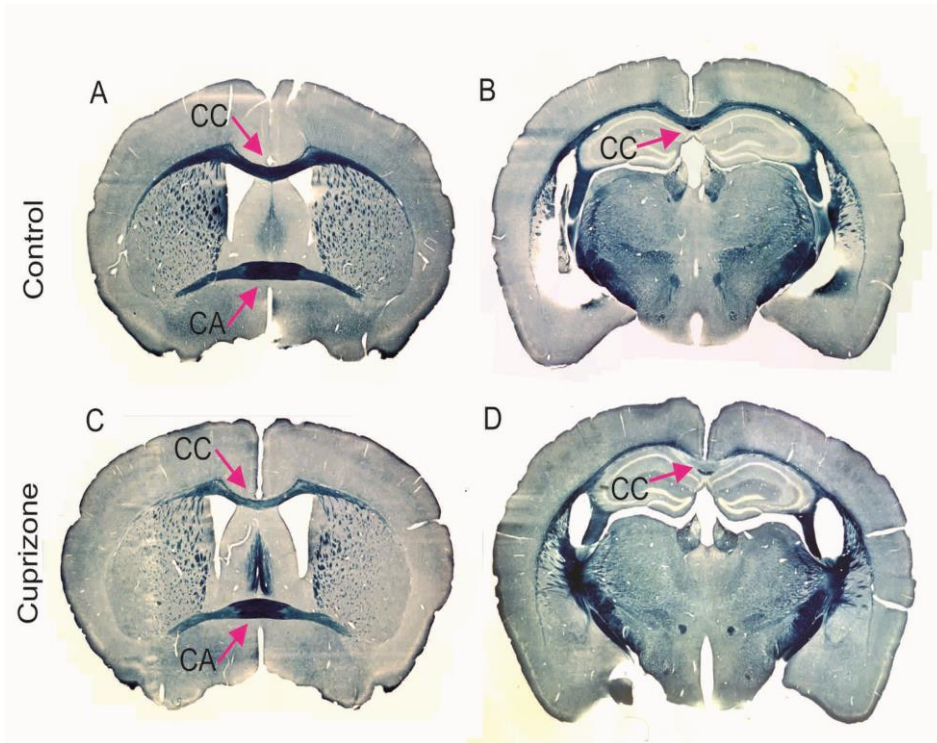


**Fig. 3.18** Histological images showing differences in myelin content in cc and CA in a control (healthy) animal and the animal fed with cuprizone diet (Source: Department of Neuroanatomy, Jagiellonian University).

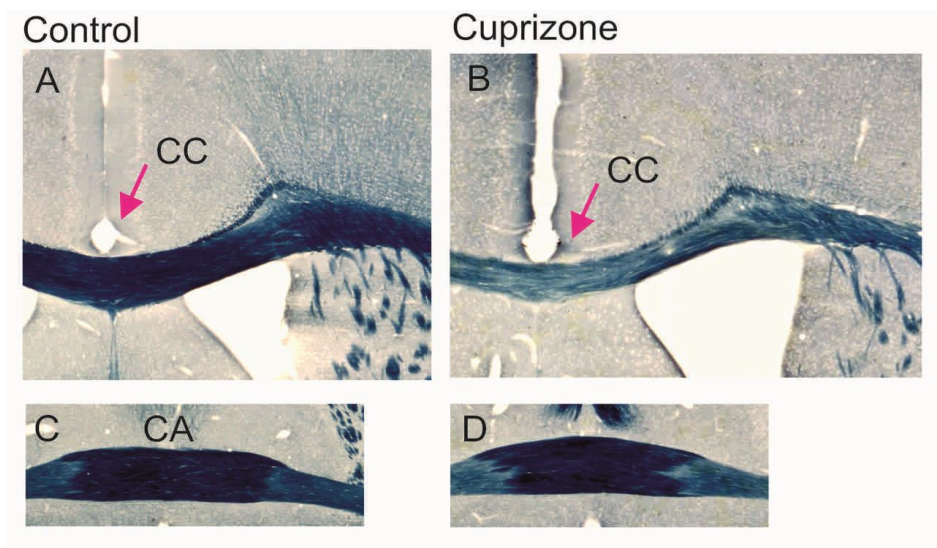


**Fig. 3.19** Zoomed histological images showing differences in myelin content in the selected brain areas of the control and cuprizone fed mouse. (Source: Department of Neuroanatomy, Jagiellonian University).

## 4. Discussion and Conclusions

In the presented studies several optimized pulse sequences was applied to enable MRI of myelin, hence early detection of MS. The investigated pulse sequences have advantages and disadvantages. The UTE pulse sequence allows imaging of very short  $T_2$  components, most directly related to myelin. However, it also collects signal from other macromolecular components of the brain tissue, hence the resulting image lacks acceptable contrast between myelinated and non-myelinated brain tissue. Adding the inversion pulse preceding the UTE imaging sequence (IR-UTE), which was accomplished in this work, allows to obtain satisfactory contrast between highly myelinated WM and poorly myelinated GM. However, the acquisition time for 3D imaging of the whole brain was found to be too long for practical *in vivo* experiments when non-selective inversion pulse is used. Moreover, SNR assessment in MR images obtained with pulse sequences with radial readout, such as UTE, may be questionable due to possible artifacts within FOV.

Application of the MP-RAGE pulse sequence allows high resolution 3D imaging within suitable total acquisition time, provides very good image quality and contrast. However, interpretation of the image contrast and thus exact assessment of local myelin content is not straightforward *in vivo*, due to blood flow in vessels and capillaries, hindering image interpretation. However, semi-quantitative assessment of the reduction of myelinated volume in the areas of the brain such as corpus callosum and parts of cerebellum is possible. Using the same pulse sequence for formalin fixed brains *ex vivo* provides excellent quantitative assessment of the change in the myelinated volume.

To obtain maximum SNR, the rf cryo-coil was applied and its sensitivity was assessed by comparing it with a volume coil. The comparison was achieved by collection of an additional image without transmitting rf power to assess “pure noise”. Using this approach SNR gain of  $\sim 2.5$  between cryo-coil and the same size surface coil (radius 12 mm) was reported by Baltes (2009). In our case SNR gain comparing to mouse brain surface receive-only rf coil was between 2.3 and 3.0 in the area of the brain (Piędzia, 2014). This allowed obtaining superior quality spin-echo and gradient echo MR images of the mouse brain *in vivo*. When the cryo-coil was compared with a volume birdcage coil (35 mm diameter), the SNR gain was significantly larger (i.e. 3- to 12-fold within the brain area).

The most demanding aspect of the research was to clearly distinguish and compare regions of similar relaxation times within the mouse brain at 9.4T. To rectify this issue, we

used the IR-UTE pulse sequence, that allowed to overcome the lack of suitable contrast between different regions of the brain, despite their similar proton density. The sequence was capable to measure signal with short  $T_2$ , such as myelin, and removing unwanted signal from tissues with long  $T_1$ , such as CSF. However, it allowed imaging of only few slices within experiment time. We have also applied Magnetization-Prepared Rapid Gradient Echo (MP-RAGE) pulse sequences, which have been used to image the human brain at 3 T and 7 T with very good  $T_1$  contrast (Marques, 2010; Kober, 2012; Jack, 2008). This technique provided good contrast for tissues with different  $T_1$ . However, due to its longer minimum TE, it is less suitable than IR-UTE for imaging tissues with very short  $T_2$ .

Other known approach to increase  $T_1$  contrast between WM and GM is manganese-enhanced magnetic resonance imaging (MEMRI) method (Silva, 2004). However, it requires application of a contrast agent. Considering its toxicity, we abandoned this approach.

Our study demonstrated improved CNR and SNR of WM and GM in the mouse brain MRI using the cryo-coil when compared to the room temperature birdcage and surface coils. However, the cryo-probe produces a non-uniform rf field, which allows homogeneous images in the horizontal plane only, parallel to the cryo-coil's surface. A further improvement in the image homogeneity could be obtained by the application of adiabatic pulses but at the cost of longer TE (Larson, 2007) and/or using volume cryo rf coil but it is not yet available.

Although the birdcage rf coil excites spins and detects signal uniformly over the entire brain volume thus provides homogeneous images in all orientations allowing quantification measurement, it produces relatively low SNR and thus it is not suitable for precise evaluation and visualization of the detailed brain structure *in vivo*, within a limited experimental time. As temperature of the cryo-coil is very low (about 20K) it generates practically no resistive noise providing much higher SNR than standard room temperature coils. Application of this coil for *in vivo* studies allowed improved distinction between different brain tissues when compared to a standard coil. However, precise adjustment of the two quadrature channels in terms of decoupling, as well as tuning and matching for each imaged slice is essential for obtaining homogeneous excitation over the image.

The aim of this research, namely to show that MRI can be indeed used for detection of changes in the demyelinating brain in the animal model of MS, was achieved. However, further studies are needed to fully assess physiological effects of e.g. blood circulation, inflammation or pathological iron content in brain tissues, on the image contrast *in vivo*. This requires application and investigation of optimal hardware (e.g. rf phase array coils) to

maximize SNR as well as parameters of the pulse sequences with inversion recovery pulses and/or short echo times. These studies may provide a clinical non-invasive tool for early detection of MS not available so far.

In summary the results showed that:

1. It is possible to image changes in myelin content in the animal model of MS based on both  $T_1$  and  $T_2$  relaxation times using appropriate pulse sequences and MR hardware, in particular:
  - single-slice IR-UTE pulse sequence with appropriately selected inversion time (TI) (1000-1200 ms) and
  - magnetization-prepared rapid gradient echo (MP-RAGE) pulse sequence allows detection of demyelination processes in the animal model of MS.
2. Application of the cryo-coil significantly increases SNR in the mouse brain MRI and it is highly recommended for the study of the animal model of MS at 9.4T.
3. The proper combination of pulse sequences and the cryo-coil allowed artifact-free MR imaging of myelin in the animal model of MS.
4. Use of the above imaging techniques to formalin-fixed brain tissue allows for quantitative and free from physiological artifacts, assessment of the demyelination extent.

## 5. References

- Abragam A, The Principles of Nuclear Magnetism, Oxford, 1961.
- Acs P, Kipp M, Norkute A. 17beta-estradiol and progesterone prevent cuprizone provoked demyelination of corpus callosum in male mice. *Glia* 2009; 57:807–814.
- Agosta F, Absinta M, Sormani MP, Ghezzi A, Bertolotto A, Montanari E, Comi G, Filippi M. In vivo assessment of cervical cord damage in MS patients: a longitudinal diffusion tensor MRI study. *Brain* 2007; 130:2211–19.
- Agosta F, Benedetti B, Rocca MA, Valsasina P, Rovaris M, Comi G, Filippi M. Quantification of cervical cord pathology in primary progressive MS using diffusion tensor MRI. *Neurology* 2005; 64:631–635.
- Aktas O, Schulze-Topphoff U, Zipp F. The role of TRAIL/TRAIL receptors in central nervous system pathology. *Front. Biosci.* (Landmark Ed) 2007, 12(8):2912–2921.
- Andrew ER, Nuclear Magnetic Resonance. Cambridge at the University Press, New York, 1955.
- Anon. Mouse Brain Atlas, Stereotaxic Coordinates. San Diego: Academic Press; 1998, available at: <http://www.mbl.org/atlas232/atlas232 frame.html> (accessed July2013).
- Appel M, Freeman JJ, Pusiol D, Robust Multi-Phase Flow Measurement Using Magnetic Resonance Technology. Paper presented at the SPE Middle East Oil and Gas Show and Conference, Manama, Bahrain, September 2011.
- Ascherio A. Environmental factors in multiple sclerosis. *Expert Rev Neurother* 2013; 13: 3–9.
- Avila RL, et al. Structure and stability of internodal myelin in mouse models of hereditary neuropathy. *J Neuropathol Exp Neurol* 2005; 64:976–990.
- Badea A, Ali-Sharief, AA, Johnson, GA. Morphometric analysis of the C57BL/6J mouse brain, *NeuroImage* 2007, 37(3):683-693.
- Bagnato F, Hametner S, Yao B, van Gelderen P, Merkle H, Cantor FK, et al. Tracking iron in multiple sclerosis: a combined imaging and histopathological study at 7 Tesla. *Brain* 2011; 134:3602-15.
- Bain A. Coherence levels and coherence pathways in NMR. A simple way to design phase cycling procedures. *J Magn Reson*, 1984; 56(3): 418-427.
- Baltes C, Radzwill N, Bosshard S, Marek D, Rudin M. Micro MRI of the mouse brain using a novel 400 MHz cryogenic quadrature RF probe. *NMR Biomed* 2009; 22(8):834–842.
- Banerjee D, Liou HC, Sen R. c-ReI-dependent priming of naive T cells by inflammatory cytokines. *Immunity* 2005; 23:445-458.
- Barkovich A. Concepts of myelin and myelination in neuroradiology. *Am J Neuroradiol* 2000; 21:1099–1109.
- Bartzokis G, Cummings JL, Sultzer D, Henderson VW, Nuechterlein KH, Mintz J. Whitematter structural integrity in healthy aging adults and patients with Alzheimer disease. A magnetic resonance imaging study. *Arch Neurol* 2003; 60(3):393–398.
- Bartzokis G, Lu P, Mintz J. Quantifying age-related myelin breakdown with MRI:novel therapeutic targets for preventing cognitive decline and Alzheimer’s disease. *J Alzheimers Dis* 2004; 6(6):53–59.

- Baudrexel S, Nürnberger L, Rüb U, Seifried C, Klein JC, Deller T, et al. Quantitative mapping of T1 and T2\* discloses nigral and brainstem pathology in early Parkinson's disease. *Neuroimage* 2010; 51(2):512–520.
- Bieber AJ, Rodriguez M. Experimental Models of Virus-Induced Demyelination. *Myelin Biology and Disorders*. 2004; 1073–100.
- Bielekova B, Martin R. Development of biomarkers in sclerosis. *Brain* 2004;127: 1463-1478.
- Bielekova B, Sung MH, Kadom N, Simon R, McFarland H, Martin R. Expansion and functional relevance of high-avidity myelin-specific CD4(+) T cells in multiple sclerosis. *J Immun* 2004; 172:3893-3904.
- Bjarnason TA, Vavasour IM, Chia CLL, MacKay AL. Characterization of the NMR behavior of white matter in bovine brain. *Magn Reson Med* 2005; 54(5):1072–1081.
- Blakemore WF, Demyelination of the superior cerebellar peduncle in the mouse induced by cuprizone. *J Neurol Sciences* 1973; 20(1):63-72.
- Bloch F, Hansen WW, Packard M. Nuclear Induction. *Phys Rev*. 1946; 70:474-485.
- Bloch F, Nuclear Induction, *Phys Rev* 1946; 70:460-474.
- Bock NA, Hashim E., Janik R., Konyer N. B., Weiss M., Stanisiz G. J., et al.. Optimizing T1-weighted imaging of cortical myelin content at 3.0 T. *Neuroimage* 2013; 65:1-12.
- Bottomley PA, Edelstein WA. Method of eliminating effects of spurious free induction decay NMR signal caused by imperfect 180 degrees pulses. US patent, 4484138, 1984.
- Brandt-Zawadzki M, Gillan GD, Nitz WR, MP RAGE: a three dimensional, T1-weighted gradient-echo sequence – initial experience in the brain. *Radiology* 1992; 182(3):769-775.
- Browne P, Chandraratna D, Angood C, et al. Atlas of multiple sclerosis 2013: a growing global problem with widespread inequity. *Neurology* 2014; 83: 1022–1024.
- Brunton LL. Immunomodulators. In: Lazo JS, Parker KL, editors. Goodman & Gilman's The Pharmacological Basis of Therapeutics. 11th ed. New York: McGraw-Hill Medical; 2005. 1424–1427.
- Carr HY, Parcell EM. Effects of diffusion on free precession in nuclear magnetic resonance experiments. *Phys. Rev*. 1954; 94(3):630-638.
- Chard, D.T., Alahmadi, A.A.S., Audoin, B. et al. Mind the gap: from neurons to networks to outcomes in multiple sclerosis. *Nat Rev Neurol* 2021, 17:173–184.
- Chavez S, Stanisiz GJ, A novel method for simultaneous 3D B1 and T1 mapping: the method of slopes (MoS). *NMR Biomed* 2012; 25(9):1043–1055.
- Chen JT, Kuhlmann T, Jansen GH et al. Voxel-based analysis of the evolution of magnetization transfer ratio to quantify remyelination and demyelination with histopathological validation in a multiple sclerosis lesion. *Neuroimage* 2007; 36:1152–8.
- Chuang N, Mori S, Yamamoto A, Jiang H, Ye X, Xu X, Richards LJ, Nathans J, Miller MI, Toga AW, Sidman RL, Zhang J. An MRI-based Atlas and Database of the Developing Mouse Brain, *Neuroimage*, 2011 54(1):80-89.
- Confavreux C, Compston A. The Natural History of Multiple Sclerosis. In: Compston A, McDonald I, Noseworthy J et al, Editors. McAlpine's Multiple Sclerosis. Churchill Livingstone, 2005; 183-272.

- Cooke SF, Bliss TVP. Plasticity in the human central nervous system. *Brain* 2006; 129:1659-1673.
- Cree BAC. Multiple sclerosis. In: Brust JCM, editor. *Current Diagnosis and Treatment in Neurology*. New York: Lange Medical Books/McGraw-Hill Medical; 2007
- de Graaf RA, Brown PB, McIntyre S, Nixon TW, Behar KL, Rothman DL. High magnetic field water and metabolite proton T1 and T2 relaxation in rat brain in vivo. *Magn Reson Med* 2003; 2–3(56):386–94.
- de Graaf RA, Brown PB, Scott McIntyre, Terence W. Nixon, Kevin L. Behar, and Douglas L. Rothman High Magnetic Field Water and Metabolite Proton T1 and T2 Relaxation in Rat Brain In Vivo, *Mag Reson Med* 2006; 56:386–394.
- DeLuca GC, Williams K, Evangelou N, Ebers GC, Esiri MM. The contribution of demyelination to axonal loss in multiple sclerosis. *Brain* 2006; 129:1507–16.
- Deoni SCL, Rutt BK, Arun T, Pierpaoli C, Jones DK. Gleaning multicomponent T1 and T2 information from steady-state imaging data. *Magn Reson Med* 2008; 60:1372–87.
- Dobson, R., Giovannoni, G. Multiple sclerosis – a review. *Eur J Neurol*, 2019;26: 27-40.
- Does M, Gore J. Compartmental study of T1 and T2 in rat brain and trigeminal nerve in vivo. *Magn Reson Med* 2002; 47:274–83.
- Dousset V, et al. Experimental allergic encephalomyelitis and multiple sclerosis: Lesion characterization with magnetization transfer imaging. *Radiology* 1992; 182:483–491.
- Du G, Lewis MM, Styner M, Shaffer ML, Sen S, Yang QX, et al. Combined R2\* and diffusion tensor imaging changes in the substantia nigra in Parkinson's disease. *Mov Disord* 2011; 26(9):1627–32.
- Du J, Michael Carl, Mark Bydder, Atsushi Takahashi, Christine B. Chung, Graeme M. Bydder, Qualitative and quantitative ultra-short echo time (UTE) imaging of cortical bone, *J Magn Res* 2010; 207(2): 304-311.
- Du J. Short T2 contrast with three-dimensional ultra-short echo time imaging. *J Magn Reson Imag* 2001; 29:470–82.
- Ebers GC, Sadovnick AD. The Geographic-Distribution of Multiple-Sclerosis - A Review. *Neuroepidemiology* 1993; 12:1-5.
- Ernst RR, Anderson WA Application of Fourier Transform Spectroscopy to Magnetic Resonance, *Rev. Sci. Instr.* 1965; 36:1696..
- Ernst RR, Bodenhausen G, Wokaun A. Principles of Magnetic Resonance in One and Two Dimensions. Oxford, New York, 1987.
- Fellner E, Holl K, Held P, Fellner C, Schmitt R, Bohm-Jurkovic H. A T1-weighted rapid three-dimensional gradient-echo technique (MP-RAGE) in preoperative MRI of intracranial tumours. *Neuroradiology* 1996; 38:199-206.
- Filippi M, Preziosa P, Barkhof F, et al. Diagnosis of Progressive Multiple Sclerosis From the Imaging Perspective: A Review. *JAMA Neurol.* 2021;78(3):351–364
- Frahm J, Haase A, Matthaei D. Rapid NMR imaging of dynamic processes using the FLASH technique. *Magn Reson Med*, 1986; 3:321-327.
- Frahm J, Haase A. Matthaei D. Rapid three-dimensional MR imaging using the FLASH technique. *J Comput Assist Tomogr* 1986;10(2):363-368.

- Freeman R, Kempf SP, Levitt MH. Radiofrequency pulse sequences which compensate their own imperfections. *J Magn Reson* 1980; 38:453-479.
- Frisoni GB, Fox NC, Jack CR Jr, Scheltens P, Thompson PM. The clinical use of structural MRI in Alzheimer disease. *Nat Rev Neurol* 2010; 6(2):67-77.
- Frullano L, Wang C, Miller RH, Wang Y. A myelin-specific contrast agent for magnetic resonance imaging of myelination. *J Am Chem Soc* 2011; 133:1611-1613.
- Fu L, Matthews PM, De Stefano N, Worsley KJ, Narayanan S, Francis GS, et al. Imaging axonal damage of normal-appearing white matter in multiple sclerosis. *Brain* 1998; 121:103-13.
- Fu Y, Huff TB, Wang HW, Wang H, Cheng JX, Ex vivo and in vivo imaging of myelin fibers in mouse brain by coherent anti-Stokes Raman scattering microscopy. *Opt Express* 2008; 16:19396-19409.
- Fujima N, Homma A, Harada T, Shimizu Y, Tha KK, Kano S, Mizumachi T, Li R, Kudo K, Shirato H. The utility of MRI histogram and texture analysis for the prediction of histological diagnosis in head and neck malignancies. *Cancer Imaging*. 2019; 4,19(1):5.
- Fujinami RS, Von Herrath MG, Christen U, Whitton JL. Molecular mimicry, bystander activation, or viral persistence: Infections and autoimmune disease. *Clinical Microbiology Reviews* 2006; 19:80.
- Gareau P, Rutt B. Magnetization transfer and multicomponent T2 relaxation measurements with histopathologic correlation in an experimental model of MS. *J Magn Reson Imaging* 2002; 11:586-95.
- Gatehouse P, Thomas R, Robson M. Magnetic resonance imaging of the knee with ultra-short TE pulse sequences. *Magn Reson Imag* 2004; 22:1061-1067.
- Grenier D, Pelletier D, Normandeau M, Newitt D, Nelson S, Goodkin DE, et al. T2 relaxation time histograms in multiple sclerosis. *Magn Reson Imag* 2002; 20:733-741.
- Gudbjartsson H, Patz S. The Rician distribution of noisy MRI data. *Magn Reson Med* 1995; 34(6):910-4.
- Guilfoyle DN, Dyakin VV, O'Shea J, Pell GS, Helpert JA. Quantitative measurements of proton spin-lattice (T1) and spin-spin (T2) relaxation times in the mouse brain at 7.0 T. *Magn Reson Med* 2003; (49):576-580.
- Haacke EM, Brown RW, Thomson MR, Venkatesan R, Magnetic Resonance Imaging Physical Principles and Sequence Design, John Wiley and Sons, Inc. New York, USA, 1999.
- Haacke ME, Xu Y, Cheng XC, Reichenbach JR. Susceptibility-weighted imaging (SWI). *Magn Reson Med* 2004; 52(3):612-8.
- Hahn EL, An Accurate Nuclear Magnetic Resonance Method for Measuring Spin-Lattice Relaxation Times, *Phys. Rev.* 1949; 76:145-146.
- Hahn EL. Nuclear Induction Due to Free Larmor Precession, *Phys. Rev.* 1950; 77(2):278-297.
- Hahn EL. Spin Echoes. *Phys. Rev.* 1950; 80:580-585.
- Harkins KD, Dula AN, Does MD. The effect of inter-compartmental water exchange on the apparent myelin water fraction in multi-exponential T2 measurements of rat spinal cord. *Magn Reson Med* 2012; 67 (3):793-800.

- Harsan et al. Recovery from Demyelination by Thyroid Hormone Therapy. *J. Neurosci*, 2008; 28(52):14189–14201.
- Harsan LA, Steibel J, Zaremba A et al. Recovery from chronic demyelination by thyroid hormone therapy: myelinogenesis induction and assessment by diffusion tensor magnetic resonance imaging. *J Neurosci* 2008; 28:14189–14201.
- Hartung HP, Bar-Or A, Zoukos Y. What do we know about the mechanism of action of disease-modifying treatments in MS? *J Neurology* 2004; 251:12-20.
- He X, Janeway CA, Levine M *et al.* Dual receptor T cells extend the immune repertoire for foreign antigens. *Nature Immunology* 2002; 3:127-134.
- Helms G, Hagberg GE. In vivo quantification of the bound pool T1 in human white matter using the binary spin-bath model of progressive magnetization transfer saturation. *Phys Med Biol* 2009; 54:N529.
- Hemmer B, Archelos JJ, Hartung HP. New Concepts in the Immunopathogenesis Of Multiple Sclerosis. *Nature Reviews*, 2002; 3:291-301
- Hendrick RE, Nelson TR, Hendee WR. Optimizing tissue contrast in magnetic resonance imaging. *Magn Reson Imag* 1984; 2(3):193-204.
- Herder, V., Hansmann, F., Stangel, M., Skripuletz, T., Baumgärtner, W. Beineke, A., Lack of cuprizone-induced demyelination in the murine spinal cord despite oligodendroglial alterations substantiates the concept of site-specific susceptibilities of the central nervous system. *Neuropathology and Applied Neurobiology*, 2011, 37:676-684.
- Herndon C, Lancaster J, Toga A, Fox P. Quantification of white matter and gray matter volumes from T1 parametric images using fuzzy classifiers. *J Magn Reson Imag* 1996; 6:425–35.
- Hiremath MM, Saito Y, Knapp GW, Ting JP, Suzuki K, Matsushima GK. Microglial/macrophage accumulation during cuprizone-induced demyelination in C57BL/6 mice. *J Neuroimmunol* 1998; 92(1-2):38-49.
- Holmes S, Friese MA, Siebold C, Jones EY, Bell J, Fugger L. Multiple sclerosis: MHC associations and therapeutic implications. *Expert Reviews in Molecular Medicine*. 2005; 7(3):1-17.
- Hoult DI, Cheng CN, Sang VJ. Quadrature detection in the laboratory frame, Quadrature detection, *Magn Reson Med*. 1984; 1(3):339-353.
- Hoult DI, The Principle of reciprocity *J Magn Reson*. 2011; 213:344-346.
- Hurlimann MD, Griffin DD. Spin Dynamics of Carr–Purcell–Meiboom–Gill-like Sequences in Grossly Inhomogeneous B0 and B1 Fields and Application to NMR Well Logging, *J Magn Reson*. 2000; 143(1):120–135.
- Hutchison JM, Sutherland RJ, Mallard JR, NMR Imaging: image recovery under magnetic fields with large nonuniformities, *J Phys E: Scient Instrum* 1978; 1:217.
- Jack CR Jr, Bernstein MA, Fox NC, Thompson P, Alexander G, Harvey D, et al. The Alzheimer’s disease neuroimaging initiative (ADNI): MRI methods. *J Magn Reson Imag* 2008; 27(4):685–91.
- Kara F, Chen F, Ronen I, de Groot HJ, Matysik J, Alia A. In vivo measurement of transverse relaxation time in the mouse brain at 17.6 T. *Magn Reson Med*. 2013; 70(4):985-993.

- Kim, BS. Excessive Innate Immunity Steers Pathogenic Adaptive Immunity in the Development of Theiler's Virus-Induced Demyelinating Disease. *Int. J. Mol. Sci.* 2021,22: 5254.
- Kirsch S, Augath M, Seiffge D, Schilling L, Schad LR. In vivo chlorine-35, sodium-23 and proton magnetic resonance imaging of the rat brain. *NMR Biomed* 2010; 23(6):592-600. Fig 3.
- Kobelt G, Thompson A, Berg J, et al. New insights into the burden and costs of multiple sclerosis in Europe. *Mult Scler* 2017; 23: 1123– 1136.
- Kober T, Granziera C, Ribes D, Browaeys P, Schlupe M, Meuli R, et al. MP2RAGE multiple sclerosis magnetic resonance imaging at 3 T. *Invest Radiol* 2012; 47(6):346–352.
- Koenig S, Brown R III, Spiller M, Lundbom N. Relaxometry of brain: why white matter appears bright in MRI. *Magn Reson Med* 1990; 14(3):482–495.
- Koenig SH. Cholesterol of myelin is the determinant of gray-white contrast in MRI of brain. *Magn Reson Med* 1991; 20(2):285–291.
- Komoly S, Experimental demyelination caused by primary oligodendrocyte dystrophy. Regional distribution of the lesions in the nervous system of mice [corrected]. *Ideggyogyaszati Szemle.* 2005; 58(1-2):40-43.
- Kozlowski P, Liu J, Yung AC, Tetzlaff W. High-resolution myelin water measurements in rat spinal cord. *Magn Reson Med* 2008; 59 (4):796–802.
- Kurtzke JF. Epidemiology in multiple sclerosis: a pilgrim's progress. *Brain* 2013; 136: 2904–2917.
- Kutzelnigg A, Lucchinetti CF, Stadelmann C *et al.* Cortical demyelination and diffuse white matter injury in multiple sclerosis. *Brain* 2005; 128:2705-2712.
- Labadie C, Lee J-H, Rooney WD, Jarchow S, Aubert-Frécon M, Springer CS Jr, et al. Myelin water mapping by spatially regularized longitudinal relaxographic imaging at high magnetic fields. *Magn Reson Med* 2014; 71:375–387.
- Lancaster JL, Andrews T, Hardies LJ, Dodd S, Fox PT. Three-pool model of white matter. *J Magn Reson* 2003;17(1):1–10.
- Larson PE, Conolly SM, Pauly JM, Nishimura DG. Using adiabatic inversion pulses for long-T2 suppression in ultra-short echo time (UTE) imaging. *Magn Reson Med* 2007; 58:952–961.
- Larson PE, Gurney PT. Designing long-T2 suppression pulses for ultra-short echo time imaging. *Magn Reson Med* 2006; 56(1): 94–103.
- Laule C, et al. Myelin water imaging of multiple sclerosis at 7T: Correlations with histopathology. *Neuroimage* 2008; 40:1575–1580.
- Laule C, et al. Water content and myelin water fraction in multiple sclerosis: a T2 relaxation study. *J Neurol* 2004; 251:284–93.
- Laule C, Leung E, Li D. Myelin water imaging in multiple sclerosis: quantitative correlations with histopathology. *Mult Scler* 2006; 12(6):747–53.
- Lauterbur PC, Image formation by induced local interactions. Examples employing NMR. *Nature*, 1973; 242:190.
- Levitt MH, Ernst RR. Composite pulses constructed by a recursive expansion procedure. *J Magn Reson* 1983; 55(2):247-254.

- Levitt MH, Freeman R. Compensation for pulse imperfections in NMR spin-echo experiments. *J Magn Reson* 1981; 43:65-80.
- Levitt MH, Freeman R. NMR Population Inversion Using a Composite Pulse, *J Magn Reson* 1979; 33:473-476.
- Levitt MH. Composite Pulses. *Progress in NMR Spectroscopy* 1986; 18:61-122.
- Levitt MH; Symmetrical composite pulse sequences for NMR population inversion. II. Compensation of resonance offset. *J Magn Reson* 1982; 50:95-110.
- Logothetis, N. What we can do and what we cannot do with fMRI. *Nature*. 2008; 453:869–878
- Lovett-Racke AE, Trotter JL, Lauber J, Perrin PJ, June CH, Racke MK. Decreased dependence of myelin basic protein-reactive T cells on CD28-mediated costimulation in multiple sclerosis patients - A marker of activated/memory T cells. *J Clin Invest* 1998; 101:725-730.
- Lublin FD, Reingold SC. Defining the clinical course of multiple sclerosis: Results of an international survey. *Neurology* 1996; 46:907-911.
- Lucchinetti C, Bruck W, Parisi J, Scheithauer B, Rodriguez M, Lassmann H. Heterogeneity of multiple sclerosis lesions: Implications for the pathogenesis of demyelination. *Ann. Neurology* 2000; 47:707-717.
- Ludwin SK, Central nervous system demyelination and remyelination in the mouse: an ultrastructural study of cuprizone toxicity. *Laboratory Investigation; a Journal of Technical Methods and Pathology*. 1978, 39(6):597-612.
- McGinley MP, Goldschmidt CH, Rae-Grant AD. Diagnosis and Treatment of Multiple Sclerosis: A Review. *JAMA*. 2021; 325(8):765–779
- MacKay A, Whittall K, Adler J, Li D, Paty D, Graeb D. In vivo visualization of myelin water in brain by magnetic resonance. *Magn Reson Med* 1994; 31:673–7.
- MacKay AL, Laule C. Magnetic Resonance of Myelin Water: An in vivo Marker for Myelin, *Brain Plasticity*, 2016; 2(1):71-91.
- Madsen LS, Andersson EC, Jansson L *et al*. A humanized model for multiple sclerosis using HLA-DR2 and a human T-cell receptor. *Nature Genetics* 1999; 23:343-347.
- Mansfield P, Grannell, NMR “diffraction” in solids? *J Phys C: Solid State Phys* 1973; 6:L422.
- Mao J, Mareci TH, Andrew ER. Experimental Study of Optimal Selective 180 Radiofrequency Pulses, *J Mag Reson* 1988; 79:1-10.
- Marques JP, Kober T, Krueger G, van der Zwaag W, Van de Moortele PF, Gruetter R. MP2RAGE, a self bias-field corrected sequence for improved segmentation and T1-mapping at high field. *Neuroimage* 2010; 49:1271–81.
- McCreary CR, Bjarnason TA, Skihar V, Mitchell JR, Yong Wee V, Dunn JF. Multiexponential T2 and magnetization transfer MRI of demyelination and remyelination in murine spinal cord. *Neuroimage* 2009; 45(4):1173–82.
- Modin H, Olsson W, Hillert J, Masterman T. Modes of action of HLA-DR susceptibility specificities in multiple sclerosis. *Am J Human Genetics* 2004; 74:1321-1322.

- Mottershead JP, Schmierer K, Clemence M, Thornton JS, Scaravilli F, Barker GJ, et al. High field MRI correlates of myelin content and axonal density in multiple sclerosis. *J Neurol* 2003; 250(11):1293–301.
- Neema M, Stankiewicz J, Arora A. T1- and T2-based MRI measures of diffuse gray matter and white matter damage in patients with multiple sclerosis. *J Neuroimaging* 2007; 17(1):16–21.
- NFZ, Raport o Zdrowiu: Stwardnienie rozsiane, Centrala Narodowego Funduszu Zdrowia Departament Analiz i Innowacji, Warszawa 2021.
- Oksenberg JR, Barcellos LF, Cree BAC *et al.* Mapping multiple sclerosis susceptibility to the HLA-DR locus in African Americans. *Am J Human Genetics* 2004; 74:160-167.
- Piędzia W, Bock N, Jasiński K, Kalita K, Stanisiz G, Węglarz WP, MR imaging of the mouse brain using cryo-coil at 9.4T - histology in vivo? Abstr. of XLV Polish Seminar on Nuclear Magnetic Resonance and Its Applications, 1-2 December 2014, Krakow, in IFJ Report, 2077/AP 2014, p. 37;
- Piędzia W, Jasiński K, Kalita K, Bartel Z, Węglarz WP, Detection of Myelin Changes *in vivo* Using High Field MRI, Proc 8<sup>th</sup> Pan-Asian Committee for Treatment and Research in Multiple Sclerosis (PACTRIMS), Seoul, South Korea, Nov 19-21, 2015. *Multiple Sclerosis Journal* 22(3):413, 2016.
- Piędzia W, Jasiński K, Kalita K, Tomanek B, Węglarz W, White and gray matter contrast enhancement in MR images of the mouse brain in vivo using IR UTE with a cryo-coil at 9.4 T. *J Neurosc Meth* 232:30–35, 2014.
- Piędzia W, Jasiński K, Kalita K, Tomanek B, Węglarz WP. MRI of myelin as a potential tool for early diagnosis of multiple sclerosis, Proc. 6<sup>th</sup> Congress of the Pan Asian Committee on Treatment and Research in Multiple Sclerosis (PACTRIMS), Kyoto, Japan, 6-8 November 2013, *Multiple Sclerosis Journal*, 20(7):920, 2014.
- Piędzia W, Jasiński K, Kalita K, Węglarz WP, T1 relaxation measurements in the mouse brain in vivo using Variable Flip Angle - UTE with a cryo-coil at 9.4 T, *ISMRM 21st Annual Meeting and Exhibition*, Salt Lake City, USA, April 20 – 26, 2013
- Piędzia W, Jasiński K, Kalita K, Węglarz WP, T1 relaxation measurements in the mouse brain in vivo using Variable Flip Angle - UTE with a cryo-coil at 9.4T, Proc. of Joint ISMRM-ESMRMB Meeting, Milan, Italy, 10-16 May 2014; 3280.
- Piędzia W, Jasiński K, Kalita K, Węglarz WP. 7<sup>th</sup> World Congress on Controversies in Neurology (CONy) Istanbul, Turkey, April 11-14, 2013.
- Piędzia W, Jasinski K, Węglarz WP, Comparison of different MRI pulse sequences for quantitative T<sub>2</sub> measurements in preclinical studies, *ESMRM, 30th Annual Scientific Meeting*, October 3-5, 2012, Lisbon, Portugal.
- Piędzia, W, Jasinski K, Kalita K, Tomanek B, Węglarz WP, Enhancement of the Myelin Rich Regions in MR Images in the Mouse Brain in vivo Using IR-UTE with a Cryo-Coil at 9.4 T. *ISMRM 21st Annual Meeting and Exhibition*, Salt Lake City, USA, April 20 – 26, 2013.
- Pierce JR. Physical Sources of Noise. *Proceedings of the IRE*. 1956; 44 (5):601–608.
- Piredda, GF, Hilbert, T, Thiran, J-P, Kober, T. Probing myelin content of the human brain with MRI: A review. *Magn Reson Med*. 2020; 85:627– 652.
- Poon CS, Henkelman RM. Practical T2 quantitation for clinical applications. *J Magn Reson Imag* 1992; 2:541–53.

- Purcell E, Torrey H, Pound R. Resonance Absorption by Nuclear Magnetic Moments in a Solid. *Physical Rev.* 1950; 69: 37.
- Rabi II, Zacharias JR, Millman S, Kusch P. A New Method of Measuring Nuclear Magnetic Moment. *Physical Review.* 1938; 53(4):318–327.
- Rahmanzadeh, R., Galbusera, R., Lu, P.-J., et al, A New Advanced MRI Biomarker for Remyelinated Lesions in Multiple Sclerosis. *Ann Neurol*, 2022, 92:486-502
- Ratering D, Baltes C, Nordmeyer-Massner J, Marek D, Rudin M. Performance of a 200-MHz cryogenic rf probe designed for MRI and MRS of the murine brain. *Magn Reson Med* 2008; 59:1140–447.
- Reeder SB, Atalar E, Bolster BD, Jr., McVeigh ER, Quantification and Reduction of Ghosting Artifacts in Interleaved Echo-Planar Imaging. *Magn Reson Med.* 1997; 38(3):429–439.
- Research Gate, [https://www.researchgate.net/publication/321716019\\_Physics-based\\_data\\_analysis\\_for\\_wind\\_turbine\\_condition\\_monitoring/figures?lo=1](https://www.researchgate.net/publication/321716019_Physics-based_data_analysis_for_wind_turbine_condition_monitoring/figures?lo=1)
- Robson MD, Gatehouse PD, Bydder M, Bydder GM, Magnetic Resonance: An Introduction to Ultra-short TE (UTE) Imaging. *J Comput Assist Tomogr* 2003; 27(6):825-846.
- Rovaris M, Bozzali M, Santuccio G, Ghezzi A, Caputo D, Montanari E, Bertolotto A, Bergamaschi R, Capra R, Mancardi G, Martinelli V, Comi G, Filippi M. In vivo assessment of the brain and cervical cord pathology of patients with primary progressive multiple sclerosis. *Brain* 2001; 124:2540–9.
- Seppo Äyräväinen Hut, Antialiasing. *Telecommunications Software and Multimedia Laboratory, Computer Science*, 2002, <https://www.semanticscholar.org/>
- Schnack HG, et al., Automated Separation of Gray and White Matter from MR Images of the Human Brain, *NeuroImage*, 2001; 13(1): 230-237.
- Silva AC, Lee JH, Aoki I, Koretsky AP. Manganese-enhanced magnetic resonance imaging (MEMRI): methodological and practical considerations. *NMR Biomed* 2004; 17:532–43.
- Stidworthy MF, Genoud S, Suter U, Mantei N, Franklin RJM. Quantifying the Early Stages of Remyelination Following Cuprizone-induced Demyelination. *Brain Pathology* 2003; 13(3):245-415.
- Tench CR, Morgan PS, Jaspan T, Auer DP, Constantinescu CS. Spinal cord imaging in multiple sclerosis. *J Neuroimaging* 2005; 15:94S–102S.
- Teunissen CE, Dijkstra C, Polman C. Biological markers in CSF and blood for axonal degeneration in multiple sclerosis. *The Lancet Neurology.* 2005; (4)1:32-41,
- Torkildsen O, Brunborg LA, Myhr K-M, Bo L. The cuprizone model for demyelination. *Acta Neurol Scand* 2008; 117 (Suppl. 188):72–76.
- Torrey HC, Bloch Equations with Diffusion Terms. *Phys. Rev.* 1956; 104:563.
- Torrey HC, Transient Nutations in Nuclear Magnetic Resonance. *Phys. Rev.* 1949; 76:1059.
- Tyler DJ, Robson MD, Henkelman RM, Young IR, Bydder GM, MB. Magnetic Resonance Imaging with Ultra-short TE (UTE) PULSE Sequences: Technical Considerations, *J Mag Reson Imag* 2007; 25:279–289.
- Van de Ven RC, Hogers B, van den Maagdenberg AM, de Groot HJ, Ferrari MD, Frants RR, et al. T1 relaxation in in vivo mouse brain at ultra-high field. *Magn Reson Med* 2007; 58:390–395.

- Vandebergh M, Dubois B, Effects of Vitamin D and Body Mass Index on Disease Risk and Relapse Hazard in Multiple Sclerosis A Mendelian Randomization Study An Goris *Neurol Neuroimmunol Neuroinflamm* May 2022, 9(3):e1165
- Van der Knaap MS, Valk J (2005) Magnetic Resonance of Myelination and Myelin Disorders, eds Heilmann U, Mennecke-Buhler D (Springer, Berlin), pp 1–19.
- Veto S, Acs P, Dolowschiak T, Lendvai Z, Gallyas F, Komoly S, Berente Z. In vivo MRI follow-up of cuprizone-induced CNS changes. *Multiple Sclerosis* 2007; 13:S255-S255
- Walton C, King R, Rechtman L, et al., Rising prevalence of multiple sclerosis worldwide: Insights from the Atlas of MS, third edition. *Multiple Sclerosis Journal* 2020; 26(14):1816–1821.
- Wang H, Fu Y, Zickmund P, Shi R, Cheng JX. Coherent anti-stokes Raman scattering imaging of axonal myelin in live spinal tissues. *Biophys J* 2005; 89:581–591.
- Wansapura JP, Holland SK, Dunn RS, Ball WS, Jr. NMR Relaxation Times in the Human Brain at 3.0 Tesla. *J Magn Reson Imag* 1999; 9:531–538.
- Watanabe S, Suenaga K, Yamamoto A, Abe K, Kotoura N, Ishikura R, et al. Correlation of subthalamic nuclei T2 relaxation times with neuropsychological symptoms in patients with Parkinson's disease. *J Neurol Sci* 2012;315(1/2):96–9.
- Wei W, et al Predicting PET-derived myelin content from multisequence MRI for individual longitudinal analysis in multiple sclerosis, *NeuroImage*, 2020, 223:117308,
- Weijden van der CWJ, García DV, Borra RJH, Thurner P, Meilof JF, van Laar P-J, Dierck RAJO, Gutmann IW, de Vries EFJ. Myelin quantification with MRI: A systematic review of accuracy and reproducibility. *NeuroImage* 2021; 226: 117561
- Weinshenker BC. Epidemiology of multiple sclerosis. *Neurol Clin*. 1996; 142:1–308.
- Whittall KP, MacKay AL, Graeb DA, Nugent RA, Li DK, Paty DW. In vivo measurement of T2 distributions and water contents in normal human brain. *Magn Reson Med* 1997; 37:34–43.
- Wilhelm MJ, Ong HH, Wehrli SL, Li C, Tsai PH, Hackney DB, et al. Direct magnetic resonance detection of myelin and prospects for quantitative imaging of myelin density. *Proc Natl Acad Sci* 2012; 109(24):9605–10.
- Wu QZ, Yang Q, Cate HS et al. MRI identification of the rostral–caudal pattern of pathology within the corpus callosum in the cuprizone mouse model. *J Magn Reson Imag* 2008; 27(3):446–53.
- Wucherpfennig KW. Mechanisms for the induction of autoimmunity by infectious agents. *J Clin Invest* 2001; 108: 1097-1104.
- Zhang J, Hutton G, Zang Y. A comparison of the mechanisms of action of interferon beta and glatiramer acetate in the treatment of multiple sclerosis. *Clin.Ther.* 2002; 24: 1998-2021.
- Zhang JW, Markovicplese S, Lacet B, Raus J, Weiner HL, Hafler DA. Increased Frequency of Interleukin 2-Responsive T-Cells Specific for Myelin Basic-Protein and Proteolipid Protein in Peripheral-Blood and Cerebrospinal-Fluid of Patients with Multiple-Sclerosis. *J Exp Med* 1994; 179: 973-984.